

N°d'ordre :

PEOPLE'S DEMOCRATIC REPUBLIC OF ALGERIA
MINISTRY OF HIGHER EDUCATION AND SCIENTIFIC RESEARCH
UNIVERSITY OF SAIDA- Dr. TAHAR MOULAY



DOCTORAL THESIS

Specialty: Physics

Option: Physics of Materials

Entitled

First-principles calculations of structural, magnetic, electronic and mechanical properties of Heusler alloys

Elarabi Hiba

Defended on: 25 / 09 /2024

In front of the jury composed of:

<i>MESKINE Mohamed</i>	<i>PR</i>	<i>University of Saida Dr. Moulay Tahar</i>	<i>President</i>
<i>BOUDIA Keltouma</i>	<i>PR</i>	<i>University of Tissemsilet</i>	<i>Supervisor</i>
<i>KHELFAOUI Friha</i>	<i>MCA</i>	<i>University of Saida Dr. Moulay Tahar</i>	<i>Co-Supervisor</i>
<i>ZEMOULI Mostefa</i>	<i>PR</i>	<i>University of Saida Dr. Moulay Tahar</i>	<i>Examiner</i>
<i>SAHABI Toufik</i>	<i>MCA</i>	<i>University of Saida Dr. Moulay Tahar</i>	<i>Examiner</i>
<i>BOUAFIA Hamza</i>	<i>PR</i>	<i>University of Taret</i>	<i>Examiner</i>

Academic year 2023 – 2024

ACKNOWLEDGEMENTS

*I thank **ALLAH** the Almighty for giving me the courage, the will and the patience to accomplish this modest work,*

*First of all, I would like to express my warmest thanks to my dissertation supervisor, Pr. **Boudia Keltouma**, and my dissertation co-supervisor, Dr. **Kheffaoui Friha**. I would particularly like to thank them for giving me the benefit of their scientific skills, their human qualities and their constant availability.*

*I would like to express my thanks, respect and gratitude to Pr. **MESKINE Mohamed**, professor at the University of Dr. Moulay Tahar, Saida, for chairing the jury.*

*I would like to express my sincere thanks and deep respect to Pr. **ZEMOULI Mostafa**, lecturer at the University of Dr. Moulay Tahar, Saida, Dr. **SAHABI Toufik**, lecturer at the University of Dr. Moulay Tahar, Saida, and Pr. **BOUAFIA Hamza**, lecturer at the University of Tiaret, for agreeing to examine this work and doing me the honour of taking part in the jury.*

*I would like to express my sincere gratitude to Pr. **ElKeurti Mohammed** for providing me with the opportunity to conduct my doctoral research at Laboratory of physic-chemical studies. His guidance, support, and expertise have been invaluable throughout this journey. I would like to thank the entire Laboratory of physic-chemical studies team for their support and creating a conducive research environment.*

Finally, I would like to thank all those who contributed in any way to the completion of this work,

Elarabi Hiba

Dedication

I extend my sincere thanks and gratitude to God for His guidance and to my dear parents for their love and constant support, and To my brother and sisters.

Thank you to everyone who stood by my side and helped me, whether directly or indirectly.

I pray that God blesses all of you and that this success marks the beginning of a bright future filled with achievements.

Elarabi Hiba

تم استخدام طريقة الموجات المستوية المترابطة خطياً بكمون كامل (FP-LAPW) ، ضمن إطار نظرية الكثافة الوظيفية (DFT)، لدراسة الخصائص الهيكلية ، المرونية ، الإلكترونية ، والمغناطيسية لمركبات CrCoSi و MnCoSi والمشتقة منهما CrMnCo₂Si₂. أظهرت النتائج ، باستخدام تقريب التدرج المعمم (GGA) ، أن الطور الأخير من الترتيب من النوع الأول هو الأكثر استقراراً. ويظهر كل من CrCoSi و CrMnCo₂Si₂ مقاومة للتشوه ويمكن تصنيفها كمواد لينة، بينما يعتبر مركب MnCoSi هشاً. في الخصائص الإلكترونية تبين أن المركبات CrCoSi و MnCoSi و CrMnCo₂Si₂ تظهر سلوكاً معدنياً في الاتجاه المغزلي العلوي وسلوكاً شبيه موصل في الاتجاه السفلي، مع فجوات طاقة (فجوات طاقة نصف معدنية) تبلغ 0.851(0.020) eV، 0.852(0.021) eV، و 0.531(0.002) eV. يحتفظ المركب CrMnCo₂Si₂ النصف معدني بفجوة طاقة (فجوة نصف معدنية) تبلغ 0.38(0.106) eV. الكتل فولت مقارنة بـ GGA عند استخدام تقريب GGA + U، علاوة على ذلك، فإن إجمالي العزوم المغناطيسية المحسوبة هي أعداد صحيحة وتساوي 1 μ_B و 2 μ_B و 3 μ_B لـ CrCoSi و MnCoSi و CrMnCo₂Si₂، على التوالي. ومن المعروف أن عدم وجود الأنماط الرخوة (الترددات السالبة) في منحنى تشتت الفونون للمادة يدل على استقرارها الديناميكي. لذا تعتبر هذه السبائك مرشحة جيدة لتطبيقات السبينترونيك بسبب نصف معدنيته.

الكلمات المفتاحية: نصف المعدن، سبائك هوسلر، الاستقطاب الدوراني، FP-LAPW

Abstract

The full-potential linearized augmented plane waves (FP-LAPW) method, within the density functional theory (DFT), has been used to investigate the structural, elastic, electronic, and magnetic properties of CrCoSi, MnCoSi, and their CrMnCo₂Si₂ derivative DHH. The obtained results, utilizing the generalized gradient approximation (GGA), As a result, the latter phase of the type I arrangement is the most stable. This DDH as well as its CrCoSi parent HH are found to be resistant to deformation and can be classified as ductile materials whereas the MnCoSi compound is brittle. In the electronic properties, we found CrCoSi, MnCoSi, and CrMnCo₂Si₂ compounds exhibit a metallic behavior in the spin-up channel and a semiconducting behavior in the spin-down channel, with half-metallic gaps of 0.851(0.020) eV, 0.852(0.021) eV, and 0.531(0.002) eV, respectively. The half-metallicity of CrMnCo₂Si₂ DHH is kept with lower (bigger) band gap (half-metallic gap) of 0.38(0.106) eV than that of GGA, using GGA+U approximation. Moreover, their calculated total magnetic moments are integers and equal to 1 μ_B , 2 μ_B and 3 μ_B for CrCoSi, MnCoSi, and CrMnCo₂Si₂, respectively. And it is known that the absence of soft modes (imaginary modes; negative frequencies) in the phonon dispersion curve of a material implies its dynamical stability. Therefore, these alloys good candidates for spintronic applications due to their half-metallicity.

Key words: half-metal, heusler alloys, spin polarization, mechanical stability, FP-LAPW

Table of content

List of Figures.....	iv
List of tables.....	VII
General introduction.....	2
CHAPTER I: MAGNETISM AND SPINTRONICS	5
Introduction	6
I.2. Origin of magnetic moments	6
I.3. Different forms of magnetism	7
I.3.1. Diamagnetism	8
I.3.2. Paramagnetism	8
I.3.3. Ferromagnetism	8
I.3.4. Ferrimagnetism	9
I.3.5. Antiferromagnetism	9
I.4. Magnetic interactions	10
I.4.1. Direct exchange	10
I.4.2. Super-exchange	11
I.4.3. Exchange in 3d metals	13
I.4.4. Double exchange	13
I.4.5. Ruderman-Kittel-Kasuya-Yoshida (RKKY) indirect exchange:	14
I.5. Magnetic materials for spintronics	15
I.5.1. Giant magnetoresistance (GMR)	16
I.5.2. Tunnel magnetoresistance (TMR)	16
I.6. Spin polarization	17
I.7. Half-metallic materials	18
I.7.1. Definition of a half-metal	18
I.7.2. Examples of a half-metals	19
I.7.3. Clasification of half-metals	20
Reference.....	23
CHAPTER II: GENERALITIES OF HEUSLER ALLOYS	25
II.1. Introduction	26
II.2. Heusler alloys	27
II.2.1. Half Heusler	27
II.2.2. Full Heusler	28

II.2.3. Quaternary Heusler alloys	28
II.2.3. Double Half-Heusler alloys.....	29
II.3. Classification and crystal structure of Heusler alloys.....	30
II.3.1. Crystal structure of half-Heusler alloys	30
II.3.2. Crystal structure of full-Heusler alloys.....	31
II.4. Magnetism of Heusler alloys	31
II.5. Half-metallicity of Heusler alloys.....	32
II.5.1. Half-metallic ferromagnetism	33
II.5.2. Slater–Pauling rule.....	34
II.5.3. Relationship between disorder and spin polarization.....	35
II.6. Gap origin in half-Heusler alloys.....	35
II.7. Applications of the Heuslers:	37
Conclusion.....	38
Reference :	40
CHAPTER III: THEORY AND CALCULATION METHODS.....	43
III.1. Introduction	44
III.2. Schrödinger equation	44
III.3. Born-Oppenheimer approximation	46
III.4. Hartree- Fock approximation.....	46
a. Hartree approximation	46
b. Spin-orbit.....	47
III.5. Density functional theory (DFT)	48
III.5.1. Hohenberg-kohn theorems	49
III.5.2. Kohn-Sham method.....	51
III.5.3. Self-consistency in calculations.....	52
III.5.4. Exchange-correlation	53
III.6. Generalized-gradient approximations (GGA)	53
III.7. Local density (LDA) and generalized gradient (GGA) approximations with spin polarization	54
III.8. LDA and GGA approximations with Hubbard correction.....	54
III.9. Calculation method.....	55
III.9.1. Introduction	55
III.9.2. Augmented plane wave method (APW).....	56
III.9.3 Linearized augmented plane wave method (FP-LAPW)	58
III.9.3.1 Basic functions of the FP-LAPW.....	58

III.9.4 Roles of the linearization energies E_1	59
III.9.5 Construction of radial functions.....	59
III.9.5.1 Non-relativistic radial functions.....	60
III.9.6 Solving the Poisson equation.....	61
III.9.7 Improvement of the method (FP-LAPW).....	62
III.9.7.1 Multiple energy windows.....	62
III.9.7.2 Local orbital development.....	63
III.9.8 Treatment of spin-orbit effects.....	64
III.10. WIEN2k code	64
III.10.1 Initialisation	65
III.11. CASTEP code.....	67
References:.....	68
CHAPTER IV: RESULTS AND DISCUSSIONS	71
IV.1. Introduction.....	72
IV.2. Computational method.....	72
IV.3. Structural properties	73
IV-3.1 Crystalline structure of Heusler alloys and preferred sites	73
IV-3.2 Structural optimization and magnetic order	73
IV-3.2 Formation Energy (or enthalpy of formation).....	76
IV-4. Dynamical proprieties	77
IV.5. Mechanical properties	78
IV.6. Electronic and magnetic properties	81
IV-6.1. Electronic properties	81
IV-6.1.1. Electronic band structure	86
IV-6.1.2. Densities of states	90
IV-7. Magnetic properties.....	86
References	88
GENERAL CONCLUSION	90

List of Figures

Figure I.1: Magnetic field lines around a permanent magnet, materialized by iron filings..	06
Figure I.2: Types of magnetism.....	08
Figure I.3 : Bethe-Slater curve shows the relationship between the exchange integral and the ratio of the interatomic distance r_{ij} to the orbital radius « r_d ».....	11
Figure I.4: Magnetic order as a function of the type of orbital of neighbouring cations. The angle between two cations is fixed at 180°	12
Figure I.5: Double exchange: case of two ions Mn^{4+} and Mn^{3+} , separated by an oxygen ion.	13
Figure I.6: Schematic representation of the RKKY indirect exchange interaction. (+) and (-) represent the polarization of the conduction electrons as a function of the distance d from the magnetic ion located at site n_0 . \uparrow and \downarrow represent the orientation of the magnetic moments.....	14
Figure I.7: Spin-Dependent Transport Mechanism in Giant Magnetoresistance (GMR) structures	16
Figure I.8: Schematic representation of the densities of states and spin polarization of a non-ferromagnetic metal (A), a ferromagnetic material (B) and a half-metallic material (C)...	19
Figure I.9: Density of states of a type I or type II half-metal.	21
Figure I.10: Density of states for a class IIIA half-metal.	21
Figure I.11: Density of states of an IVA half-metal type.	22
Figure I.12: Two types of density of states of a VA-type half-metal. It concerns magnetic semiconductors, such as (GaMn)As.	22
Figure II.1: Periodic Table of Elements showing possible combinations of Heusler alloys.....	26
Figure II.2: Representative diagrams of the cubic meshes of a full Heusler alloy and a half Heusler alloy.....	28

Figure II.3: Crystal structure of quaternary-Heusler (Type I, Type II, Type III)29

Figure II.4: Regular and inverse structures for Mn₂-based Heusler alloys depending on the position of the Y element.....31

Figure II.5: (a) Half-Heusler alloys of the XYZ type, (b) X₂YZ Heusler alloys32

Figure II.6: Band structure for a (a) conventional ferromagnetic and (b) half-metallic material.....32

Figure II.7: Schematic illustration of the density of states of (a) a metal, (b) a metal (spin polarised), (c) a ferromagnet, (d) a half-metallic ferromagnet, and (e) a half-metallic ferrimagnetic half-metallic.....33

Figure II.8: Slater-Pauling curve for 3d alloys as a function of the number of valence electrons.....35

Figure II.9: Illustration of the origin of the gap and the hybridization of d states in Co₂YZ materials.....36

Figure II.10: Illustration of the degeneration of d orbitals into two levels eg(dx²-y²,dz²)and t_{2g}(dxy, dyz, dzx).....37

Figure II.11: Working principle of giant magnetoresistance (GMR).....38

Figure III.1: Solution of the Kohn and Sham equations: Self-consistent cycle52

Figure III.2: Diagram of the distribution of the elementary mesh into atomic spheres and interstitial region.....57

Figure III.3: Multiple energy windows.....63

Figure III.4: Program Flowchart in WIEN2k Software66

Figure IV.1. Total energy per formula unit of ferromagnetic (FM), non-magnetic (NM) and antiferromagnetic (AFM) phases as functions of the volume for CrCoSi and MnCoSi HH alloys.....75

Figure IV.2. Total energy per formula unit as functions of the volume for the ferromagnetic (FM), non-magnetic (NM), and antiferromagnetic (AFM) phases of CrMnCo₂Si₂ DHH alloy.....75

Figure IV.3. Phonon dispersion diagram along lines of high symmetry in the Brillouin zone for the $\text{CrMnCo}_2\text{Si}_2$ compound.....78

Figure IV.4: Valence bands, conduction bands, band gap and the Fermi level.....82

Figure IV.5: Spin-polarized band structures for CrCoSi , MnCoSi , and $\text{CrMnCo}_2\text{Si}_2$ Heusler alloys.....83

Figure IV.6: Spin-polarized density of states (DOS) for CrCoSi , MnCoSi , and $\text{CrMnCo}_2\text{Si}_2$ Heusler alloys.....85

List of tables

Table I.1: Some examples of half-metals.....	19
Table II.1: Atomic Sites of Inequivalent Combinations in Quaternary Heusler Alloys	29
Table II. 2: Different possibilities for occupying non-equivalent sites in the C1b half- Heusler structure.....	30
Table III.1: Atomic units.....	45
Table IV.1: The different possibilities for occupying non-equivalent sites in the Hlef- Heusler C1b structure, for the compounds studied CrCoSi , MnCoSi.....	73
Table IV.2 Calculated lattice parameters (in Å) for the structural ground state of the CrCoSi, MnCoSi HH alloys and parent structure of CrMnCo ₂ Si ₂ DHH, bulk moduli (in GPa), their derivative pressures, and magnetic ground phase (FM) for CrCoSi, MnCoSi and CrMnCo ₂ Si ₂ compounds.....	76
Table IV.3. Calculated formation (E_{form}) energies (in eV/Atom) of the structural and magnetic ground phase (FM) for CrCoSi, MnCoSi and CrMnCo ₂ Si ₂ compounds.....	77
Table IV.4 Elastic constants C_{11} , C_{12} , C_{13} , C_{33} , C_{44} , C_{66} (in GPa), bulk B, Young E(GPa), Shear G moduli (in GPa), B/G, Anisotropic parameter A, and Poisson's coefficients ν of CrCoSi, MnCoSi and CrMnCo ₂ Si ₂ Heusler alloys.....	80
Table IV.5: Gap, and Half-metallic gap (in eV) of CrCoSi, MnCoSi, and CrMnCo ₂ Si ₂ Heusler alloys.....	84
Table IV.6: Atomic (M_{Cr} , M_{Co} , M_{Mn} , M_{Si}), interstitial ($M_{Intersti}$) and total magnetic (M_{tot}) moments (in μ_B) for CrCoSi, MnCoSi, and CrMnCo ₂ Si ₂ Heusler alloys.....	87

*General
Introduction*

General introduction

Electronic and magnetic devices are at the forefront of rapidly evolving technologies, driven by advances in the understanding of material physics. The physical properties of solids are intricately linked to the behaviour of their constituent electrons, making them the subject of ongoing scientific investigation. In addition to structural properties, important considerations include mechanical aspects such as elasticity and physical metallurgy, as well as electrical properties like dielectric behaviour, semiconductor performance, and conductivity. Magnetic and thermodynamic properties also play critical roles. Technological progress demands continuous improvements in material applications, and before industrial implementation, rigorous assessments of structural integrity, electrical conductivity, and other key attributes are essential.

Magnetic phenomena have been studied for nearly 2,500 years, starting with the early use of magnetite and iron's attractive properties. By the 11th and 12th centuries, magnets were being applied practically in compasses for navigation. The 17th century saw the first detailed treatises on magnetism and its uses. In the late 18th century, figures like Coulomb and Poisson laid the foundation for magnetic theory. The 19th century brought significant advances, including Maxwell's electromagnetic theory and Curie's work, which revealed key phenomena such as paramagnetism, diamagnetism, and ferromagnetism.

Despite major advancements in electronics in recent decades, magnetic materials have received comparatively little attention in integrated electronic systems. However, the rise of spintronics has sparked renewed interest. This emerging field takes advantage of electrons' intrinsic spin property in addition to their charge. In spintronics, information transfer within circuits is controlled by electron spins rather than by electrical charges. Historically, magnetic materials and semiconductors developed separately, with magnetic materials mainly used for data storage.

Heusler alloys are highly versatile materials with widespread applications in magnetic tunnel junctions, magnetoresistance, and giant magnetoresistance technologies. Named after Friedrich Heusler, who in 1903 discovered the ferromagnetic properties of Cu_2MnAl despite its constituent elements being non-magnetic[1], these compounds, along with their variants exceeding 1,000, are now referred to as Heusler compounds. They consist of ternary semiconducting or metallic compounds, with two primary stoichiometries: 1:1:1,

known as "Half-Heusler," and 2:1:1, referred to as "Full Heusler." A major breakthrough in the study of Heusler alloys came in 1983, when de Groot and colleagues [2] predicted half-metallicity in the NiMnSb alloy. This sparked renewed interest and led to extensive theoretical and experimental research into these materials. In addition to NiMnSb, many other Heusler alloys, including Co-based variants, have been predicted through ab initio calculations to exhibit half-metallic behavior, characterized by 100% spin polarization. With high Curie temperatures, these materials show significant promise for commercial spintronics applications.

In half-metallic materials, the two spin bands behave distinctly: the majority spin band demonstrates typical metallic properties, while the minority spin band behaves as a semiconductor, featuring a band gap at the Fermi level. This gap results in 100% spin polarization at the Fermi level, making fully polarized spins achievable in these compounds. Such properties enhance the efficiency of magnetoelectric devices, offering great potential for spintronic technologies [3, 4].

Recently, Double Half-Heusler materials have gained significant attention from researchers and scientists worldwide due to their promising applications in various fields. These compounds are categorized into three distinct groups based on substitution sites in the XYZ phase: $X'X''Y_2Z_2$, $X_2Y'Y''Z_2$, and $X_2Y_2Z'Z''$. This classification has spurred considerable interest, as each variant offers unique properties. However, heat transfer in Double Half-Heuslers presents challenges, particularly due to disordered scattering influenced by low-frequency phonon modes with low group velocities.

Advances in ab initio methods now allow for highly accurate calculations of numerous material properties, including elasticity, optical spectra, and lattice vibration frequencies, even in complex systems. Among these techniques, the linearized augmented plane wave (FP-LAPW) method[5] stands out as one of the most precise tools for determining the electronic structure of solids within the density functional theory (DFT) framework. DFT, developed by Hohenberg, Kohn, and Sham in the 1960s and 1970s, is a powerful approach for describing a system's ground state, enabling its numerical implementation with high accuracy.

The aim of this study is to provide a theoretical investigation into the half-metallicity of CrCoSi and MnCoSi half-Heusler alloys, as well as their derivative double half-Heusler compound CrMnCo₂Si₂. The research is structured into four chapters as follows:

1. **Chapter 1** offers a review of fundamental concepts in magnetism, including the different types of magnetic behavior. It also examines the technological applications of ferromagnetic compounds, such as Giant Magnetoresistance (GMR) and Tunnel Magnetoresistance (TMR).
2. **Chapter 2** provides an in-depth exploration of Heusler alloys and Double Half-Heusler compounds, along with their key properties.
3. **Chapter 3** focuses on Density Functional Theory (DFT), which serves as the foundation for the ab initio calculations in this study. It includes a discussion of the FP-LAPW method and explains the various approximations applied in the research. Additionally, it details the functionalities of the programs used in the Wien2K code that were implemented in this investigation.
4. **Chapter 4** presents the results of the study, focusing on the CrCoSi and MnCoSi parent half-Heusler alloys and their derivative CrMnCo₂Si₂ double half-Heusler compound. This chapter covers structural, electronic, elastic, and magnetic properties, with particular emphasis on the results obtained using the Generalized Gradient Approximation (GGA) method for exchange-correlation interactions.

References

- [1] F. Heusler, W. Starck, E. Haupt, Magnetisch-chemische studien, Verh. Dtsch. Phys. Ges 5 (1903) 219-232.
- [2] R.A. De Groot, F.M. Mueller, P.v. van Engen, K. Buschow, New class of materials: half-metallic ferromagnets, Physical review letters 50 (1983) 2024.
- [3] J. De Boeck, W. Van Roy, J. Das, V. Motsnyi, Z. Liu, L. Lagae, H. Boeve, K. Dessen, G. Borghs, Technology and materials issues in semiconductor-based magnetoelectronics, Semiconductor science and technology 17 (2002) 342.
- [4] J. De Boeck, W. Van Roy, V. Motsnyi, Z. Liu, K. Dessen, G. Borghs, Hybrid epitaxial structures for spintronics, Thin Solid Films 412 (2002) 3-13.
- [5] P. Blaha, K. Schwarz, P. Sorantin, S. Trickey, Full-potential, linearized augmented plane wave programs for crystalline systems, Computer physics communications 59 (1990) 399-415.

CHAPTER I

MAGNETISM AND SPINTRONICS

I.1. Introduction

The concept of "magnetism" refers to the wide range of phenomena that occur in and around materials that are either naturally magnetized, or influenced by an external magnetic or electric field. Magnetism plays a crucial role in various fields, including information technology, healthcare, and particle physics, with applications ranging from data storage and medical imaging to particle accelerators and magnetic confinement in fusion research.[1].

Since solids are composed of atoms, it is essential to recognize that the fundamental properties of a material are determined by the interactions between the atoms within the crystal lattice. Electron interactions are responsible for shaping the energy band structure, while interactions between ions govern the vibrational properties of the lattice. These interactions collectively define the material's electronic, optical, and thermal characteristics.

In practical terms, materials referred to as "magnets" are generally classified into two main types: "hard" magnets and "soft" magnets. Hard magnets retain their magnetism permanently and can magnetize or attract soft magnets, which, in contrast, lose their magnetism quickly. Soft magnets are easily magnetized and demagnetized, making them suitable for applications where temporary magnetism is required. Hard magnets, on the other hand, produce a stable magnetic field, which can be visualized using iron filings (see Figure I.1).

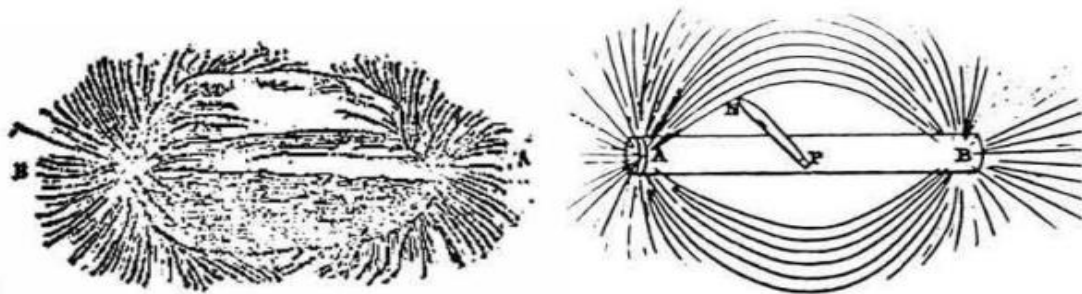


Figure I.1: Magnetic field lines around a permanent magnet, materialized by iron filings.

I.2. Origin of magnetic moments

In general, electrons within an atom arrange themselves according to Pauli's exclusion principle and Hund's rules. These rules dictate that electrons in the same quantum state form

pairs and can occupy sub-levels within the same energy level. The principle of achieving the lowest energy state prevails, favouring configurations with the greatest number of occupied quantum cells and the highest number of parallel spins (unpaired electrons).

Partially filled d or f orbitals, as seen in transition metals and rare earth elements, contain unpaired electrons, which give rise to magnetism. The atomic magnetic moment is composed of two main components:

- **The orbital magnetic moment (μ_L)**, which arises from the rotational motion of electrons around the nucleus.
- **The spin magnetic moment (μ_S)**, which is due to the intrinsic spin of the electrons.

Magnetization, denoted as (\vec{M}), is the macroscopic measure of a material's magnetic behaviour, representing the total magnetic moment per unit volume.

A key characteristic of magnetic materials is their response to an applied magnetic field, \vec{H} . This response is captured by the magnetic susceptibility, χ , which quantifies the material's reaction to the external field. Mathematically, magnetic susceptibility χ is defined as:

$$\chi = \lim_{H \rightarrow 0} \frac{\delta \vec{M}}{\delta \vec{H}} \quad \text{I.1}$$

In general, χ is a tensor, but for isotropic materials, susceptibility becomes a scalar quantity, denoted simply as χ .

I.3. Different forms of magnetism

Various forms of magnetism arise from the statistical behaviors of individual atomic systems, influenced by factors such as the presence of magnetic moments and the occupation of atomic sublayers. Below is a brief overview of the primary types of magnetic behavior, We will now provide a brief overview of the primary types of magnetic behavior: diamagnetism, paramagnetism, antiferromagnetism, ferromagnetism, and ferrimagnetism.

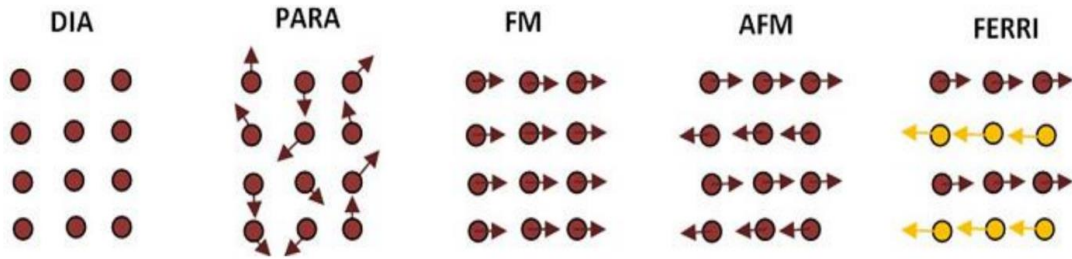


Figure I-2: Types of magnetism

I.3.1. Diamagnetism

Diamagnetic metals exhibit exceptionally low and negative magnetic susceptibility. When subjected to a magnetic field, diamagnetic materials experience a repulsive force, and they lose all magnetic properties once the external magnetic field is withdrawn. Unlike magnetic materials, diamagnetic ones lack a permanent magnetic moment per atom due to the complete pairing of their electrons. The manifestation of their magnetic characteristics results from the rearrangement of electron orbitals influenced by an external magnetic field. Notably, the majority of elements in the periodic table fall under the category of diamagnetic materials, including copper, silver, and gold.

I.3.2. Paramagnetism

Paramagnetism emerges in materials with atoms that have inherent magnetic moments due to unpaired electron spins and orbital magnetic moments. This property is characterized by a modest positive susceptibility. Thermal agitation counteracts the tendency of magnetic moments to align with the magnetic field, making paramagnetism often temperature-dependent. Notably, susceptibility inversely responds to temperature.

In substances with permanent magnetic moments, paramagnetism prevails over diamagnetism. When the temperature surpasses the Curie point, most gases, certain metals (such as aluminum, manganese, and tungsten), and ferromagnetic and ferrimagnetic materials transition into a paramagnetic state.

I.3.3. Ferromagnetism

Ferromagnetic materials exhibit notably high and positive susceptibility when subjected to external magnetic fields. They have a strong affinity for magnetic fields and can retain their magnetization even after the external magnetic field is removed. Due to the

presence of unpaired electrons within their atomic structure, ferromagnetic materials possess a net magnetic moment.

The strength of their magnetic properties is rooted in the existence of magnetic domains. These domains consist of large groups of atomic moments aligned in parallel, creating a strong magnetic force within the domains. In the absence of an external magnetic field, these domains are typically oriented randomly, resulting in an overall net magnetic field close to zero. When a magnetizing force is applied, the domains align, producing a strong magnetic field within the material. Metals such as iron, nickel, and cobalt are examples of ferromagnetic materials. Components made from these materials are commonly inspected using methods like magnetic particle inspection.

I.3.4. Ferrimagnetism

These different forms of magnetism play crucial roles in various technological applications and are fundamental to understanding the behavior of magnetic materials. Ferrimagnetism characterizes a specific category of oxides known as ferrites. Within their structure, two distinct crystalline lattices, denoted as A and B, are identifiable. These lattices feature antiparallel and typically dissimilar magnetic moments, namely m_A and m_B . This arrangement gives rise to spontaneous magnetization that diminishes as temperature increases. Beyond the Curie temperature, these materials transition into a paramagnetic state and exhibit notably low conductivity, which is particularly important at higher frequencies. However, ferrites have reduced permeability, increased coercive field, and decreased saturation field. Ferrites can be classified as either soft or hard. Mechanically, they are characterized as hard and brittle.

I.3.5. Antiferromagnetism

In antiferromagnetic materials, the exchange interaction prompts them to segregate into two ferromagnetic sub-lattices that exhibit opposing movement directions. While these materials possess a positive magnetic susceptibility, it generally tends to be lower than that observed in ferromagnetic materials. When temperatures surpass a pivotal point called the Néel temperature, these materials exhibit behavior similar to ferromagnetic substances.

I.4. Magnetic interactions

We have shown that even in the absence of an external magnetic field, a ferromagnetic material maintains a non-zero magnetic moment and exhibits spontaneous magnetization. In contrast, an antiferromagnetic material, despite having an overall zero net moment, has a well-defined arrangement of magnetic moments. In a solid, the alignment of these moments results from their mutual interactions. These interactions determine whether spins align in parallel (as in ferromagnetic materials) or in an antiparallel manner (as in antiferromagnetic materials). This phenomenon, known as the exchange interaction, is a purely quantum mechanical effect discovered by Heisenberg.

The next section will explore the primary methods used to characterize magnetic exchange interactions.

I.4.1. Direct exchange

Pauli's principle and short-range Coulombic interactions among individual magnetic moments constitute the fundamental underpinnings of the direct exchange interaction. In accordance with Pauli's principle, the nature of the direct exchange interaction is rooted in the antisymmetry of electron wave functions.

In a two-spin system, the exchange energy is established by the disparity in energy levels between parallel and antiparallel spin orientations. For systems encompassing multiple electrons, this energy is quantified by the Heisenberg Hamiltonian:

$$H_{\text{éch}} = -2 \sum J_{ij} S_i S_j \quad \text{I.2}$$

Where J_{ij} is called the exchange integral related to the overlap of orbitals and describes the coupling between the two spins represented by the \vec{S}_i and \vec{S}_j operators. It depends significantly on the interatomic distance between the atoms. If J_{ij} is positive, the energy term will be minimal when all the magnetic spin moments align parallel (ferromagnetic materials). If J_{ij} is negative, the spin moments align antiparallel (antiferromagnetic materials). The evolution of J_{ij} can be seen on the Bethe-Slater curve.

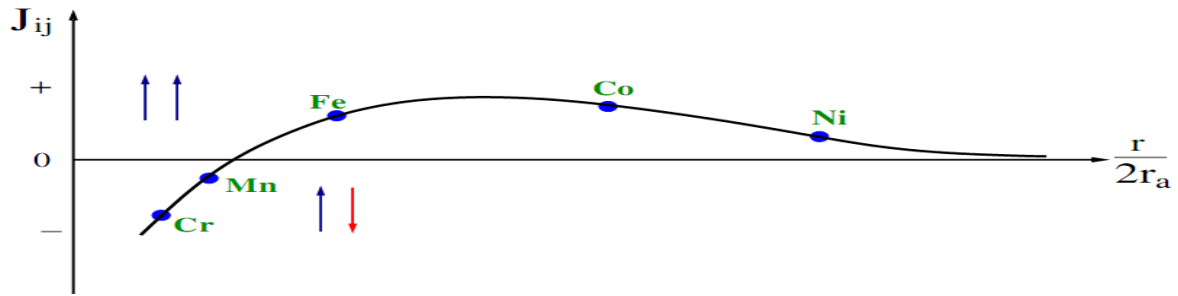


Figure I.3 : Bethe-Slater curve shows the relationship between the exchange integral and the ratio of the interatomic distance r_{ij} to the orbital radius r_a [2].

I.4.2. Super-exchange

Antiferromagnetism observed in LaMnO_3 crystals has been elucidated through the framework of the super-exchange interaction [3, 4]. This mechanism involves an indirect process where two magnetic cations interact via an oxygen anion. The magnetic moments of the ions are correlated through an exchange interaction that connects their valence band p orbitals. Notably, there is no orbital overlap between the nearest neighbors of the magnetic ions in this scenario. Importantly, the presence of delocalized charge carriers is not a prerequisite for superexchange.

Goodenough et al [4] formalized the concept of super-exchange interaction in insulating materials based on the d -orbital configuration of magnetic ions and the bond angle (magnetic ion-oxygen-magnetic ion). This conceptualization led to the development of the Goodenough-Kanamori rules. Figure I.4 illustrates various cation-anion-cation combinations at an angle of 180° . In cases where both cations possess half-filled e_g orbitals oriented towards the anion, direct coupling according to Hund's principles occurs, yielding robust antiferromagnetism (case 1). Modest antiferromagnetism is also apparent in case 2, where both e_g orbitals remain vacant. In this instance, electrons from the cation have a non-zero probability of being in the unoccupied e_g orbital. However, this scenario is transient, explaining the weak interaction. Conversely, in case 3, one cation has a half-filled e_g orbital while the other remains empty. Here, a virtual transition of the electron from one cation to another is viable, provided the spins of the two cations are aligned in parallel. This virtual transition results in a weak ferromagnetic interaction.

The crystal field in these three situations exhibits octahedral symmetry. However, cobalt ions, which replace zinc ions in co-doped ZnO , introduce tetrahedral symmetry.

Despite this difference, the reversed energy position of the e_g and t_{2g} orbitals in the latter situation does not alter the logic concerning magnetic order. The nature of coupling is contingent upon the angle between magnetic cations and their concentrations. Consequently, it's plausible that both the concentration of Co ions and the associated angle between them can lead to a ferromagnetic interaction.

Case	orbital configuration	super-exchange coupling
1		strong antiferromagnetic coupling
2		weak antiferromagnetic coupling
3		weak antiferromagnetic coupling

Cation	Description
	Filled orbitals t_{2g} and one half-filled orbital e_g pointing in the direction of the anion
	Filled orbitals t_{2g} and one empty filled orbital e_g pointing in the direction of the anion
	Orbitale $p\sigma$

Figure I.4: Magnetic order as a function of the type of orbital of neighboring cations. The angle between two cations is fixed at 180° [4].

I.4.3. Exchange in 3d metals

The magnetic moments observed in transition metals like Co, Fe, and Ni arise from the disparity in occupancy between the majority spin and minority spin bands. The interplay between these magnetic moments occurs when the 3d wave functions of adjacent sites overlap.

I.4.4. Double exchange

In 1951, Zener[5, 6] introduced the double exchange model to explain ferromagnetism in manganites, particularly perovskites with the general formula $A_{1-x}B_xMnO_{3-\alpha}$, like $La_{0.7}Sr_{0.3}MnO_{3-\alpha}$ [3]. This model utilizes oxygen ions as intermediaries to enable electron transfer between manganese cations with different charge states (III and IV), which are too far apart for direct cation-cation exchange.

Zener's proposition establishes that the fundamental state is characterized by the parallel alignment of spins of localized electrons in accordance with Hund's laws. Within this context of parallel localized spins, electrons are poised to migrate, giving rise to both ferromagnetic interactions and concurrent electron delocalization. Notably, the presence of available free-charge carriers distinguishes this interaction from superexchange mechanisms. Consequently, the material must exhibit metallic behavior to facilitate the transport of electrons between Mn ions. configuration, both prior to and subsequent to electron transfer, can be comprehensively described using degenerate wave functions:

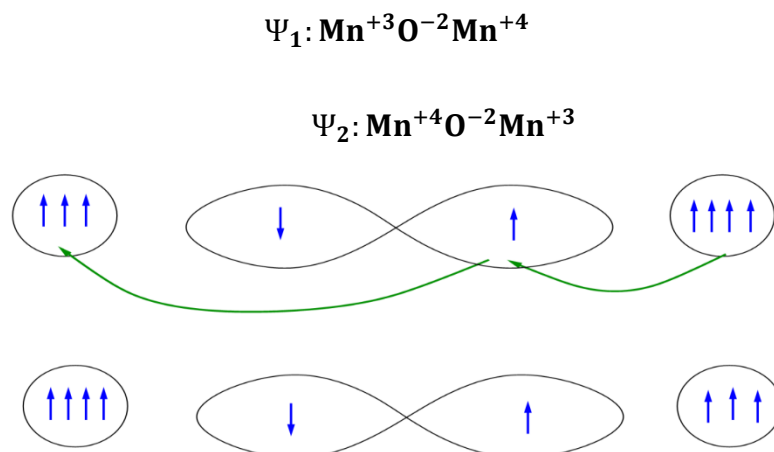


Figure I.5: Double exchange: case of two ions Mn^{4+} and Mn^{3+} separated by an oxygen ion.

The system's At the same time as an electron from the Mn^{4+} ion jumps towards the oxygen, the latter gives up an electron to the other Mn ion. This is only possible if the two Mn ions have their spins parallel.

I.4.5. Ruderman-Kittel-Kasuya-Yoshida (RKKY) indirect exchange:

The RKKY (Ruderman-Kittel-Kasuya-Yosida) interaction, facilitated by electrons in the conduction band, constitutes a potent indirect exchange mechanism between the localized moments associated with the inner layer's d orbitals. In this mechanism, a d-electron spin interacts with a conduction electron, which subsequently interacts with another d-electron spin. This interplay generates an energy correlation connecting the two spins. The orientation of the conduction electron's spin is influenced by the magnetic ion's surroundings, and its polarization fluctuates in an oscillatory pattern as the distance from the magnetic ion varies. The nature of the J coupling, whether ferromagnetic or antiferromagnetic, alternates based on the electron density within the free electron gas and the distance between the two magnetic ions. It's important to note that this interaction requires the presence of free charge carriers, often referred to as itinerant electrons or holes.

Moreover, this concept has been utilized to elucidate the ferromagnetic or antiferromagnetic coupling between two thin layers of a ferromagnetic metal separated by a thin layer of a non-magnetic metal. The nature of the connection between the two layers, whether ferromagnetic or antiferromagnetic, depends on the thickness of the nonmagnetic layer [7].

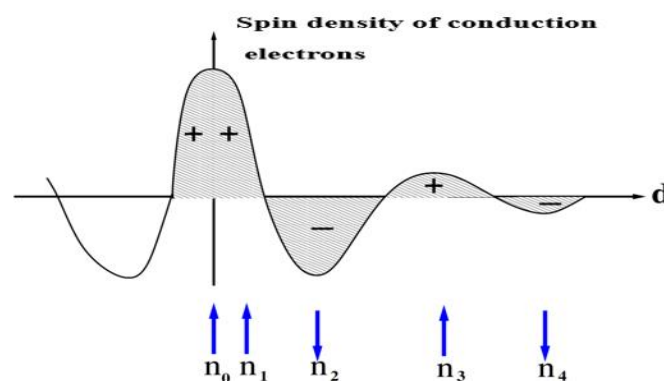


Figure I.6: Schematic representation of the RKKY indirect exchange interaction. (+) and (-) represent the polarization of the conduction electrons as a function of the distance d from the magnetic ion located at site n_0 . ↑ and ↓ represent the orientation of the magnetic moments [8].

I.5. Magnetic materials for spintronics

Spintronics, also known as spin electronics, has emerged as a pivotal technology within the realm of information storage in recent years. Despite the primary focus of this thesis on magnetic materials for microwave applications, we have chosen to include this segment due to the profound relevance of spintronics in shaping innovative magnetic materials.

At its core, spintronics is a cutting-edge technology harnessing electron spin, particularly the phenomenon of spin-polarized current. Foundational works in the realm of spintronics include the discovery of Tunneling Magnetoresistance (TMR) by Jullière in 1975, the observation of spin-polarized current injection from a ferromagnetic material to a non-magnetic metal by Johnson and Silsbee in 1985[9], and the breakthrough discovery of Giant Magnetoresistance (GMR) by Fert et al. in 1988 [10] and Grünberg et al. in 1989[11].

Ferromagnetic materials like Fe or Co exhibit asymmetry in their d-bands for up and down electrons, leading to differing densities of electronic states between the two spin states, often referred to as majority and minority spins. Consequently, when an electron traverses a ferromagnetic material, its probability of diffusion varies based on its spin state. This difference in diffusion probabilities results in distinct electrical resistivity for spin up and spin down states. Consequently, an electric current flowing through a ferromagnetic material experiences a change in the number of electrons with spin up and spin down states, a phenomenon termed spin-polarization. This underlying effect forms the basis for phenomena such as Giant Magnetoresistance (GMR) and Tunnel Magnetoresistance (TMR).

In essence, spintronics is an innovative avenue that capitalizes on spin-related phenomena to revolutionize information technologies and, by extension, drive the advancement of novel magnetic materials.

I.5.1. Giant magnetoresistance (GMR)

William Thomson developed magnetoresistance in 1857, which refers to the alteration in electrical resistance due to the presence of a magnetic field. After 130 years of theoretical exploration and applications of magnetoresistance, the development of measurement devices, detectors, and sensors occurred toward the close of the 1980s.

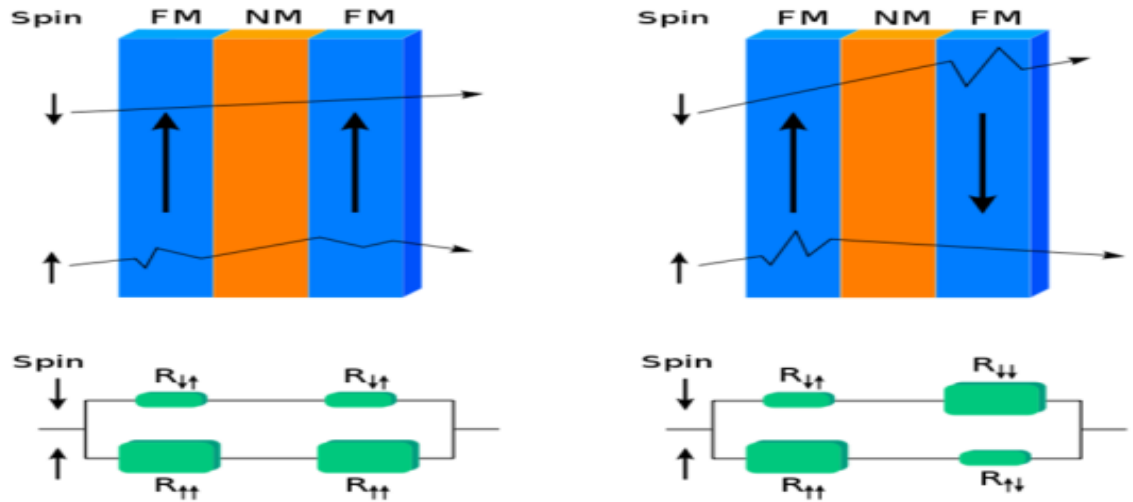


Figure I.7: Spin-Dependent Transport Mechanism in Giant Magnetoresistance (GMR) Structures.

The Giant Magnetoresistance (GMR) effect is a quantum phenomenon that manifests in a structure known as a Ferro/Metal/Ferro stack[12]. These devices comprise two thin ferromagnetic layers separated by a non-magnetic conducting layer. Ferromagnetic electrodes are commonly crafted from materials like iron, cobalt, and their alloys, while the non-magnetic layer employs materials such as copper and chromium. The GMR effect, which leads to significant changes in electrical resistance, revolutionized the landscape of magnetoresistance and paved the way for numerous applications.

I.5.2. Tunnel Magnetoresistance (TMR)

The Tunnel Magnetoresistance (TMR) phenomenon is discernible in Ferro/Insulator/Ferro systems. It manifests as fluctuations in electrical resistance that arise as an electric current tunnels through an insulator, contingent on the arrangement of ferromagnetic materials. Given that the conduction in both ferromagnetic materials is solely quantum in nature, the TMR is contingent on the variance in states accessible through the barrier.

The Magnetic Tunnel Junction (MTJ) stands as the predominant device harnessed in contemporary technologies (e.g., MRAM memory) to exploit the TMR effect. In this structure, two ferromagnetic electrodes are demarcated by a dielectric barrier, commonly composed of materials like MgO or Al₂O₃. While Jullière[12] made the initial observations

of this phenomenon in 1975, it wasn't until 1995 that TMR garnered renewed attention, bolstered by the work of Moodera et al. on Co/Al₂O₃/CoFe stacks [13].

Recent advancements have illuminated that employing Heusler materials as electrodes in Magnetic Tunnel Junctions (MTJs)[14, 15] can yield substantial TMR values, signifying a promising avenue for enhancing the efficiency of these devices.

I.6. Spin polarization

In the realm of spintronics, a key parameter for characterizing the properties of a magnetic layer is spin polarization. This property quantifies the degree of asymmetry in densities of states at the Fermi level (E_F) between spin up and spin down states. The following expression serves as a definition for this intrinsic material characteristic that quantifies spin asymmetry.

$$P = \frac{N\uparrow(E_F) - N\downarrow(E_F)}{N\uparrow(E_F) + N\downarrow(E_F)} \quad \text{I.2}$$

Here, $N\uparrow(E_F)$ and $N\downarrow(E_F)$ denote the values of the densities of states for majority and minority spins, respectively, at the Fermi level (E_F). It's important to note that spin polarization phenomena are highly intricate, and there is currently no single model that can comprehensively unify all the observed outcomes.

Indeed, research has revealed that the spin polarization of an electrode is influenced by the ferromagnetic/insulator interface[16]. Depending on the specific type of barrier employed, the sign or magnitude of spin polarization from the same electrode can undergo changes. For example, the alumina barrier favors s states, resulting in a positive spin polarization value when measuring cobalt through a tunnel junction[17]. On the contrary, a strontium titanate (SrTiO₃) barrier yields negative polarization, favoring d states[17]. Moreover, spin polarization measurements acquired via field emission techniques can exhibit varying signs contingent upon the crystallographic direction.

The experimental determination of a material's spin polarization is challenging due to the variability in measurement outcomes. To accurately discuss the spin polarization of a material, the nature of the barrier, identical to the second electrode, must be specified. Additionally, the value of spin polarization is influenced by temperature, further complicating the picture. Therefore, to compare spin polarization levels across different

materials, it's crucial to employ the same measurement method and equipment, including consistent barrier and top electrode choices.

I.7. Half-metallic materials

I.7.1. Definition of a half-metal

The term "half-metal" originates from the fusion of a metal with a semiconductor or insulator. In the early 1980s, Groot and van Niemen coined the term "half-metal" to describe the band structure of Heusler alloys [18]. According to de Groot's definition, A half-metal is a material in which conduction electrons are exclusively allowed to possess one spin direction, while a gap at the Fermi level exists for the other spin direction. Essentially, only either spin-up or spin-down electrons contribute to conduction (see Figure I.8), leading to 100% spin polarization within half-metal materials.

Typically, half-metals are found in conducting oxides like Fe_3O_4 [19], $\text{La}_{0.7}\text{Sr}_{0.3}\text{MnO}_3$ [20], or in lacunar alloys, specifically half-Heusler alloys like NiMnSb [21].

These materials exclusively present a d-band at the Fermi level. However, it's important to note that this definition and the depiction in the C diagram (Figure I.8) are limited, as they correspond to a specific subset of half-metals.

Contrary to popular notion, robust ferromagnets such as Co or Ni do not equate to half-metals. In reality, the 4s bands at the Fermi level in these materials are non-polarized, while the 3d bands of Co or Ni are highly polarized with 100% spin. Thus, the Fermi level contains either up or down electrons. To achieve a half-metallic state, the 3d and 4s bands need to hybridize in a manner that shifts the Fermi level away from the 4s band. This implies that no single-atom substance can exhibit half-metallicity. Additionally, it's crucial to differentiate between half-metals and half-metals like bismuth. The latter contain an equal number of holes and electrons due to minimal overlap between the valence and conduction bands, unlike the distinct polarization seen in true half-metals.

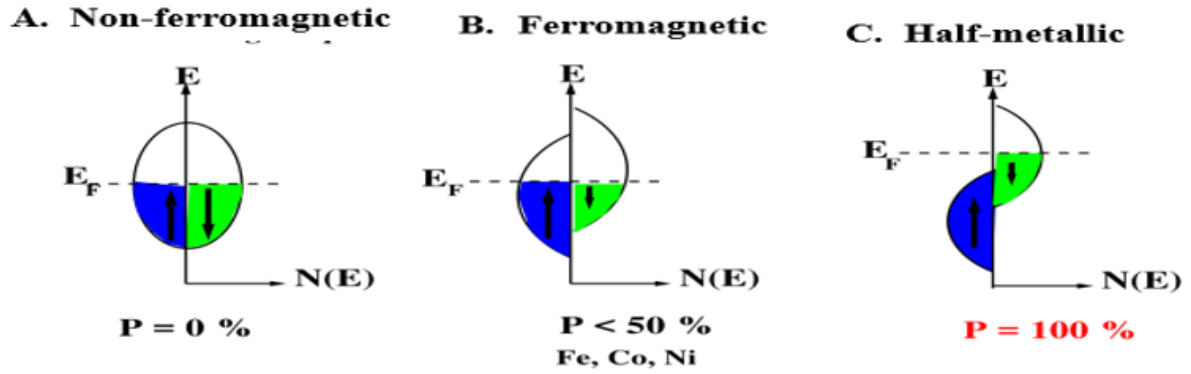


Figure I.8: Schematic representation of the densities of states and spin polarization of a non-ferromagnetic metal (A), a ferromagnetic material (B) and a half-metallic material (C).

I.7.2. Examples of half-metals

First of all, the materials in **Table I.1** don't seem to have much in common in terms of crystallographic structure. have much in common in terms of crystallographic structure, even though they are all are all half-metallic.

Table I.1: Examples of half-metals.

Structure	Material	P à 5K	M_s ($\mu_B/u.f$)	T _c (K)	References
Rutile AO ₂	CrO ₂	96%	2	390	[22]
Spinel AB ₂ O ₄	Fe ₃ O ₄	/	4	840	[19]
Heuslers A ₂ MnB	Co ₂ MnSi	89%	5	985	[23]
Half Heuslers AMnB	NiMnSb	/	4	730	[20]
Manganites ABMnO ₃	La _{1-x} Sr _x MnO ₃	95%	/	340	[24]
Dilute magnetic SCs	(Ga,Mn)As	85%	/	110	[25]
Double perovskite	Sr ₂ FeMoO ₆	85%	4	415	[26]

Furthermore, only a limited subset of half-metals have achieved near 100% spin polarization, primarily due to the inherent challenges in polarization detection and material synthesis. Among the difficulties, it's noteworthy that many half-metals (referred to as types I and II, as elaborated in the subsequent section) exhibit magnetism equivalent to an integer number of Bohr magnetons a concept elucidated by the visual representation at the top.

Specifically, the relation $n = n + n$ results in an integer due to complete state occupation, as illustrated in Figure I-8. Consequently, the magnetization equates to an integer value of Bohr magnetons, as expressed by the formula $M_s = (n + n) \mu_B$.

Lastly, it's worth highlighting that diverse half-metals possess distinct Curie temperatures. In terms of practical applications, half-metals with Curie temperatures surpassing room temperature hold greater allure. This preference arises from the fact that a reduction in polarization corresponds with the loss of ferromagnetic order[27]. While certain half-metals like magnetite exhibit notably high Curie temperatures, challenges in manufacturing thin films, possibly due to parasitic phases, can complicate their practical implementation.

I.7.3. Classification of half-metals

Coey and Venkatesan's classification[28] of half-metals is outlined below, differentiating between five distinct types of half-metals. They establish an **A** family for conduction through "up" electrons and a **B** family for conduction through "down" electrons within each type.

Type-I Half-Metals: This category involves instances where either the hybridization of the 4s energy levels with the 2p oxygen states lifts the 4s levels above the Fermi level, or p-d hybridization shifts the Fermi level downwards into the d band, well beneath the 4s band. Type IA is characterized by solely "up" electrons at the Fermi level, exemplified by materials like CrO_2 and NiMnSb . In contrast, type IB features "down" electrons at the Fermi level, as seen in cases like $\text{Sr}_2\text{FeMoO}_6$.

Type-II Half-Metals: In this type, electrons are localized, and conduction ensues through hopping between sites with the same spin. An example of type IIB half-metal is magnetite. Coey and Venkatesan's categorization offers a comprehensive framework for understanding the diverse configurations and behavior of half-metals based on their electronic properties and spin polarization characteristics.

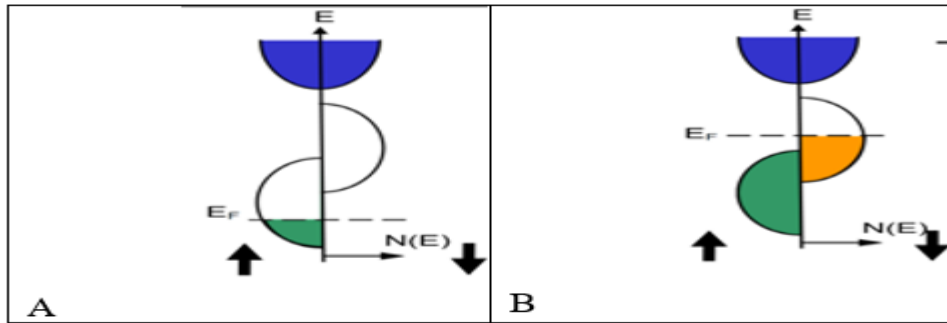


Figure I.9: Density of states of a type I or type II half-metal. Type II half-metals differ from type I half-metals in that the d-band is sufficiently narrow for electrons to be localized. Type A half-metals are conducted by up electrons, while type B half-metals are conducted by down electrons.

Type-III half-metals: "up" electrons at the Fermi level are localized and "down" ones delocalized, or vice versa. Electrons of a single spin orientation contribute significantly to conduction, due to a large difference in effective masses between "up" and "down" electrons. $\text{La}_{0.7}\text{Sr}_{0.3}\text{MnO}_3$ is type IIIA, as it is the "up" electrons that contribute to conduction.

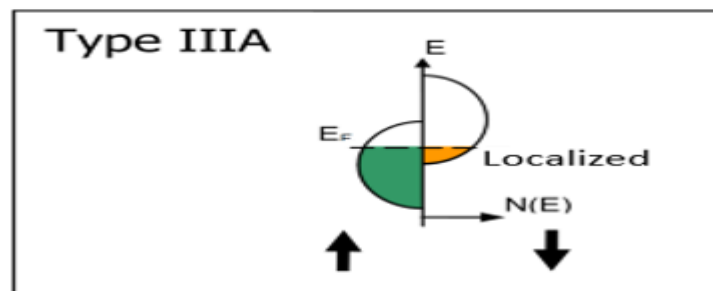


Figure I.10: density of States for a class IIIA half-metal.

It is classed as type IIIA because there are states accessible at the Fermi level for both "up" and "down" spins. However, the "down" spin electrons are confined, thus only the "up" electrons engage in conduction.

Type-IV half-metals: These are magnetic half-metals with a large difference in effective mass between, for example, down-spin electrons and up-spin holes. $\text{Tl}_2\text{Mn}_2\text{O}_7$ is of type IVB, and is currently the only known ferromagnetic half-metal. A half-metal, such as bismuth or graphite, is generally non-magnetic and has a small, equal number of electrons and holes due to a slight overlap between the valence and conduction bands.

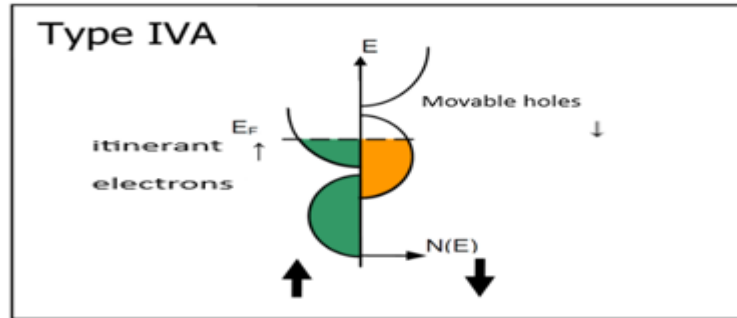


Figure I.11: Density of states of an IVA half-metal type. Type IV refers to half-metals. Here, the "up" spin electrons are itinerant and the "down" spin electrons are localized.

Type-V half-metals: This refers to magnetic semiconductors, such as (GaMn)As, in which the valence bands for the two spin orientations are shifted relative to each other, creating "down" spin holes, for example. EuO and GaN:Mn are VA and SnO₂:Fe are VB. A magnetic semiconductor can be a half-metal if one of these three conditions is met: the valence bands for the two spin orientations are offset from each other so that the Fermi level passes through an energy gap for one of the two spin directions, the conduction bands for the two spin orientations are offset from each other so that the Fermi level passes through an energy gap for one of the two spin directions, the dopant creates a band for which the Fermi level passes through an energy gap for one of the two spin directions.

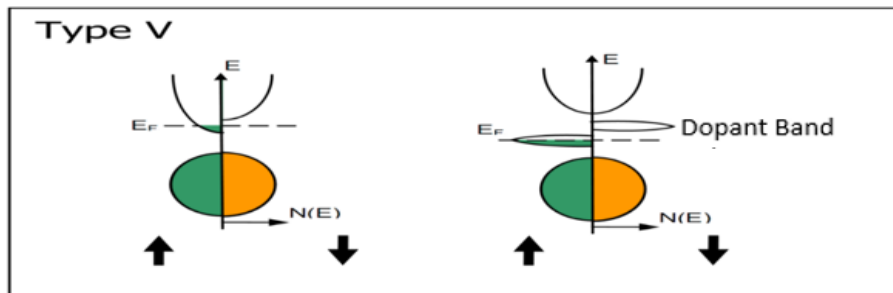


Figure I.12: Two types of density of states of a VA-type half-metal.

It concerns magnetic semiconductors, such as (GaMn)As. On the left, the conduction bands are shifted for both spin directions, and the Fermi level passes through an energy gap for the "down" spin. On the right, the dopant bands are shifted for both spin directions, and the Fermi level passes through an energy gap for the "down" spin.

References

- [1] B. HAMRI, Investigation théorique des propriétés structurales, électroniques et magnétiques des alliages heusler Ti_2VZ ($Z = Ge, Sn, Pb$), in, 2016.
- [2] S. Chikazumi, Magnetism-from fundamentals to nanoscale dynamics, New York: Oxford University Press, (1999).
- [3] G. Jonker, J. Van Santen, Ferromagnetic compounds of manganese with perovskite structure, *physica*, 16 (1950) 337-349.
- [4] J.B. Goodenough, A. Wold, R. Arnott, N. Menyuk, Relationship between crystal symmetry and magnetic properties of ionic compounds containing Mn^{3+} , *Physical Review*, 124 (1961) 373.
- [5] C. Zener, Interaction between the d-shells in the transition metals. II. Ferromagnetic compounds of manganese with perovskite structure, *Physical Review*, 82 (1951) 403.
- [6] C. Zener, Interaction between the d shells in the transition metals, *Physical Review*, 81 (1951) 440.
- [7] e.P. Bruno, C. Chappert, Oscillatory coupling between ferromagnetic layers separated by a nonmagnetic metal spacer, *Physical review letters*, 67 (1991) 1602.
- [8] M. Julliere, Tunneling between ferromagnetic films, *Physics letters A*, 54 (1975) 225-226.
- [9] M. Johnson, R.H. Silsbee, Interfacial charge-spin coupling: Injection and detection of spin magnetization in metals, *Physical review letters*, 55 (1985) 1790.
- [10] M.N. Baibich, J. Broto, A. Fert, F.N. Van Dau, F. Petroff, P. Etienne, G. Creuzet, A. Friederich and J. Chazelas, *Phys. Rev. Lett*, 61 (1988) 2472.
- [11] G. Binasch, P. Grünberg, F. Saurenbach, W. Zinn, Enhanced magnetoresistance in layered magnetic structures with antiferromagnetic interlayer exchange, *Physical review B*, 39 (1989) 4828.
- [12] T. Graf, F. Casper, J. Winterlik, B. Balke, G.H. Fecher, C. Felser, Crystal structure of new Heusler compounds, *Zeitschrift für anorganische und allgemeine Chemie*, 635 (2009) 976-981.
- [13] J. Moodera, L. Kinder, J. Nowak, P. LeClair, R. Meservey, Geometrically enhanced magnetoresistance in ferromagnet–insulator–ferromagnet tunnel junctions, *Applied Physics Letters*, 69 (1996) 708-710.
- [14] S. Kämmerer, A. Thomas, A. Hütten, G. Reiss, Co_2MnSi Heusler alloy as magnetic electrodes in magnetic tunnel junctions, *Applied Physics Letters*, 85 (2004) 79-81.
- [15] J. Kübler, A. William, C. Sommers, Formation and coupling of magnetic moments in Heusler alloys, *Physical Review B*, 28 (1983) 1745.

- [16] J. De Teresa, A. Barthélémy, A. Fert, J. Contour, R. Lyonnet, F. Montaigne, P. Seneor, A. Vaures, Inverse tunnel magnetoresistance in Co/SrTiO₃/La_{0.7}Sr_{0.3}MnO₃: new ideas on spin-polarized tunneling, *Physical Review Letters*, 82 (1999) 4288.
- [17] J.M. De Teresa, A.s. Barthélémy, A. Fert, J.P. Contour, F. Montaigne, P. Seneor, Role of metal-oxide interface in determining the spin polarization of magnetic tunnel junctions, *Science*, 286 (1999) 507-509.
- [18] R.A. De Groot, F.M. Mueller, P.v. van Engen, K. Buschow, New class of materials: half-metallic ferromagnets, *Physical review letters*, 50 (1983) 2024.
- [19] G. Hu, Y. Suzuki, Negative Spin Polarization of Fe₃O₄ in Magnetite/Manganite-Based Junctions, *Physical review letters*, 89 (2002) 276601.
- [20] R. Soulen Jr, J. Byers, M. Osofsky, B. Nadgorny, T. Ambrose, S. Cheng, P.R. Broussard, C. Tanaka, J. Nowak, J. Moodera, Measuring the spin polarization of a metal with a superconducting point contact, *science*, 282 (1998) 85-88.
- [21] A. Gupta, J. Sun, Spin-polarized transport and magnetoresistance in magnetic oxides, *Journal of magnetism and magnetic materials*, 200 (1999) 24-43.
- [22] Y. Ji, G. Strijkers, F. Yang, C. Chien, J. Byers, A. Anguelouch, G. Xiao, A. Gupta, Determination of the spin polarization of half-metallic CrO₂ by point contact Andreev reflection, *Physical Review Letters*, 86 (2001) 5585.
- [23] Y. Sakuraba, J. Nakata, M. Oogane, H. Kubota, Y. Ando, A. Sakuma, T. Miyazaki, Huge spin-polarization of L21-ordered Co₂MnSi epitaxial Heusler alloy film, *Japanese journal of applied physics*, 44 (2005) L1100.
- [24] M. Bowen, M. Bibes, A. Barthélémy, J.-P. Contour, A. Anane, Y. Lemaitre, A. Fert, Nearly total spin polarization in La_{2/3}Sr_{1/3}MnO₃ from tunneling experiments, *Applied Physics Letters*, 82 (2003) 233-235.
- [25] J. Braden, J. Parker, P. Xiong, S. Chun, N. Samarth, Direct measurement of the spin polarization of the magnetic semiconductor (Ga, Mn) As, *Physical review letters*, 91 (2003) 056602.
- [26] M. Bibes, K. Bouzehouane, A. Barthélémy, M. Besse, S. Fusil, M. Bowen, P. Seneor, J. Carrey, V. Cros, A. Vaures, Tunnel magnetoresistance in nanojunctions based on Sr₂FeMoO₆, *Applied Physics Letters*, 83 (2003) 2629-2631.
- [27] T.-S. Choy, J. Chen, S. Hershfield, Correlation between spin polarization and magnetic moment in ferromagnetic alloys, *Journal of applied physics*, 86 (1999) 562-564.
- [28] J. Coey, M. Venkatesan, Half-metallic ferromagnetism: Example of CrO₂, *Journal of Applied Physics*, 91 (2002) 8345-8350.

Chapter II
Fundamentals
of Heusler
Alloys

II.1. Introduction

Since its inception in 1988, when Albert Fert's team in France and Peter Grünberg's team in Germany made the groundbreaking discovery of giant magneto-resistance an achievement that earned them the 2007 Nobel Prize in Physics spintronics has become a crucial foundation of information storage technology. Revisiting this pivotal discovery is essential, as it marked the first use of electron spin polarization in charge transport within electronics. This phenomenon involves manipulating the magnetization orientation in devices using external stimuli, such as magnetic fields, by leveraging the quantum spin properties of electrons. The notion of this influence was initially postulated by Mott in 1936 and subsequently underwent empirical validation and theoretical elucidation in the late 1960s [1].

Recently, there has been a surge of interest in spintronics applications focusing on Heusler alloys that exhibit partial magnetism[2]. The Heusler alloy class includes more than 3000 recognized compounds, first discovered by Fritz Heusler in 1903 during his investigation of the ferromagnetic properties of the Cu₂MnAl alloy[3].

The primary combinations of Heusler alloys are visually depicted in the accompanying illustration. Due to their versatile range of properties, these compounds exhibit characteristics similar to those of half-metals, semiconductors, superconductors, and a variety of other materials.

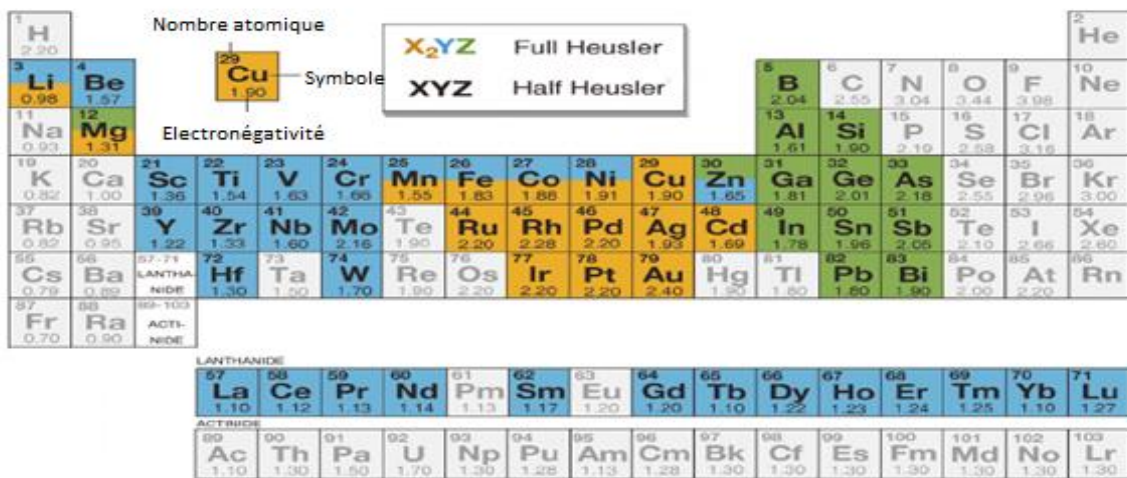


Figure II.1: Periodic Table of Elements showing possible combinations of Heusler alloys.

Surprisingly, the properties of numerous Heusler compounds can be predicted through valence electron calculations[4]. For instance, non-magnetic Heusler compounds with approximately 27 valence electrons are known to be superconductors.

Conversely, a significant subgroup of Heusler compounds consists of semiconducting alloys, with over 250 distinct combinations. These alloys are considered pioneering resources for energy-related applications. By simply adjusting their chemical composition, a wide range of band gaps, from 0 to 4 eV, can be achieved, demonstrating their versatility in advancing energy technologies.

II.2. Heusler alloys

The arrangement of atoms in Heusler phases is dictated by their electronegativity. These compounds adopt the crystalline structure of Cu_2MnAl and have a general formula of X_2YZ , conforming to the $\text{Fm}3\text{m}$ space group[5]. Typically, X and Y represent transition metals, while Z is either a non-magnetic metal or a non-metal element.

However, there are exceptions, such as LiCu_2Sb and YPd_2Sb , where the sequence is more adaptable and guided by the positioning of the most electropositive element. According to the nomenclature established by the International Union of Pure and Applied Chemistry (IUPAC), the most electropositive element is listed first in these cases[6].

II.2.1. Half Heusler

Due to their recently discovered atypical physical attributes, half-Heusler compounds are attracting considerable interest. These half-Heusler (HH) alloys, characterized by a cubic C1b crystal structure, represent an extraordinary category of compounds, exhibiting a wide range of intriguing properties and applications[7].

In the XYZ composition of the half-Heusler structure, Z is a main group element, while X and Y are transition metals[8].

II.2.2. Full Heusler

The designation "full-Heusler" is frequently used to refer to a category of intermetallic compounds identified by the chemical formula X_2YZ . In this formula, X and Y symbolize transition metals, while Z pertains to an element within groups III to V of the periodic table. This formulation highlights the repetition of the metal (X) twice at the beginning of the formula, representing the more electropositive element. Conversely, the more electronegative element is positioned at the end of the formula. However, there are instances where Y is substituted by either a rare earth element or an alkaline earth metal.

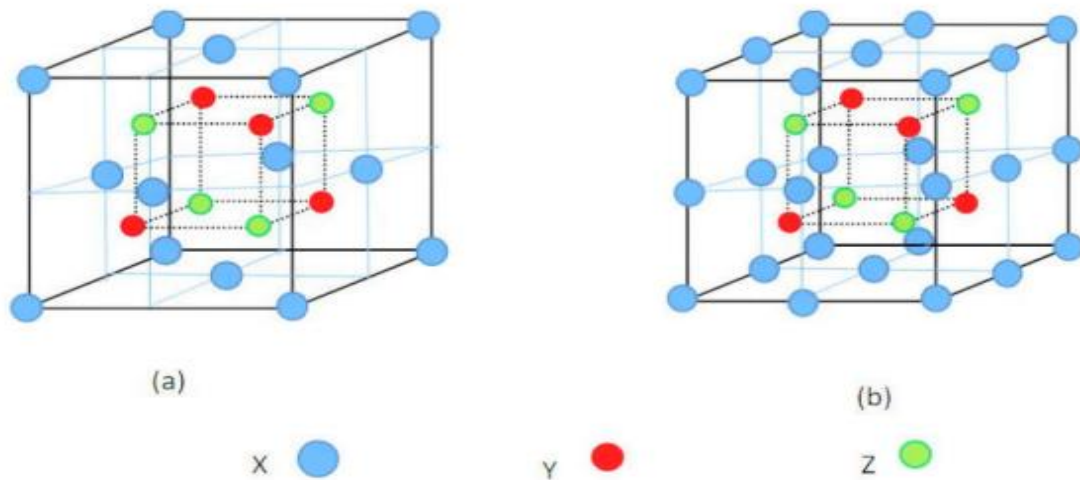


Figure II.2: Representative diagrams of the cubic meshes of a full Heusler alloy and a half Heusler alloy.

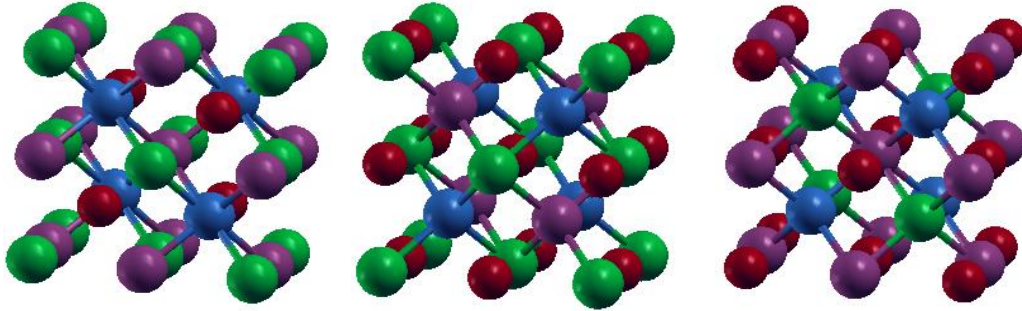
II.2.3. Quaternary Heusler alloys

Another category of Heusler alloys is known as quaternary Heusler compounds, consisting of four distinct chemical elements. This composition involves two different elements, X and X', located at the 4a and 4d sites respectively. Meanwhile, the Y element is positioned at the 4b site, and element Z occupies the 4c positions.

These compounds adopt a structure similar to the $\text{LiMgPbSb}[9]$ type, characterized by the $F-43m$ (N 216) space group and the chemical formula $XX'YZ$. Here, X, X', and Y represent transition metals, while Z denotes an element from the sp group. Notably, X' atoms typically have a lower valence than X atoms, and Y atoms exhibit a valence lower than both X and X'.

Tableau II.1: Atomic Sites of Inequivalent Combinations in Quaternary Heusler Alloys

Element	X	X'	Y	Z
Type I	$4c(1/4, 1/4, 1/4)$	$4d(3/4, 3/4, 3/4)$	$4d(3/4, 3/4, 3/4)$	$4d(3/4, 3/4, 3/4)$
Type II	$4b(1/2, 1/2, 1/2)$	$4d(3/4, 3/4, 3/4)$	$4c(1/4, 1/4, 1/4)$	$4a(0,0,0)$
Type III	$4a(0,0,0)$	$4d(3/4, 3/4, 3/4)$	$4b(1/2, 1/2, 1/2)$	$4c(1/4, 1/4, 1/4)$

**Figure II.3:** Crystal structure of quaternary-Heusler (Type I, Type II, Type III).

II.2.4. Double half-Heusler

The search for novel materials, such as Heusler alloys, has captured the scientific community's attention [10, 11] due to their remarkable properties including phase transitions, magneto-resistance, spintronic applications, half-metallicity, and shape memory effects [12, 13]. Heusler alloys are undergoing intensive theoretical and experimental investigation [14, 15].

Recently, double half-Heusler (DHH) materials have also garnered significant interest worldwide. One major attraction is their potential applications across various fields. Based on the substitution sites in the XYZ phase, double half-Heusler compounds are categorized into three groups with the following formulas: $X'X''Y_2Z_2$, $X_2Y'Y''Z_2$, and $X_2Y_2Z'Z''$. Heat transport in double half-Heuslers is constrained by disordered scattering, primarily affecting low-frequency phonon modes with reduced group velocities.

A notable example is the synthesis of the double half-Heusler compound $Ti_2FeNiSb_2$ [16], which exhibits significantly lower lattice thermal conductivity compared to $TiCoSb$. Using first-principal approaches, researchers have computed and investigated the structural, elastic, electrical, optical, and vibrational characteristics of $Ti_2FeNiSb_2$ and Ti_2Ni_2InSb DHH compounds [17].

II.3. Classification and crystal structure of Heusler alloys

Heusler alloys can be classified into two primary categories based on their atomic and crystal structures. This classification hinges on how atoms are arranged within the crystal lattice. Changes in the distribution of atoms at lattice sites can profoundly impact the electronic configuration of Heusler alloys, potentially altering their magnetic and transport properties[18, 19]. The ordering of atoms plays a crucial role in determining the properties of Heusler alloys. These atoms are arranged in specific structures such as the C1b and L21 for half-Heuslers, and the Y-type structure for full-Heuslers, respectively.

II.3.1. Crystal structure of half-Heusler alloys

The alloys in this category follow a chemical composition of the form XYZ. Half-Heusler alloys are intermetallic ternary compounds characterized by two distinct types of transition metals, denoted as X and Y, with Z serving as a sp-element with a specific valence. These alloys adopt a cubic C1b crystalline structure.

This structural type can be defined by three face-centered cubic (fcc) sublattices, each populated by atoms X, Y, and Z[20]. This arrangement is typical for this structural type, where the Wyckoff positions are designated as 4a (0,0,0), 4b (1/2,1/2,1/2), and 4c (1/4,1/4,1/4). Table II.2 provides a comprehensive overview of these distinct possibilities.

Table II. 2: Different possibilities for occupying non-equivalent sites in the C1b half-Heusler structure.

	X	Y	Z
1st arrangement	4a	4b	4c
2nd arrangement	4b	4c	4a
3rd arrangement	4c	4a	4b

The C_{1b} half-Heusler structure resembles a ZnS sublattice, incorporating both the 4a and 4c positions and extending to occupy the 4b octahedral sites. This representation effectively explains the covalent bonding interaction between the two elements present in this alloy. According to this explanation, atoms occupying the 4a and 4b sites form a Rock-Salt (NaCl) sublattice, where the ionic arrangement depends on the specific chemical properties of the constituent elements.

II.3.2. Crystal structure of full-Heusler alloys

Taking Cu_2MnAl as a paradigm, Full-Heusler compounds adopt the $L2_1$ structure, corresponding to the $Fm\bar{3}m$ space group (space group number 225)[21, 22]. In this structure, the X atoms are located at position 8c (1/4, 1/4, 1/4), while the Y and Z atoms occupy positions 4a (0, 0, 0) and 4b (1/2, 1/2, 1/2), respectively.

In addition to the $L2_1$ structure, there exists another configuration known as the inverse Heusler structure. This occurs when the atomic number of Y, which is within the same period as X, exceeds that of X ($Z(Y) > Z(X)$). This phenomenon is observed in transition metal alloys spanning different periods[23]. The formula $(XY)X'Z$ is typically used to distinguish between inverse and direct Heusler alloys. The inverse Heusler structure is commonly found in materials where $Z(Y) > Z(X)$, illustrated in Figure II.4. An example of such a structure is Mn_2CoSn or $(\text{MnCo})\text{MnSn}$ [24, 25].

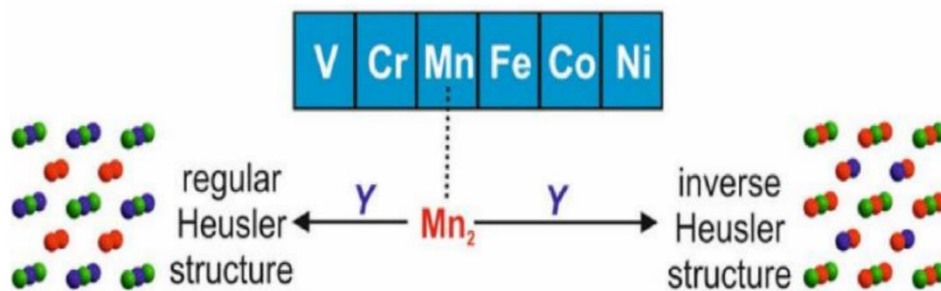


Figure II.4: Regular and inverse two structures for Mn_2 -based Heusler alloys depending on the position of the Y element[21].

II.4. Magnetism of Heusler alloys

In 1903, F. Heusler made a significant discovery when he observed that the combination Cu_2MnAl exhibited ferromagnetic properties despite the non-ferromagnetic nature of its constituent elements[3]. However, it took thirty years to confirm that the crystal structure was indeed face-centered cubic [22, 23].

Unfortunately, these findings faded into obscurity over the following decades, with only a few studies focusing on synthesizing innovative Heusler compounds emerging in the 1970s[26, 27]. Scientific interest in Heusler materials saw a resurgence when de Groot et al[2] predicted the presence of half-metallic ferromagnetism in MnNiSb , followed by Kübler et al.'s prediction for Co_2MnSn in 1983[28].

As illustrated in Figure II.5, XYZ materials exclusively accommodate magnetic moments on octahedral sites, forming an effective magnetic sublattice. As noted in Section I.4.2, the only instances of magnetic half-Heusler materials with the XYZ formula are found for Mn and Re. This phenomenon is attributed to the localization of the magnetic moment carried by the four 3D electrons in Mn^{3+} and the four f electrons.

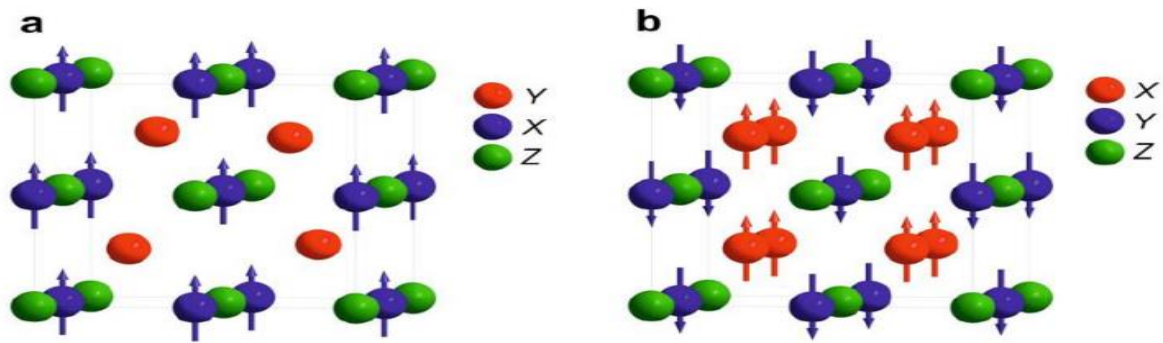


Figure II.5: (a) Half-Heusler alloys of the XYZ type. (b) X_2YZ Heusler alloys

II.5. Half-metallicity of Heusler alloys

In their investigation of the band structure of half-Heusler alloys, Groot et al[2] introduced the term "half-metallicity" for the first time[29]. Using NiMnSb as an example, conventional ferromagnetic materials exhibit a density of electronic states ($N(E_F)$) at the Fermi level for both majority spin electrons (up: $N\uparrow(E_F)$) and minority spin electrons (down: $N\downarrow(E_F)$)[30]. Half-metallic materials ($P = 1$) display markedly different conduction properties between minority and majority spins. They exhibit metallic behavior for one spin direction (having a non-zero density of states at the Fermi level), while showing semiconducting or insulating characteristics for the other spin direction. This results in a spin polarization of 100%, as depicted in Figure II.6.

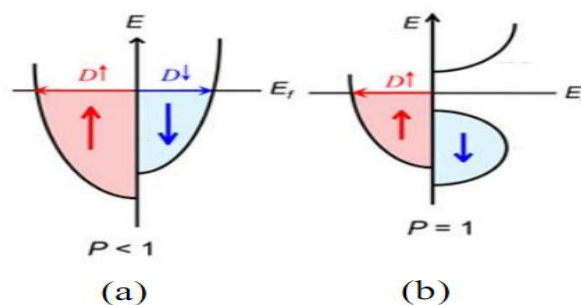


Figure II.6: Band structure for a (a) conventional ferromagnetic and (b) half-metallic material [33].

Since Groot's seminal study[2], a diverse range of substances have been recognized as half-metals, including Heusler alloys, CrO_2 [31], and graphene[32]. Half-metallic materials are notable for their unique conduction properties, potentially achieving 100% spin polarization and exhibiting strong magnetoresistive effects such as tunnel magnetoresistance and giant magnetoresistance.

Band structure calculations play a crucial role in understanding the electronic structure that determines the magnetic and half-metallic properties of Heusler alloys. Following the initial synthesis of cobalt-based Heusler alloys in the 1970s, Kübler[33] reported the first indications of half-metallicity in layers of Co_2MnAl and Co_2MnSn , while Ishida[34] discovered half-metallic behavior in Co_2MnSi and Co_2MnGe layers. Co_2FeSi [35, 36] has also been identified as exhibiting half-metallic behavior both experimentally and theoretically.

II.5.1. Half-metallic ferromagnetism

The study of the electronic structure of various Heusler compounds in the 1980s was driven by their unique magneto-optical properties, which led to unexpected discoveries. Certain Heusler materials exhibit half-metallic ferromagnetism, where they display metallic behavior for one spin orientation and insulating characteristics for the opposite spin orientation simultaneously[33, 37]. De Groot et al. distinguished three different forms of half-metallic ferromagnetism, establishing a categorization system [38].

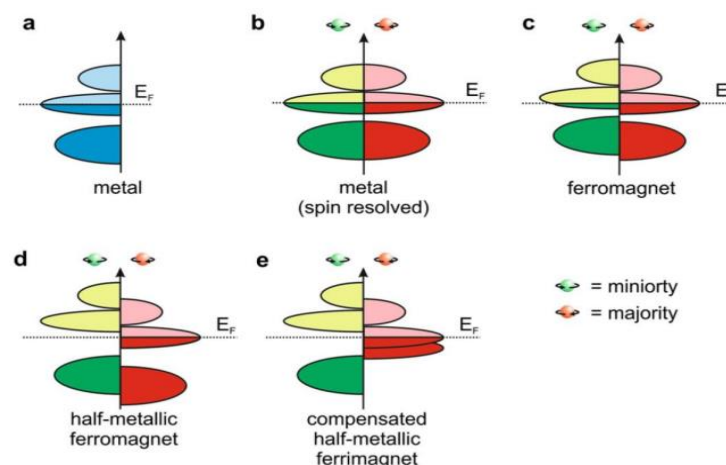


Figure II.7: Schematic illustration of the density of states of (a) a metal, (b) a metal (spin polarised), (c) a ferromagnet, (d) a half-metallic ferromagnet, and (e) a half-metallic ferrimagnetic half-metallic.

Figure.II.7 shows a schematic illustration of the density of states (DOS) (a) a metal with a density of states at the Fermi level, and (b) a spin-polarized representation of a metal: the two states are identical in both spin directions and equally occupied, (c) shows the DOS of a ferromagnetic material, in which the majority and minority states are shifted with respect to each other, leading to a measurable magnetisation. ferromagnetic (HMF) which behaves like a metal for one spin orientation and like an insulator for the other spin orientation.

II.5.2. Slater–Pauling rule

Heusler alloys, intermetallic compounds based on transition metals, exhibit more localized magnetism rather than itinerant features. Explaining the origin of magnetism in these alloys is highly challenging, as the magnetic moments of these materials vary with the crystal structure and the number of valence electrons (N_v). This behavior is referred to as the Slater-Pauling rule [39-41].

According to Slater and Pauling[39, 40], the magnetic moment of a metal can be predicted based on the number of valence electrons it possesses.

The total magnetic moment is shown against the number of valence electrons in **Figure II.8** (Slater-Pauling behavior). The positive component ($+B/1e$) and the negative part ($-B/1e$).The magnetic moment per atom is given by the relationship:

$$m \approx N_v - 6 \quad \text{II.1}$$

Where N_v is the number of valence electrons

The total magnetic moment is given by the number of majority electrons in excess ($0\uparrow$) compared to the minority electrons ($N\downarrow$):

$$M = N\uparrow - N\downarrow \quad \text{II.2}$$

The number of valence electrons per cell is determined by:

$$N_v = N\uparrow + N\downarrow \quad \text{II.3}$$

and the total magnetic moment becomes:

$$M_{\text{totale}} = N_v - 24 \quad \text{II.4}$$

This relationship is called the generalized Slater-Pauling rule, it is used to determine their magnetic moments.

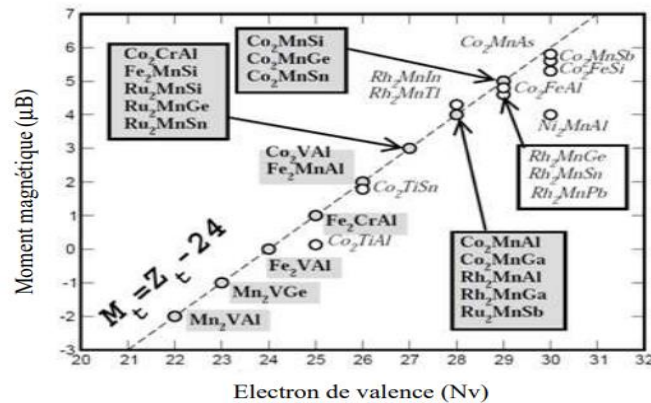


Figure II.8: Slater-Pauling curve for 3d alloys as a function of the number of valence electrons [41].

II.5.3. Relationship between disorder and spin polarization

To better understand the relationship between atomic disorder and spin polarization, Miura and colleagues[18] conducted theoretical studies on the electronic structure of the Heusler alloy $\text{Co}_2\text{Cr}_x\text{Fe}_{1-x}\text{Al}$ using first-principles calculations. Their findings indicate that the spin polarization remains high (over 90%) for the parent compound Co_2CrAl , even when Cr and Al atoms are completely exchanged.

This disorder does not significantly affect the electronic structure around the Fermi level, meaning the semiconducting nature of the minority states is preserved in both the L21 and disordered B2 structures. However, increasing the Fe concentration in both the L21 and disordered B2 structures reduces the spin polarization in the $\text{Co}_2\text{Cr}_x\text{Fe}_{1-x}\text{Al}$ alloy.

This polarization has been evaluated at 90% for the L21 structure and 70% for the B2 structure, respectively[42]. An exchange between Co and Cr atoms exhibits a different behavior, leading to a significant reduction in spin polarization. Additionally, the total magnetic moment is linearly reduced by $3 \mu_B$ per formula unit with an increasing amount of Co-Cr disorder.

II.6. Gap origin in half-Heusler alloys

Heusler alloys are half-metallic ferromagnetic materials (HMFs), exhibiting metallic behavior for the majority spins and semiconducting behavior with a band gap for the minority spins[43]. Numerous studies have explored this electrical feature by identifying the

source of the band gap. Ishida et al. provided the first theoretical evidence for Co_2MnSi [44], while Galanakis et al. examined common cobalt-based full Heusler alloys such as Co_2MnGa and Co_2MnSn [38].

The origin of the band gap in Heusler alloys is due to the contribution of the orbitals of the elements X, Y, and Z, particularly the low energy s and p orbitals in their valence band. These orbitals do not directly contribute to the formation of the gap but are responsible for the localization and positioning of the Fermi level within the forbidden band[45]. According to Kübler, the filling of these electronic states at these energy levels starts with the 8 electrons of minor spins and then progresses to the major spins[46].

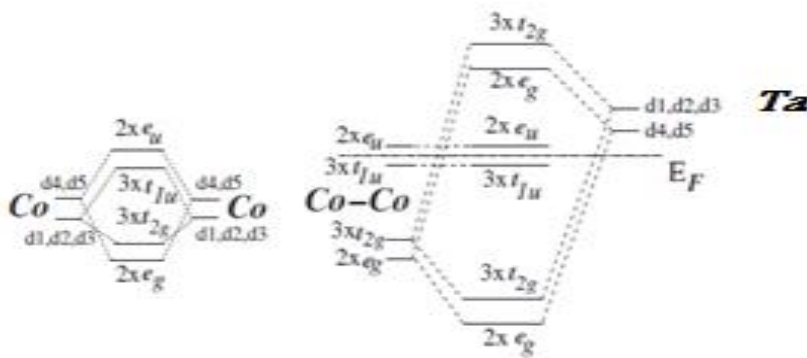


Figure II.9: Illustration of the origin of the gap and the hybridization of d states in Co_2YZ materials.

The d electronic states of the Co and Y atoms interact with each other, leading to the hybridization of doubly and triply degenerate states, specifically e_g (dx^2-y^2 , dz^2) and t_{2g} (d_{xy} , d_{yz} , d_{zx}), respectively (see Figure II.9). The strong hybridization of the d states arises from the interaction between X-X (Co-Co) atoms, generating bonding and antibonding states, along with the contribution from the Y element. This interaction results in the formation of a band gap between the antibonding t_{2g} and e_g states (see Figure II.10, where the notations d1 to d5 correspond to the orbitals d_{xy} , d_{yz} , d_{zx} , dx^2-y^2 , and dz^2 , respectively).

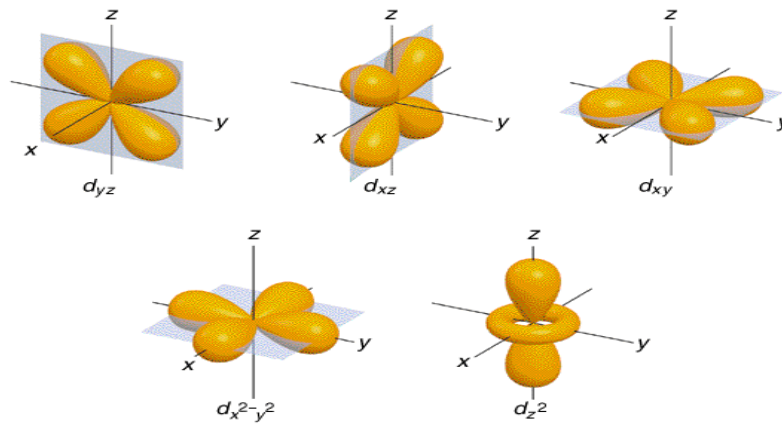


Figure II.10: Illustration of the degeneration of d orbitals into two levels e_g ($d_{x^2-y^2}, d_{z^2}$) and t_{2g} (d_{xy}, d_{yz}, d_{zx}).

II.7. Applications of the Heusler alloys:

Heusler alloys have recently garnered significant attention due to their diverse characteristics, making them ideal for various device applications. One of their most notable features is their half-metallic nature, which has driven extensive research. This property makes them excellent candidates for electrodes in magnetic tunnel junctions[38].

A prominent practical application of these materials is in spin valves, which utilize their large magnetoresistance properties. A "spin valve" is an assembly of these materials designed to maximize magnetoresistance. This principle is crucial for the functioning of modern hard drive read heads, enabling their high performance.

Figure II.11 illustrates the principle of giant magnetoresistance. In this setup, there are two channels for current flow: one for spin-up electrons and one for spin-down electrons. In a conventional conductor, these channels are equivalent. However, in a ferromagnetic material, the difference between them can be substantial, depending on the density of states at the Fermi level. In the extreme case of a half-metal, only one channel, which is metallic, allows conduction, while the other, which is insulating, does not contribute to current flow.

Although Giant Magnetoresistance (GMR) was first identified in a Current-In-Plane (CIP) setup, the Current-Perpendicular-to-Plane (CPP) design has proven to have much more significant impacts. A spin valve consists of two ferromagnetic layers separated by a thin non-magnetic metal layer. The first layer is "pinned" by an antiferromagnetic substance, making it insensitive to mild magnetic fields, whereas the second layer is "free" and its magnetization can be influenced by the application of modest magnetic fields.

GMR spin valves significantly increased storage density, but with the advent of new, extremely fast technologies, spin-dependent tunneling devices have become the dominant technology. When the metal spacer in a GMR spin valve is replaced with an insulating layer, the magnetoresistance increases by a factor of 10. These new devices are known as Magnetic Tunnel Junctions (MTJs) or Tunnel Magnetoresistance devices (TMRs) because the effect is based on the tunneling of electrons through an insulating barrier[47].

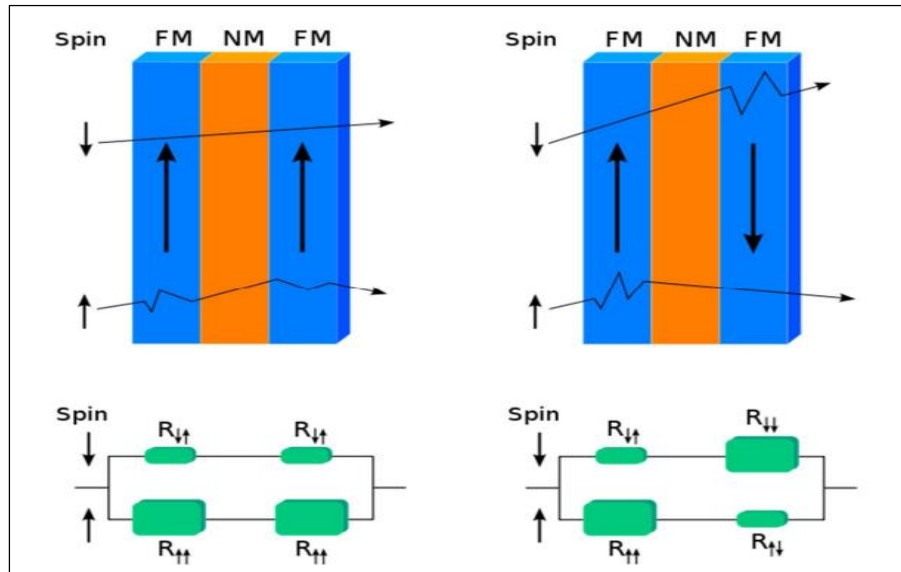


Figure II.11: Working principle of giant magnetoresistance (GMR)[48].

Conclusion

In this chapter, we have defined Heusler alloys and double half-Heusler materials, exploring their various properties and highlighting their broad and evolving field of applications. These materials offer numerous advantages and contributions, making them valuable for new technologies and applications across multiple sectors.

Double half-Heusler materials are a unique class with a wide range of properties and applications. They can be synthesized and characterized using various techniques, and their properties can be finely tuned by adjusting the composition of the two interpenetrating lattices. This tunability makes them highly versatile for specific applications.

Double half-Heusler materials are important due to their diverse applications and potential for further development. They are promising candidates for developing new materials with tailored properties for specific uses.

References

- [1] A. Fert, Giant magnetoresistance, *Scholarpedia*, 6 (2011) 6982.
- [2] R.A. De Groot, F.M. Mueller, P.v. van Engen, K. Buschow, New class of materials: half-metallic ferromagnets, *Physical review letters*, 50 (1983) 2024.
- [3] F. Heusler, Über magnetische manganlegierungen, *Verh. Dtsch. Phys. Ges*, 5 (1903) 219.
- [4] S. Peng, Y. Zhang, M. Wang, Y. Zhang, W. Zhao, Magnetic tunnel junctions for spintronics: principles and applications, *Wiley Encyclopedia of Electrical and Electronics Engineering*, (1999) 1-16.
- [5] P. Hohenberg, W. Kohn, *Phys Rev* 136: B864, Kohn W, Sham LJ (1965) *Phys Rev*, 140 (1964) A1133.
- [6] H. ZENASNI, Etude théorique des propriétés Magnétiques, électroniques et structurales des alliages Heusler, in, 2014.
- [7] T. Chibueze, A. Raji, C. Okoye, First principles study of the effects of doping with sp elements (As, Sb, Bi) and pressure on the properties of half-Heusler AuMnSn, *Chemical Physics*, 530 (2020) 110635.
- [8] R. Dahal, G.C. Kaphle, Structural, electronic and magnetic properties of XYZ type half-Heusler alloys, *Journal of Nepal Physical Society*, 5 (2019) 97-102.
- [9] X. Dai, G. Liu, G.H. Fecher, C. Felser, Y. Li, H. Liu, New quaternary half metallic material CoFeMnSi, *Journal of Applied Physics*, 105 (2009).
- [10] S.A. Sofi, S. Yousuf, T. Bhat, S. Singh, A.Q. Seh, M. Nabi, S. Khandy, S. Mir, N. Ganie, R. Mir, Investigation of pressure induced phase transition and thermoelectrics of semiconducting Fe₂ZrSi, in: *AIP Conference Proceedings*, AIP Publishing, 2020.
- [11] S.A. Sofi, D.C. Gupta, High temperature and pressure study on structural and thermophysical properties of Co₂XAl (X= Zr, Nb, Hf) Heusler materials by density functional theory calculations, *Philosophical Magazine*, 101 (2021) 1654-1678.
- [12] S.A. Sofi, S. Yousuf, D.C. Gupta, Prediction of robustness of electronic, magnetic and thermoelectric properties under pressure and temperature variation in Co₂MnAs alloy, *Computational Condensed Matter*, 19 (2019) e00375.
- [13] S.A. Sofi, S. Yousuf, T. Bhat, M. Nabi, S. Singh, Z. Saleem, S. Mir, S.A. Khandy, A.Q. Seh, D.C. Gupta, Investigation of structural and mechanical properties of ferromagnetic Co₂MnAs compound, in: *AIP Conference Proceedings*, AIP Publishing, 2019.
- [14] S.A. Sofi, D.C. Gupta, High Pressure-Temperature study on thermodynamics, half-metallicity, transport, elastic and structural properties of Co-based Heusler alloys: A first-principles study, *Journal of Solid State Chemistry*, 284 (2020) 121178.

- [15] S.A. Sofi, D.C. Gupta, Investigation of structural, elastic, thermophysical, magneto-electronic, and transport properties of newly tailored Mn-based Heuslers: A density functional theory study, *International Journal of Quantum Chemistry*, 120 (2020) e26216.
- [16] S. Anand, M. Wood, Y. Xia, C. Wolverton, G.J. Snyder, Double half-Heuslers, *Joule*, 3 (2019) 1226-1238.
- [17] G. Uğur, A. Kushwaha, M. Güler, Z. Charifi, Ş. Uğur, E. Güler, H. Baaziz, Electronic structure, optical and vibrational properties of $\text{Ti}_2\text{FeNiSb}_2$ and $\text{Ti}_2\text{Ni}_2\text{InSb}$ double half Heusler alloys, *Materials Science in Semiconductor Processing*, 123 (2021) 105531.
- [18] Y. Miura, K. Nagao, M. Shirai, Atomic disorder effects on half-metallicity of the full-Heusler alloys $\text{Co}_2(\text{Cr}_{1-x}\text{Fe}_x)\text{Al}$: A first-principles study, *Physical Review B*, 69 (2004) 144413.
- [19] S. Picozzi, A. Continenza, A. Freeman, Role of structural defects on the half-metallic character of Co_2MnGe and Co_2MnSi Heusler alloys, *Physical Review B*, 69 (2004) 094423.
- [20] P. Webster, K. Ziebeck, Alloys and compounds of d-elements with main group elements. Part 2, *Landolt-Bornstein, New Series, Group III*, 19 (1988) 75-184.
- [21] T. Graf, C. Felser, S.S. Parkin, Simple rules for the understanding of Heusler compounds, *Progress in solid state chemistry*, 39 (2011) 1-50.
- [22] A.J. Bradley, J. Rodgers, The crystal structure of the Heusler alloys, *Proceedings of the royal society of London. Series A, Containing Papers of a Mathematical and Physical Character*, 144 (1934) 340-359.
- [23] O. Heusler, Kristallstruktur und Ferromagnetismus der Mangan-Aluminium-Kupferlegierungen, *Annalen der Physik*, 411 (1934) 155-201.
- [24] V. Surikov, V. Zhordochkin, T.Y. Astakhova, Hyperfine fields in a new Heusler alloy Mn_2CoSn , *Hyperfine Interactions*, 59 (1990) 469-472.
- [25] N. Lakshmi, A. Pandey, K. Venugopalan, Hyperfine field distributions in disordered Mn_2CoSn and Mn_2NiSn Heusler alloys, *Bulletin of Materials Science*, 25 (2002) 309-313.
- [26] P. Webster, Magnetic and chemical order in Heusler alloys containing cobalt and manganese, *Journal of Physics and Chemistry of Solids*, 32 (1971) 1221-1231.
- [27] J. Brooks, J. Williams, Magnetic Hyperfine Interactions in the Ferromagnetic Heusler-Type Alloy Co_2TiSn Studied by Means of the Mössbauer Effect in ^{119}Sn , *physica status solidi (a)*, 32 (1975) 413-417.
- [28] H. Schuster, H. Hinterkeuser, W. Schaefer, G. Will, Investigations on neutron diffraction of the phases LiAlSi and LiAlGe , *Z. Naturforsch., B*, 31 (1976) 1540-1541.
- [29] J.S. Moodera, L.R. Kinder, T.M. Wong, R. Meservey, Large magnetoresistance at room temperature in ferromagnetic thin film tunnel junctions, *Physical review letters*, 74 (1995) 3273.

- [30] M. HEHN, F. MONTAIGNE, A. SCHUHL, Magnétorésistance géante et électronique de spin, *Techniques de l'ingénieur. Electronique*, 3 (2002) 1-15.
- [31] J. Coey, M. Venkatesan, Half-metallic ferromagnetism: Example of CrO₂, *Journal of Applied Physics*, 91 (2002) 8345-8350.
- [32] Y.-W. Son, M.L. Cohen, S.G. Louie, Half-metallic graphene nanoribbons, *Nature*, 444 (2006) 347-349.
- [33] J. Kübler, A. William, C. Sommers, Formation and coupling of magnetic moments in Heusler alloys, *Physical Review B*, 28 (1983) 1745.
- [34] S. Ishida, T. Masaki, S. Fujii, S. Asano, Theoretical search for half-metallic films of Co₂MnZ (Z = Si, Ge), *Physica B: Condensed Matter*, 245 (1998) 1-8.
- [35] K. Inomata, S. Okamura, A. Miyazaki, M. Kikuchi, N. Tezuka, M. Wojcik, E. Jedryka, Structural and magnetic properties and tunnel magnetoresistance for Co₂(Cr, Fe)Al and Co₂FeSi full-Heusler alloys, *Journal of Physics D: Applied Physics*, 39 (2006) 816.
- [36] Z. Gercsi, K. Hono, Ab initio predictions for the effect of disorder and quaternary alloying on the half-metallic properties of selected Co₂Fe-based Heusler alloys, *Journal of Physics: Condensed Matter*, 19 (2007) 326216.
- [37] C.M. Fang, G. De Wijs, R. De Groot, Spin-polarization in half-metals, *Journal of Applied Physics*, 91 (2002) 8340-8344.
- [38] I. Galanakis, P. Dederichs, N. Papanikolaou, Slater-Pauling behavior and origin of the half-metallicity of the full-Heusler alloys, *Physical Review B*, 66 (2002) 174429.
- [39] J.C. Slater, The ferromagnetism of nickel, *Physical Review*, 49 (1936) 537.
- [40] L. Pauling, The nature of the interatomic forces in metals, *Physical Review*, 54 (1938) 899.
- [41] I. Galanakis, Ph. Mavrapoulos, and PH Dederichs, *J. Phys. D: Appl. Phys.*, 39 (2006) 765.
- [42] Y. Miura, M. Shirai, K. Nagao, First-principles study on half-metallicity of disordered Co₂(Cr_{1-x}Fe_x)Al, *Journal of applied physics*, 95 (2004) 7225-7227.
- [43] S. Parkin, X. Jiang, C. Kaiser, A. Panchula, K. Roche, M. Samant, Magnetically engineered spintronic sensors and memory, *Proceedings of the IEEE*, 91 (2003) 661-680.
- [44] H. Xu, J. Gao, M. Li, Y. Zhao, M. Zhang, T. Zhao, L. Wang, W. Jiang, G. Zhu, X. Qian, Mesoporous WO₃ nanofibers with crystalline framework for high-performance acetone sensing, *Frontiers in Chemistry*, 7 (2019) 266.
- [45] S. Yusuf, A. Kumar, Neutron scattering of advanced magnetic materials, *Applied Physics Reviews*, 4 (2017).
- [46] J. Kübler, First principle theory of metallic magnetism, *Physica B+ C*, 127 (1984) 257-263.

[47] J.S. Moodera, J. Nassar, G. Mathon, Spin-tunneling in ferromagnetic junctions, Annual Review of Materials Science, 29 (1999) 381-432.

[48] M.B. ABBAR, Etude ab-initio des propriétés structurales, opto-électroniques et magnétiques des composés Heusler type A_3-xB_xC , (2018).

Chapter III

Theory and

Calculation Methods

III.1. Introduction

Understanding the physico-chemical properties of molecules or other substances relies on comprehending the state of the particles responsible for these qualities, namely electrons. In order to achieve this, early explorations into quantum mechanics aimed to devise an equation similar to classical mechanics, capable of effectively describing the movement of electrons in both space and time.

Although traditional calculation tools can be used to investigate the properties of any material and tackle the specific challenges of quantum mechanics, conventional mechanics has proven to be insufficient, necessitating the application of quantum mechanics with its foundation in the solution to the Schrödinger equation.

Solving the Schrödinger equation poses an immense challenge, bordering on the impossible. Since Dirac's initial approximation in 1929, which aimed to simplify the resolution of the characteristic equation for systems with multiple particles, there have been continuous advancements in methods and approximations for calculations. Over time, it has become increasingly evident that addressing such problems and solving systems with numerous atoms per unit cell requires the development of density functional theory (DFT) in conjunction with the local density approximation (LDA).

In this chapter, we will first present general information about the non-relativistic quantum processing of a system composed of several particles, then we will discuss the two main families of quantum calculations: the Hartree-Fock approximation and the processing of correlation. electronics on the one hand, and density functional theory on the other.

III.2. Schrödinger equation

In the general scenario, the computation of the overall energy within a system that involves interacting ions and electrons is achieved by solving the stationary states of the Schrödinger equation [1]:

$$\hat{H}\psi(\{r_i\}, \{R_I\}) = E\psi(\{r_i\}, \{R_I\}) \quad \text{III.1}$$

This constitutes an eigenvalue equation, where \hat{H} represents the Hamiltonian operator. It signifies a wave function of the system contingent upon the nuclei and electron coordinates. E denotes the complete energy of the system, symbolizing the collection of electron

coordinates, while symbolizing the compilation of nucleus coordinates. The Hamiltonian pertinent to this crystalline arrangement adheres to the subsequent structure:

$$H = T_e + T_N + V_{ee} + V_{eN} + V_{NN} \quad \text{III.2}$$

The total kinetic energy of the electrons:

$$T_e = \sum_{i=0}^{N_e} T_i = \sum_{i=0}^{N_e} \frac{(-\hbar^2 \Delta_i)}{2m_e} \quad \text{III.3}$$

Where m_e is the mass of the electron. The total kinetic energy of the nuclei:

$$T_N = \sum_{\alpha} T_{\alpha} = \sum_{\alpha=0}^{N_{\alpha}} \frac{(-\hbar^2 \Delta_{\alpha})}{2M_I} \quad \text{III.4}$$

Where M_I is the mass of the nucleus. The interaction energy of the electrons, two by two: $|\vec{r}_i - \vec{r}_j|$:

$$V_{e-e} = \frac{1}{2} \sum_{i,j \neq i} \frac{e^2}{|\vec{r}_i - \vec{r}_j|} = \frac{1}{2} \sum_{j \neq i} V_{ij} \quad \text{III.5}$$

The interaction energy of the nuclei two by two:

$$V_{N-N} = \frac{1}{2} \sum_{I \neq J}^K \frac{Z_I Z_J e^2}{|\vec{R}_I - \vec{R}_J|} = \frac{1}{2} \sum_{\alpha \neq \beta}^K V_{IJ} \quad \text{III.6}$$

Z_I and Z_J are the atomic numbers of the nuclei I and J. The energy of interaction nuclei-electrons:

$$V_{e-N} = - \sum_{i=1}^{N_e} \sum_{\alpha=1}^{N_{\alpha}} \frac{Z_{\alpha} e^2}{|\vec{r}_i - \vec{R}_{\alpha}|} = \sum_{i=1}^{N_e} \sum_{\alpha=1}^{N_{\alpha}} V_{i\alpha} \quad \text{III.7}$$

In what follows, we will use the atomic units, which are summarized in **Table III.1**

Table III.1: Atomic units.

Sizes	Symbol	SI unit	Atomic unit (u.a)
Mass of the electron	m_e	$9,109.10^{-31} \text{kg}$	1 u.a
Electron charge	e	$-1,022.10^{-19} \text{C}$	1 u.a
Cinematic moment	\hbar	$1,064.10^{-34} \text{J.S}$	1 u.a
Length (Bohr's radius)	$a_0 = \frac{4\pi\epsilon_0 \hbar}{m_e e^2}$	$0,52918.10^{-10} \text{m}$	1 u.a = 1 Bohr
Energy (Hartree)	$E_0 = \frac{\hbar^2}{m_e a_0^2}$	$4,3598.10^{-18} \text{J}$	1u.a = 1 Hartree

III.3. Born-Oppenheimer approximation

The objective of the Schrödinger equation's simplification is pursued through the approximation proposed by Born and Oppenheimer [2]. This approximation capitalizes on the substantial mass difference between electrons and nuclei. Consequently, postulating that a molecule's electrons maneuver within the confines of stationary nuclei stands as a preliminary yet fairly accurate approximation. This methodology leads to the kinetic energy of the nuclei being effectively nullified, while the potential energy arising from the nuclei's interactions remains constant. Consequently, the Hamiltonian H governing the system takes on the ensuing form:

$$H = T_e + V_{ee} + V_{eN} \quad \text{III.8}$$

The solution of the Schrödinger equation with this Hamiltonian:

$$H_e \psi_e = E_e \psi_e \quad \text{III.9}$$

Is just the electronic wave function describing the movement of electrons in the field of nuclei:

$$\psi_e = \psi_e(\{r_i\}, \{R_I\}) \quad \text{III.10}$$

Even if this approximation greatly simplifies equation (III.1) by decoupling the movement of electrons from that of nuclei, equation (III.9) still cannot be solved exactly because of the poly-electronic character of the wave function of the interacting electron system, so further simplifications must be applied.

Due to the intricate nature of the electron-electron interactions, this approximation is insufficient on its own to solve the Schrödinger equation. It is frequently connected to the Hartree and Hartree-Fock[3, 4] approximations because of this.

III.4. Hartree- Fock approximation

a- Hartree approximation

This is the first non-perturbative approximation that allows to approximately solve the Schrödinger electronic equation (III.1), it was introduced by Hartree in 1928[3], where he considered that the electrons are independent, that is to say each of them evolving in the field created by all the others. Therefore, the problem passes from a system of electron-

electron pair repulsion to a problem of a particle immersed in an average electrostatic field created by the charge distribution of all the other electrons.

Subsequently, the N-electron wave function Ψ_e reduces to a product of n single-electron single-electron wave functions Ψ_i , where the resulting function is called the Hartree wave function Ψ_H given by the following expression:

$$\Psi(\vec{r}) = \prod_{i=1}^n \Psi_i(\vec{r}_i) \quad \text{III.11}$$

Except that, in this framework, the electronic system is imperfectly described, the spin of the electrons and the Pauli exclusion principle are neglected. Which makes the call for another approximation important to better describe this term.

b- Spin-orbit:

The shape of the multi-electron wave function that clearly describes the behavior of the electron is determined from considerations that take into account the physics of the electron:

- (i) electrons are indistinguishable particles, electronic correlation must not be neglected.
- (ii) electrons are fermions characterized by spatial coordinates and spin coordinates (intrinsic angular momentum).

Because of the second point (ii), the total wave function must be antisymmetric with respect to the exchange of any two particles, which was neglected by Hartree.

In 1930, Fock[5] proposed taking into account the antisymmetry of the set to apply the Pauli exclusion principle, where the multi-electron wave function is written using a Slater determinant [05] as follows:

$$\Psi_{HF} = \frac{1}{\sqrt{N!}} \begin{vmatrix} \Psi_1(r_1) & \Psi_2(r_1) & \dots & \Psi_N(r_1) \\ \Psi_1(r_2) & \Psi_2(r_2) & \dots & \Psi_N(r_2) \\ \vdots & \vdots & \dots & \vdots \\ \Psi_1(r_N) & \Psi_2(r_N) & \dots & \Psi_N(r_N) \end{vmatrix} \quad \text{III.12}$$

Where each wave function is called orbital spin, because it is composed of two parts: a spatial orbital function and the other is a spin function (up or down), and $\frac{1}{\sqrt{N!}}$ is the normalization constant.

This maneuver respects the nature of electrons (fermions), so the Pauli principle is respected. Slater's determinant is determined using the variational principle. The application of the Hamiltonian on the wave function gives the Hartree-Fock energy:

$$E_{HF}\varphi_i(r_i) = \left(-\frac{\hbar^2}{2m} \nabla_{r_i}^2 + v_{eN}(r_i) + \sum J_j - K_j \right) \varphi_i(r_i) \quad \text{III.13}$$

The operator in parentheses is the Fock operator in which the term $-\frac{\hbar^2}{2m} \nabla_{r_i}^2$ corresponds to the kinetic energy of the electron i . The operator $v_{eN}(r_i)$ describes the electrostatic potential between this electron and the(s) nucleus(x). The operator J_j or Coulomb operator represents the average potential created by the other electrons and K_j , the exchange operator, the correction to this potential due to antisymmetry.

$$J_j\varphi_i(r_i) = \int \varphi_j^*(r) \frac{1}{|r-r_i|} \varphi_j(r) dr \quad \text{III.14}$$

$$K_j\varphi_i(r_i) = \int \varphi_j^*(r) \frac{1}{|r-r_i|} \varphi_i(r) dr \quad \text{III.15}$$

The difference between these two terms is the Hartree-Fock potential energy:

$$V_{HF}(\vec{r}_i) = \frac{1}{2} \sum_{j>i}^{Ne} [J_j(\vec{r}_i) - K_j(\vec{r}_i)] \quad \text{III.16}$$

So, the Hartree-Fock approximation takes into account interactions more finely, a whole category of methods based on this approach called "Configuration Interaction" (CI, Configuration Interaction) [6] treats the exchange term exactly. However, because of the very rapid increase in the number of configurations with the number of electrons involved, the correlations due to short-range Coulomb interactions are neglected, which limits the scope of these calculations to very small systems, for the treatment of extended systems such as solids, it remains difficult to apply. Therefore, this method does not allow to find the exact energy of the real system. These limitations have been partly circumvented by the density functional theory.

III.5. Density functional theory (DFT)

DFT stands as one of the most utilized methodologies for quantum computations pertaining to the electronic configuration of solids in the present era. This technique holds the capability to alleviate the intricacies of the task at hand, rendering the computation of a

multi-electron system's ground state attainable. In contemporary times, the advancement of materials holds profound implications for technological and industrial progress.

In accordance with density functional theory, a non-interacting system (referred to as "effective") can adequately encompass the intricacies of many-body phenomena, up to the Kohn-Sham hypothesis. This is accomplished by representing its Hamiltonian as a functional of the overall one-body density. However, as the theory doesn't furnish us with the specific form of this function, pragmatic applications necessitate the utilization of alternative approximations.

III.5.1. Hohenberg-Kohn theorems

The two theorems of Hohenberg and Kohn serve as the foundation for the formalism of density functional theory (DFT)[1].

Theorem 01:

"The potential $v_{ext}(r)$ for any interacting system of particles in an external potential is uniquely determined, up to an additive constant, by the density $n_0(r)$ of the particles in their ground state."

This theorem by Pierre Hohenberg and Walter Kohn shows that the electron density is the only function necessary to obtain all the electronic properties of a system. As initially demonstrated by Hohenberg and Kohn, due to the one-to-one correspondence existing between the external potential $v_{ext}(r)$ and the electron density $n_0(r)$ The expression for the electronic Hamiltonian is:

$$H = -\frac{1}{2} \sum_i^n \psi_i + \sum_{i>j} \frac{1}{r_{ij}} + v_{ext}(r_i) \quad \text{III.17}$$

$v_{ext}(r)$: External potential of the electron.

$n_0(r)$: Electronic density.

It is equal to N, the total number of electrons, when it is integrated over all space.

$$\int_0^\infty n(r) dr = N \quad \text{III.18}$$

The total energy of the system can be written as the sum of three functionals: that of the nucleus-electron potential energy, that of the kinetic energy, and that of the electron-electron potential energy.

$$E[n(r)] = \psi|H|\psi = V_{Ne}[n(r)] + T_e[n(r)] + V_{ee}[n(r)] \quad \text{III.19}$$

By asking:

$$V_{Ne}[n(r)] = \int n(r)v_{ext}(r)dr \quad \text{III.20}$$

$$T_e[n(r)] + V_{ee}[n(r)] = F[n(r)] \quad \text{III.21}$$

The energy functional is then written:

$$E[n(r)] = \int n(r)v_{ext}(r)dr + F[n(r)] \quad \text{III.22}$$

Where $F[n(r)]$ is the universal functional of Hohenberg and Kohn, which gathers all the terms independent of the external potential. This functional contains electron kinetic energy and electron-electron repulsive potential energy.

Theorem 02:

"There exists a universal functional $\mathbf{E}(\mathbf{n})$ that expresses the energy as a function of the electronic density $\mathbf{n}(\mathbf{r})$, valid for any external potential $\mathbf{v}_{ext}(\mathbf{r})$. For each specific $\mathbf{v}_{ext}(\mathbf{r})$, the energy of the system's ground state is the value that minimizes this functional, and the associated density $\mathbf{n}(\mathbf{r})$ corresponds to the exact density $\mathbf{n}_0(\mathbf{r})$ of the ground state."

This second theorem shows that the energy appears as a functional of the density, and that for any exterior potential, the density that minimizes this functional is the exact density of the ground state.

Let n be a density such that: $n(r) \geq 0$ And $\int_0^\infty n(r)dr = N$; so: $E[n(r)] > E_0$

This second theorem can be stated as follows: The energy associated with any density satisfying the boundary conditions and at a potential is greater than or equal to the energy associated with the ground state electron density.

Noticed:

This theorem is based on the variational principle analogous to that proposed in the Hartree-Fock approach for a functional of the wave function, but applied this time to a

functional of the electronic density: $\frac{\partial E[n(r)]}{\partial n} = 0$

III.5.2. Kohn-Sham method

The foundation of the Kohn-Sham theory[7] rests upon the concept that a supplementary system comprising non-interacting particles can emulate the ground state density of a system comprising N interacting particles. This assemblage of hypothetical independent particles evolves to create an effective potential, standing in for the authentic system comprised of interacting electrons. This potential operates within the confines of an exchange and correlation functional concerning the electron density, denoted by:

$$n(r) = \sum_{i=1}^n |\psi_i(r)|^2 \quad \text{III.23}$$

Where: $\psi_i(r)$ is the wave function of the i^{eme} electron. We use the variational principle to obtain the energy of the ground state and the density giving the functional $E[n(r)]$.

$$E[n(r)] = T_{fictif}[n(r)] + V_H[n(r)] + \int n(r)v_{ext}(r)dr + V_{xc}[n(r)] \quad \text{III.24}$$

$$E[n(r)] = T_{fictif}[n(r)] + \frac{1}{2} \int \frac{n(r)n(r')}{|r-r'|} drdr' + \int n(r)v_{ext}(r)dr + V_{xc}[n(r)] \quad \text{III.25}$$

With: $V_H = \frac{1}{2} \int \frac{n(r)n(r')}{|r-r'|} drdr'$: is the Hartree energy.

$V_{xc}[n(r)]$: The term that includes the effects of exchange and correlation.

T_{fictif} : is the kinetic energy of the ground state of our fictitious system.

Then we can write the Kohn-Sham equations:

$$H_{KS}\psi_i = \varepsilon_i\psi_i \quad \text{III.26}$$

$$(T_{fictif} + V_H + V_{xc} + v_{ext})\psi_i = \varepsilon_i\psi_i \quad \text{III.27}$$

III.5.3. Self-consistency in calculations

- 1- Use a test density as the calculation's starting point. Exactly an atomic superposition of densities.
- 2- Take samples from the Brillouin zone to determine the point-by-point density and exchange-correlation potential.
- 3- Determine the KS matrix.
- 4- To get the KS orbitals, solve the equations for the expansion coefficients.
- 5- Determine the updated density.
- 6- If the energy or density has significantly changed (convergence requirements), go to step1.
- 7- Proceed to the following step if the convergence requirements are fulfilled.
- 8- Complete the computation; end of calculation
- 9- This algorithm can be presented by the diagram below:

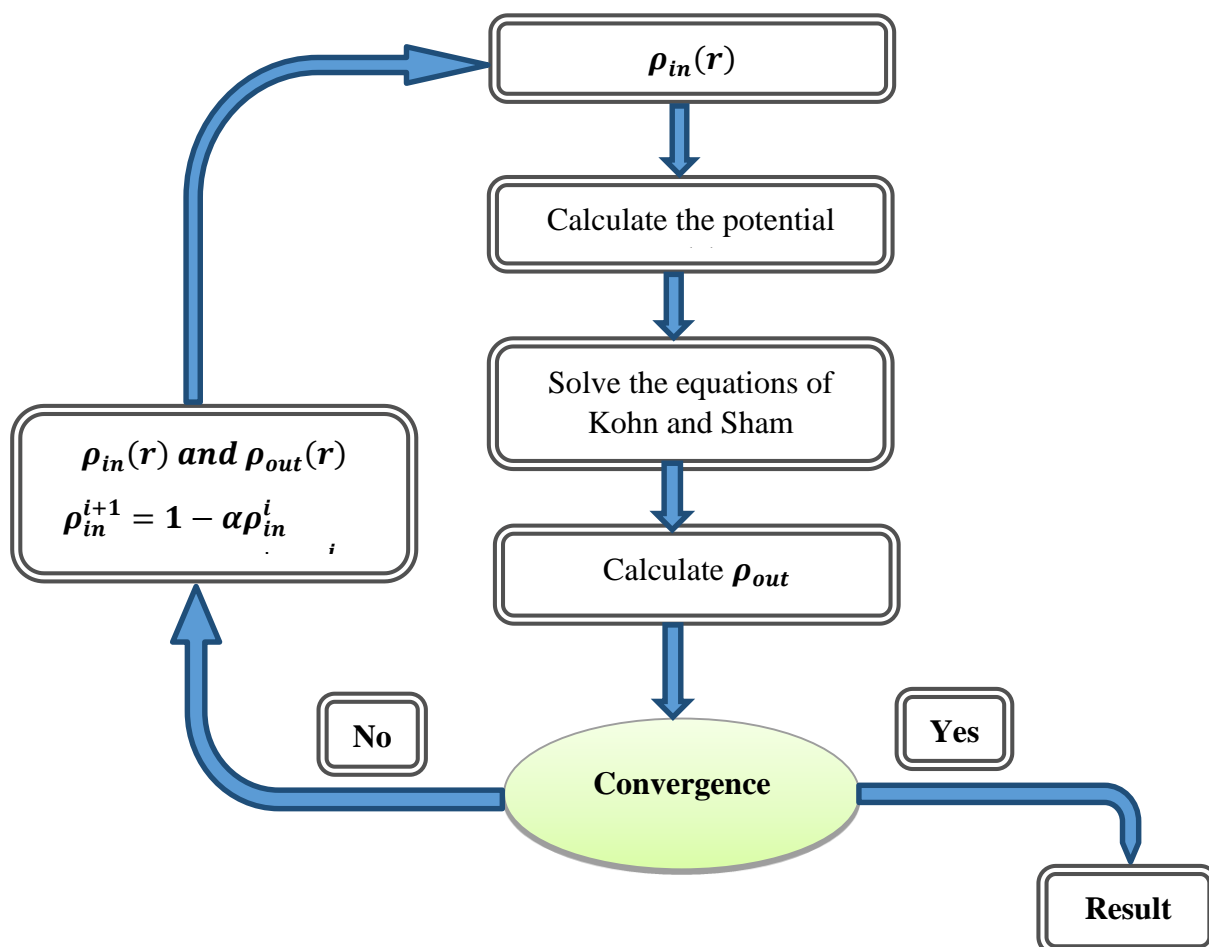


Figure III.1: Solution of the Kohn-Sham equations: Self-consistent cycle [8].

III.5.4. Exchange-correlation

The widely adopted technique for approximating the exchange-correlation term is the local density approximation, denoted as LDA[9]. The underlying concept involves regarding the exchange-correlation potential as a local parameter with a mild dependence on density fluctuations at a given position, r . This approximation forms the cornerstone of contemporary exchange-correlation functionals and can be defined as follows:

$$E_{xc}^{LDA}[n(r)] = \int n(r)\varepsilon_{xc}[n(r)]dr \quad \text{III.28}$$

Where: $E_{xc}^{LDA}[n(r)]$: is the exchange and correlation energy per electron in an electron gas whose distribution is assumed to be uniform.

$\varepsilon_{xc}[n(r)]$: is the exchange-correlation energy per particle of the uniform electron gas of density $n(r)$. Furthermore, $\varepsilon_{xc}[n(r)]$ can be considered as the sum of an exchange and correlation contribution:

$$\varepsilon_{xc}[n(r)] = \varepsilon_x[n(r)] + \varepsilon_c[n(r)] \quad \text{III.29}$$

The term of exchange, commonly called "Dirac exchange (symbolized by S because this expression was taken up by Slater [10]) is known exactly:

$$\varepsilon_x^S[n(r)] = -\frac{3}{4} \left(\frac{3n(r)}{\pi} \right)^{\frac{1}{3}} \quad \text{III.30}$$

The correlation part $\varepsilon_c[n(r)]$ cannot be expressed exactly.

III.6. Generalized-gradient approximations (GGA)

This technique integrates the density gradient to elucidate the influence of exchange and correlation effects. While non-local elements are encompassed, the LDA approach maintains its local nature by considering a density akin to that of a uniform gas. Indeed, the density gradient facilitates the incorporation of density fluctuations in proximity to each site. Consequently, we formulate the following [11]:

$$E_{xc}^{GGA}[n(r)] = \int \varepsilon_{xc}[n(r), \nabla n(r)]n(r)dr \quad \text{III.31}$$

Several functionals of this type exist among which PW91 (Perdew and Wang), PBE (Perdew-Burke-Ernzerhof), PBESol (improved version for the description of the equilibrium geometry of compact systems) and WC (Wu and Cohen).

III.7. Local density (LDA) and generalized gradient (GGA) approximations with spin polarization

The electron densities in magnetic materials depend on the spin polarization: $\rho(\uparrow)$ is distinct from $\rho(\downarrow)$, which stands for the majority and minority spin electron densities, respectively. Depending on whether gradient adjustments are used or not, the following formulas yield the exchange and correlation energies:

For a polarized spin system the equation (III.36) becomes:

$$E_{xc}^{LDA}[\rho(\uparrow), \rho(\downarrow)] = \int \rho(\vec{r}) E_{xc}[\rho(\uparrow), \rho(\downarrow)] d\vec{r} \quad \text{III.32}$$

For a polarized spin system the equation (III.39) becomes:

$$E_{xc}^{GGA}[\rho(\uparrow), \rho(\downarrow)] = \int \rho(\vec{r}) f[\rho(\uparrow)(\vec{r}), \rho(\downarrow)(\vec{r}), \nabla\rho(\uparrow)(\vec{r}), \nabla\rho(\downarrow)(\vec{r})] d\vec{r} \quad \text{III.33}$$

III.8. LDA and GGA approximations with Hubbard correction

LSDA/GGA exhibits a tendency to underestimate the gap observed in semiconductors and insulators, leading to an inability to accurately predict the characteristics of excited states, despite its many accomplishments. Particularly, the Hubbard component, signifying the effective intrasite coulombic repulsion among localized electrons, emerges as significant, especially in systems featuring d or f orbitals, where localization is pronounced. This demands the inclusion of intra-atomic correlations.

In addressing this, an alternative technique known as the DFT+U method emerges. This approach melds the DFT method (LSDA or GGA with spin polarization) with a Hubbard Hamiltonian denoted as $H_{Hubbard}$. The aim is to introduce robust, shielded intra-site coulombic interactions between d electrons [12, 13]. A straightforward variation of DFT+U, founded upon a Hamiltonian akin to the following form, was presented by Dudarev et al. [14].

$$H_{Hubbard} = \frac{U}{2} \sum_{m,m'} n_{m(\uparrow)} n_{m'(\downarrow)} + \frac{(U-j)}{2} \sum_{m \neq m'} n_{m(\uparrow)} n_{m'(\downarrow)} \quad \text{III.34}$$

Where $n_{m(\uparrow)}$ is the operator that indicates how many electrons are present in an orbital at a specific location that has the magnetic quantum number $m(\uparrow)$ and spin. U , the spherically averaged Hubbard parameter, expresses the energy expenditure involved in adding an additional electron to a certain location.

$$U = E(f^{n+1}) + E(f^{n-1}) - 2E(f^n) \quad \text{III.35}$$

J stands for the exchange energy that is screened. J is a rough estimate of the Stoner exchange parameter, while U relies on the spatial extent of the wave functions and the screening. The intrasite Coulomb repulsion is defined by the parameters U and J .

The energy contributions that the DFT functional has previously taken into consideration are included in the Mott-Hubbard Hamiltonian. The energy of the DFT+ U functional in spin polarization of Dudarev et al[14], is stated as follows after deducting the twice-counted components from the energy provided by the traditional DFT method:

$$E_{\text{DFT}+U} = E_{\text{DFT}} + \frac{(U-J)}{2} \sum_{m(\uparrow)} (n_{m(\uparrow)} - n_{m(\uparrow)}^2) \quad \text{III.36}$$

In this method, U and J act together rather than independently ($U_{\text{eff}} = U - J$). The value of U is typically determined by extra computations known as "constrained LSDA calculations"[15] or through the outcomes of experiments.

III.9. Calculation method

III.9.1. Introduction

There are three categories of approaches for solving the Schrödinger equation based on density functional theory (DFT) that have been developed by researchers in recent years and are known as first-principles methods:

- Methods based on a linear combination of atomic orbitals (LCAO)[16, 17], usable, for example, for the "d" bands of transition metals.
- The methods derived from orthogonalized plane waves (OPW)[17, 18] better adapted to the conduction bands of "s-p" character of simple metals.

- The cellular methods of the augmented plane wave (APW) type[19] and the Green's function of Korringa, Kohn and Rostoker (KKR)[20, 21] applicable to a wider variety of materials.
- The linearized methods developed by Andersen: Linearized Augmented Plane Waves (LAPW)[22] and Linearized Muffin-Tin Orbitals (LMTO), allow to gain several orders of magnitude in computation time.

III.9.2. Augmented plane wave method (APW)

In order to characterize the crystal potential, Slater[23] introduced the muffin-tin approximation in 1937 and devised a novel APW approach, proposing a radial step. This approximation results in the division of the unit cell into two different sorts of areas[24] (**Figure III.2**):

- 1- a region called interstitial region (I) far from the nuclei where electrons are more or less free.
- 2- a region inside atomic spheres "muffin tin" in the vicinity of the nucleus, the electrons behave more or less as if they were in an isolated atom.

$$\phi(\vec{r}) = \begin{cases} \frac{1}{\Omega^{1/2}} \sum_G C_G e^{i(\vec{G}+\vec{K})\vec{r}} & r \in I \\ \sum_{lm} A_{lm} U_l(r) Y_{lm}(r) & r \in S \end{cases} \quad \text{III.37}$$

Ω : Volume of the unit mesh.

Y_{lm} : Spherical harmonics.

C_G : Development coefficients.

$U_l(r)$: The regular solution of the following equation [25] :

$$\left\{ \frac{l(l+1)}{r^2} - \frac{d^2}{dr^2} + V(r) - E_l \right\} r U_l(r) = 0 \quad \text{III.38}$$

Where E_l : energy parameter.

$V(r)$: The spherical component of the potential in the sphere.

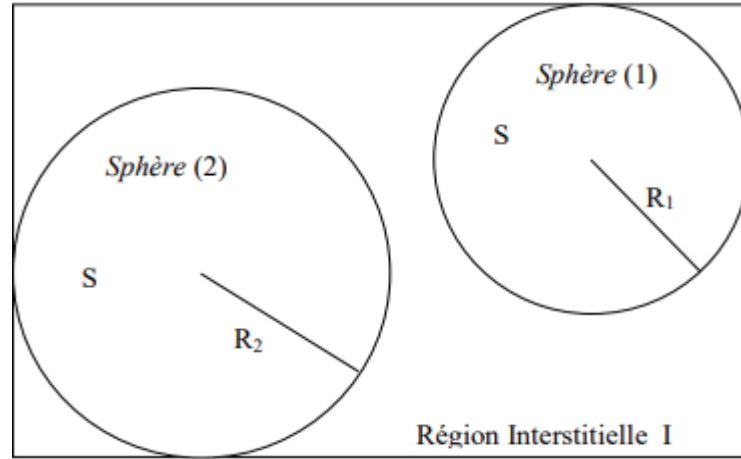


Figure III.2: Diagram of the distribution of the elementary mesh into atomic spheres and interstitial region[26].

Any Eigen state of the sphere's center is orthogonal to the radial functions that are specified by this equation. The Schrödinger equation below illustrates how the orthogonality of these functions vanishes near the sphere's edge[27]:

$$(E_1 - E_2)rU_1U_2 = U_2 \frac{d^2rU_1}{dr^2} - U_1 \frac{d^2rU_2}{dr^2} \quad \text{III.39}$$

U_1, U_2 : are the radial solutions for these energies E_1 et E_2 respectively.

In the case of a spherical potential, the solutions are the radial functions. When the symmetry of the material diminishes, the approximation becomes less and less accurate. It is particularly accurate for materials with a face-centered cubic structure.

For ensure continuity of the $\Phi(\vec{r})$ function at the surface of the MT muffin-tin sphere, the A_{lm} coefficients must be developed as a function of the existing plane wave C_G coefficients in the interstitial region:

$$A_{lm} = \frac{4\pi i^l}{\Omega^{1/2}U_l(r_l)} \sum_G C_G j_l(|K + G|r_l) Y_{lm}^*(K + G) \quad \text{III.40}$$

j_l : The Bessel functions. Where the origin is taken at the center of the sphere and r_l is its radius, Thus the A_{lm} are completely determined by the plane wave coefficients, and the energy parameters E_l are variational coefficients in the method (APW). In the interstitial zone, the wave functions behave like plane waves, whereas in the core region, they get larger and take on the characteristics of radial functions.

To overcome this problem, several modifications to the APW method have been made, including those proposed by Koelling[27] and by Andersen[22].

III.9.3 Linearized augmented plane wave method (FP-LAPW)

Although the APW method possesses asymptotic properties, its primary limitation lies in its optimal performance being restricted to uncomplicated systems featuring a limited count of eigenvalues. This constraint prompted the inception of the linearized augmented plane wave (LAPW) approach, initially proposed by Anderson[22] in 1975. The LAPW technique extends basis functions and their derivatives by linking them to a constant energy value. This alternative method effectively addresses the challenges posed by the original APW approach.

III.9.3.1 Basic functions of the FP-LAPW

The basic functions in the MT spheres of the FP-LAPW approach are linear combinations of the radial functions $U_l(r)Y_{lm}(r)$ and their energy-related derivatives $\dot{U}_l(r)Y_{lm}(r)$. The $\dot{U}_l(r)Y_{lm}(r)$ function must meet the following requirement, and the U_l functions are defined as in the APW technique (III.47).

$$\left\{ \frac{l(l+1)}{r^2} - \frac{d^2}{dr^2} + V(r) - E_l \right\} r \dot{U}_l(r) = r U_l(r) \quad \text{III.41}$$

The wave function is written as follows:

$$\phi(\vec{r}) = \begin{cases} \frac{1}{\Omega^{1/2}} \sum_G C_G e^{i(\vec{G}+\vec{K})\vec{r}} & r > r_0 \\ \sum_{lm} (A_{lm} U_l(r) + B_{lm} \dot{U}_l(r)) Y_{lm}(r) & r < r_0 \end{cases} \quad \text{III.42}$$

Where A_{lm} : are coefficients corresponding to the function U_l .

B_{lm} : are coefficients corresponding to the function \dot{U}_l

Similar to the APW approach, the LAPW functions are just plane waves in the interstitial regions. In fact, a linear combination will more accurately recreate the radial function than the APW functions if E_l departs slightly from the band energy E . In light of its derivative $\dot{U}_l(r)$ and energy E_l , the U_l function may be constructed.

$$U_l(E, r) = U_l(E_l, r) + (E - E_l) \dot{U}_l(E, r) + O((E - E_l)^2) \quad \text{III.43}$$

Et: $O(E - E_l)^2$ denotes the squared error committed.

Thus, the FP-LAPW approach guarantees the continuity of the wave function at the muffin tin sphere's surface. However, this process results in less accurate computations than the APW approach, which reproduces wave functions more well. The FP-LAPW method also introduces errors in the band energies of the order of $(E - E_l)^4$ and wave functions of the order of $(E - E_l)^2$. Despite this order of inaccuracy, the LAPW functions provide a solid foundation that makes it possible to acquire all the valence bands throughout a wide energy range with just one E_l . In situations where this is not possible, the energy window may often be divided into two portions, which is a major simplification in comparison to the APW technique.

III.9.4 Roles of the linearization energies E_l

Any core state entirely confined within the muffin-tin sphere demonstrates orthogonality with functions U and \tilde{U} . However, a caveat arises as there is a potential for misidentifying semicore states as valence states. This caveat materializes due to the fulfillment of this criterion only in the absence of core states sharing the same angular quantum number, l . While the APW technique doesn't resolve this issue, the FP-LAPW method requires careful choices to mitigate the non-orthogonal nature of certain core states. Failing to do so makes it unfeasible to accomplish the computation without adjustments.

In scenarios of this nature, resorting to the incorporation of local orbitals emerges as the optimal recourse. Nevertheless, not all software provisions this choice, thus in such instances, opting for the largest viable sphere radius becomes imperative. Lastly, it's crucial to highlight that distinct parameters need to be specified discretely. Multiple orbitals exist for energy bands, and when bands share the same angular momentum quantum number (l), selecting an energy value as close as possible to the band's energy becomes essential for precision in computing the electronic structure.

III.9.5 Construction of radial functions

Under the condition that the basic functions and their first derivatives are continuous in the limit, the basic functions in the linearly augmented plane wave approach are plane waves in the interstitial area and equal to the radial functions within the spheres. As a result, the synthesis of basic functions using this technique is equivalent to figuring out:

- 1- Radial functions $U_l(r)$ and their derivatives $\dot{U}_l(r)$.
- 2- Coefficients A_{lm} et B_{lm} that satisfy the boundary conditions.

The boundary conditions provide a simple means for the determination of the angular momentum cutoff l_{max} and for the representation of the plane wave cutoff G_{max} in the MT sphere for a radius R_α . A reasonable strategy is to choose these cutoffs, such that $R_\alpha G_{max} = l_{max}$, which is achieved in practice since the convergence of the FP-LAPW computations is ensured for $R_\alpha G_{max}$ between 7 and 9.

III.9.5.1 Non-relativistic radial functions

In the non-relativistic case, the radial functions U_l are solutions of the Schrödinger equation with a spherical potential and a fixed energy E_l .

$$\left\{ \frac{l(l+1)}{r^2} - \frac{d^2}{dr^2} + V(r) - E_l \right\} r U_l(r) = 0 \quad \text{III.44}$$

Where $V(r)$: is the spherical component of the potential in the MT sphere. The derivative with respect to the energy $\dot{U}_l(r)$ from is:

$$\left\{ \frac{l(l+1)}{r^2} - \frac{d^2}{dr^2} + V(r) - E_l \right\} r \dot{U}_l(r) = r U_l(r) \quad \text{III.45}$$

The normalization of $U_l(r)$ and of $\dot{U}_l(r)$ according to is given:

$$\int_0^{R_\alpha} r^2 U_l^2(r) dr = 1 \quad \text{III.46}$$

The suggestion of rank for which the linearization energy will be a decent approximation is made possible by the choice of the norm. In particular, Anderson claims that the inaccuracies in the linearization energy are acceptable.

$$\|\dot{U}_l\| \cdot |E_l - E| \leq 1 \quad \text{III.47}$$

Where E_l : is the energy parameter and E the energy of the bands. If such a choice is not possible, several options are available:

- 1- The energy rows are divided into windows, and each of these windows is treated separately.
- 2- We use a development in the form of local orbitals (this is effectively the quadratic method).

3- We reduce the size of the sphere. So, we reduce the norm of the derivative.

In the following, we will expose the first two methods, the third option was applied by Goedecker[28].

III.9.6 Solving the Poisson equation

The potential used in the KS equations includes the exchange and correlation term, and the coulombic term $V_c(r)$. The coulombic term is the sum of the Hartree potential $V_H(r)$ and the nuclear potential. $V_c(r)$ is determined by the fish equation from the charge density (electronic and nuclear):

$$\nabla^2 V_c(r) = 4\pi\rho(r) \quad \text{III.48}$$

This equation may be resolved in the reciprocal network. To accomplish this, Hamenn[29] and Weinert[30] suggested the "pseudo-charge" solution approach, which is largely based on the two findings listed below.

- 1- The charge density is continuous and varies slowly in the interstitial regions. On the other hand, it varies rapidly in the core region.
- 2- The coulombic potential in the interstitial region depends not only on the charges in this region, but also on the charges in the core region.

The charge density is described by a Fourier series in the interstitial region as follows:

$$\rho(\vec{r}) = \sum_G \rho(\vec{G}) e^{i\vec{G}\vec{r}} \quad \text{III.49}$$

The development of the Bessel I function allows to calculate the plane waves.

$$\int_0^R r^{l+2} J_l(\vec{G}\vec{r}) d\vec{r} = \begin{cases} R^{l+3} \frac{J_l(\vec{G}\vec{r})}{Gr} G \neq 0 \\ \frac{R^3}{3} \sigma_{l,0} G = 0 \end{cases} \quad \text{III.50}$$

So:

$$e^{i\vec{G}\vec{r}} e = 4\pi e^{i\vec{G}\vec{r}_\alpha} \sum_{lm} i^l J_l(|\vec{G}||\vec{r} - \vec{r}_\alpha|) Y_{lm}^*(\vec{G}) Y_{lm}(\vec{r} - \vec{r}_\alpha) \quad \text{III.51}$$

Where r : is the radial coordinate.

r_α : is the position of the sphere.

The coulombic potential becomes:

$$V_c(\vec{G}) = \frac{4\pi\rho(\vec{G})}{G^2} \quad \text{III.52}$$

$$V_{PW} e = \sum_{lm} V_{lm}^{PW}(r) Y_{lm}(r) = \sum_V V_V^{PW}(r) K_V(r) \quad \text{III.53}$$

Where : V_{PW} The interstitial potential.

Or:

$$V_{PW}(r) = \sum_{lm} C_{lm} Y_{lm}(r) \quad \text{III.54}$$

The potential inside the MT sphere is determined by using Green's function. $V_V(r) =$

$$V_{lm}^{PW}(r) \left[\frac{r}{R} \right] + \frac{4\pi}{2l+1} \left\{ \frac{1}{r^{l+1}} \int_0^x dr' r'^{l+2} \rho_V(r') + r^l \int_0^R dr' r'^{l-1} \rho_V(r') - \frac{r^l}{R^{2l+1}} \int_0^{R^x} dr' r'^{l+2} \rho_V(r') \right\} \quad \text{III.5}$$

Where: $\rho_V(r')$ are the radial parts of the charge density.

III.9.7 Improvement of the method (FP-LAPW)

Accurate band energies close to the linearization energies E_l are what the FP-LAPW approach seeks to achieve. In the majority of materials, picking E_l energies close to the band centers is adequate. This is not always feasible because, for many materials, selecting a single value of E_l is insufficient to compute all energy bands. Examples include elements with transition metals[31] and materials with 4f orbitals[32, 33]. The semicore state, a transitional state between the valence and core states, has this basic issue[34].

There are two ways to deal with this situation:

- The use of multiple energy windows.
- The use of local orbital development

III.9.7.1 Multiple energy windows

For solve the half-core problem, it is most frequently done by dividing the energy spectrum into windows, each of which corresponds to an E_l energy[22]. **Figure III-3** depicts this therapeutic process.

A set of E_l is selected for each window to handle the associated states in this window treatment, which creates a distinction between the valence state and the semi-core state. In

essence, this results in two separate FP LAPW computations that always have the same potential.

The FP-LAPW method is based on the fact that the U_l and \dot{U}_l functions are orthogonal to any eigenstate of the core and, in particular, to those on the surface of the sphere. However, the semicore states often satisfy this condition, unless there is the presence of "ghost" bands between the semicore and valence states.

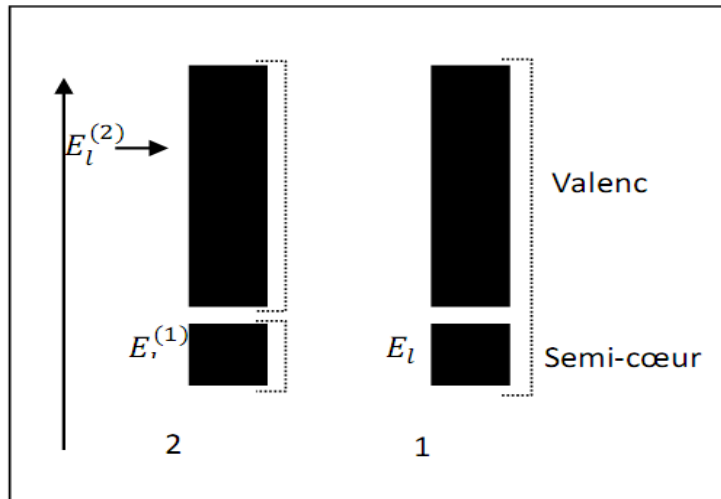


Figure III.3: Multiple energy windows

III.9.7.2 Local orbital development

The development of the LAPW method consists in a modification of the local orbitals of its basis in order to avoid the use of several windows. The main idea is to treat all bands with a single energy window by particularising the semi-core state. Several proposals were made by Tekeda [35], Pertu [36], smrka [37], Evans [38] et Singh [34], proposed a linear combination of two radial functions corresponding to two different energies and the derivative with respect to the energy of one of these functions.

$$\phi_{lm} = [A_{lm}U_l(r, E_{1,l}) + B_{lm}U_l(r, E_{1,l}) + C_{lm}U_l(r, E_{2,l})]Y_{lm}(r) \quad \text{III.56}$$

Where C_{lm} : are its coefficients having the same nature of coefficients A_{lm} and B_{lm} .

III.9.8 Treatment of spin-orbit effects

The spin-orbit term is crucial for the non-relativistic study's calculations of the band structure and electrical characteristics of materials containing heavy elements or magnetic materials.

The elements of the spin-orbit matrix inside a sphere can be calculated, a priori, as follows[39]:

$$\begin{aligned} \langle \varphi_G^\sigma | H^{SO} | \varphi_G^{\sigma'} \rangle = & \sum_{lm l'm'} \left[A_{lm}^*(G) A_{l'm'}(G') \langle U_{lm}^\sigma | H^{SO} | U_{l'm'}^{\sigma'} \rangle \right] + \\ & B_{lm}^*(G) A_{l'm'}(G') \langle \dot{U}_{lm}^\sigma | H^{SO} | U_{l'm'}^{\sigma'} \rangle + A_{lm}^*(G) B_{l'm'}(G') \langle U_{lm}^\sigma | H^{SO} | \dot{U}_{l'm'}^{\sigma'} \rangle + \\ & B_{lm}^*(G) B_{l'm'}(G') \langle \dot{U}_{lm}^\sigma | H^{SO} | \dot{U}_{l'm'}^{\sigma'} \rangle \end{aligned} \quad \text{III.57}$$

And:

$$\langle U_{lm}^\sigma | H^{SO} | \dot{U}_{l'm'}^{\sigma'} \rangle = 4\pi\sigma_{l'l'} \left(X_\sigma^+ Y_{ml}^* \sigma \cdot L Y_{l'm'} X_{\sigma'} \int dr P_l P_{l'} \left(\frac{1}{2Mc} \right)^2 \frac{1}{r} \frac{dV}{dr} \right) \quad \text{III.58}$$

Where P_l is the most important part of the radial function U_l and V the spherical part of the potential.

III.10. WIEN2k Code

The WIEN2k software constitutes a collection of Fortran-based computer programs that were developed by Peter Blaha and Karlheinz Schwarz[40] at the Institute for Materials Chemistry, Technical University of Vienna (Austria). Its inception dates back to 1990.

The Wien2k code builds upon the foundations of density functional theory and the FPLAPW approach. It encompasses a range of independent programs interconnected through a C-SHEL script to facilitate self-consistent calculations. In the initial stages, a series of input files need to be generated. Among these, the "case.struct" file assumes a central role as the master input file. It encapsulates comprehensive details about the structure, encompassing mesh parameters, atomic coordinates for individual atoms within each unit cell, lattice characteristics, and space group specification.

Once the "case.struct" file is established, a sequence of commands must be executed to generate supplementary input files (SCF files) requisite for conducting the self-consistent computation.

III.10.1 Initialization

In order to integrate in the Brillouin irreducible zone, one must establish the spatial configuration (geometry), the symmetry operations, the initial densities, the number of special points required, etc. A collection of auxiliary programs that produce and carry out all these activities.

NN : this command will calculate, from the "case.struct" file, the interatomic distances and check that the atomic spheres of the LAPW database do not overlap. Thus determine the atomic radius of the spheres.

LSTART : This program generates the atomic densities, and also determines how the different atomic orbitals are treated in the band structure calculation. As core states with or without local orbitals.

SYMMETRY : It generates the space group symmetry operations, determines the point group of individual atomic sites, generates the LM expansion for the lattice harmonics and determines the local rotation matrices

KGEN : it generates the number of k points in the Brillouin zone.

DSTART : this executable will generate the starting density for the self-consistent cycle (the SCF cycle) by superimposing the atomic densities generated in LSTART.

III.10.2. Self-Consistent Calculations

In a self-consistent cycle (SCF), the energies and electron density of the ground state are computed. Until the convergence condition (on energy, charge density, forces, etc.) is met, this cycle is initiated and repeated. Then, a different set of sub-programs is employed:

LAPW0 : it generates the Poisson potential for the calculation of the density

LAPW1 : it allows the calculation of valence bands, eigenvalues and eigenvectors.

LAPW2 : it calculates the valence densities for the eigenvectors.

LCORE it calculates the states and the core densities.

MIXER : it mixes the input and output densities (starting, valence and core). valence and core densities).

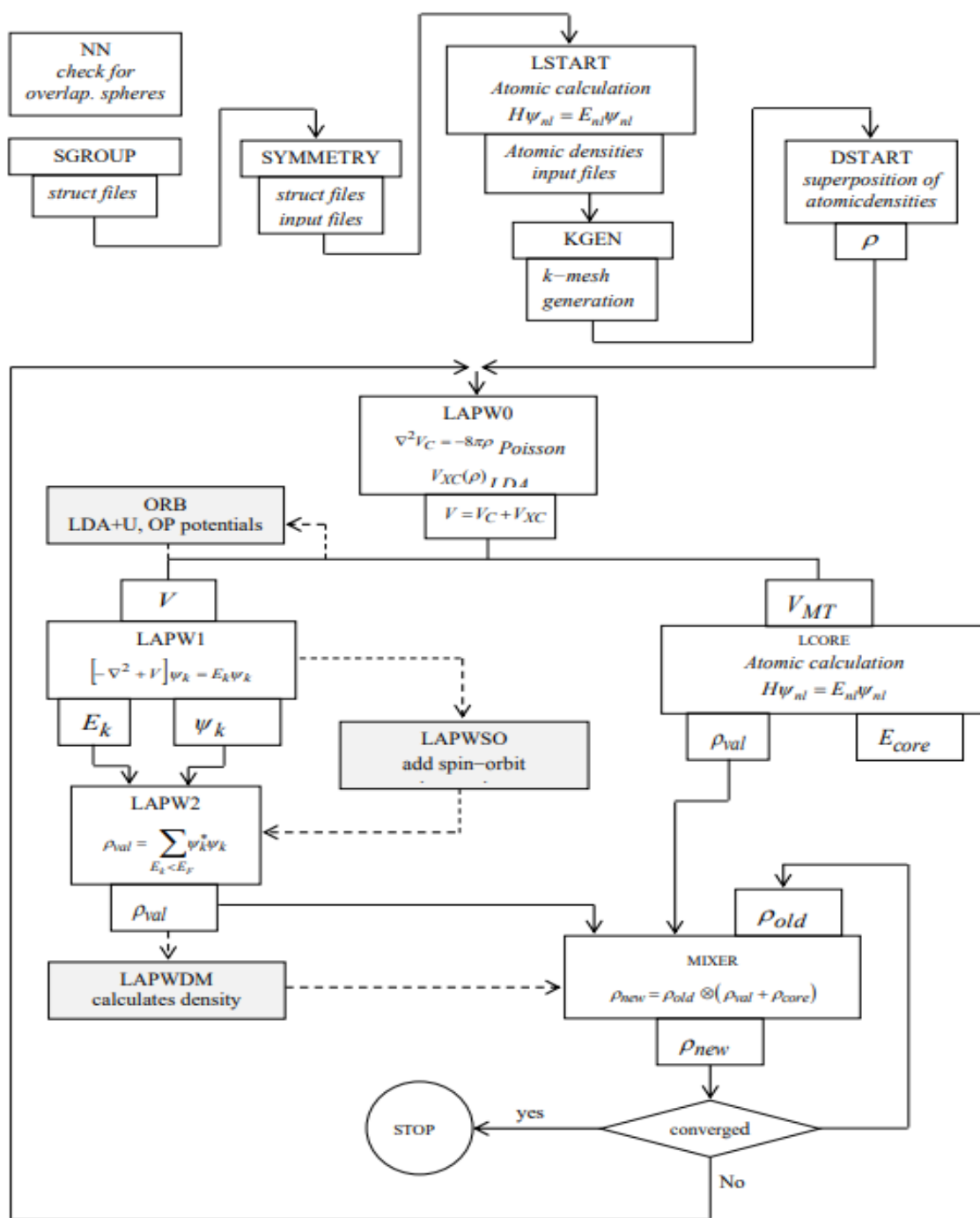


Figure III.4 Program Flowchart in WIEN2k Software

III.11. CASTEP code

The computations detailed in the manuscript (Dynamical Properties) were conducted utilizing the numerical simulation code CASTEP (Cambridge Serial Total Energy Package), originally conceived in 1988 by Payne et al[41, 42]. This code operates as an ab initio calculation tool and constitutes an integral component of the Material Studio suite of numerical simulation software, commercially offered by Accelrys.

CASTEP operates on the principles of density functional theory (DFT) to solve the Schrödinger equation. It employs an array of techniques including periodic boundary conditions, supercells, Brillouin zone integration, a plane wave basis, and pseudopotentials to ascertain the total energy of a given system. In CASTEP, electron wave functions are formulated within a plane wave basis that adheres to periodic boundary conditions and Bloch's theorem. The interaction between electrons and ions is described using ab initio pseudopotentials, with two variants available: conserved-norm pseudo-potentials and ultra-soft pseudo-potentials.

References

- [1] P. Hohenberg, W. Kohn, Inhomogeneous electron gas *phys. rev.* 136, B864, (1964).
- [2] M. Born, R. Oppenheimer, On the quantum theory of molecules, in: *Quantum Chemistry: Classic Scientific Papers*, World Scientific, 2000, pp. 1-24.
- [3] D.R. Hartree, The wave mechanics of an atom with a non-Coulomb central field. Part I. Theory and methods, in: *Mathematical Proceedings of the Cambridge Philosophical Society*, Cambridge university press, 1928, pp. 89-110.
- [4] G.H. Shortley, Note on Fock Equations for Complex Configurations, *Physical Review*, 50 (1936) 1072.
- [5] V. Fock, Näherungsmethode zur Lösung des quantenmechanischen Mehrkörperproblems, *Zeitschrift für Physik*, 61 (1930) 126-148.
- [6] T. OUAHRANI, CALCUL DES PROPRIÉTÉS STRUCTURALES, THERMIQUES ET OPTIQUES DES COMPOSÉS CHALCOPYRITES PAR LA MÉTHODE FP-(L) APW, in, *Université de Tlemcen-Abou Bekr Belkaid*, 2011.
- [7] W. Kohn, L.J. Sham, Self-consistent equations including exchange and correlation effects, *Physical review*, 140 (1965) A1133.
- [8] C. Chauvin, Les ondelettes comme fonctions de base dans le calcul de structures électroniques, in, *Institut National Polytechnique de Grenoble-INPG*, 2005.
- [9] D.M. Ceperley, B.J. Alder, Ground state of the electron gas by a stochastic method, *Physical review letters*, 45 (1980) 566.
- [10] J.C. Slater, A simplification of the Hartree-Fock method, *Physical review*, 81 (1951) 385.
- [11] J.P. Perdew, K. Burke, Comparison shopping for a gradient-corrected density functional, *International journal of quantum chemistry*, 57 (1996) 309-319.
- [12] V.I. Anisimov, J. Zaanen, O.K. Andersen, Band theory and Mott insulators: Hubbard U instead of Stoner I, *Physical Review B*, 44 (1991) 943.
- [13] A. Liechtenstein, V.I. Anisimov, J. Zaanen, Density-functional theory and strong interactions: Orbital ordering in Mott-Hubbard insulators, *Physical Review B*, 52 (1995) R5467.
- [14] S.L. Dudarev, G.A. Botton, S.Y. Savrasov, C. Humphreys, A.P. Sutton, Electron-energy-loss spectra and the structural stability of nickel oxide: An LSDA+ U study, *Physical Review B*, 57 (1998) 1505.
- [15] M. Shishkin, M. Marsman, G. Kresse, Accurate quasiparticle spectra from self-consistent GW calculations with vertex corrections, *Physical review letters*, 99 (2007) 246403.
- [16] F. Bloch, Quantum mechanics of electrons in crystal lattices, *Z. Phys*, 52 (1928) 555-600.

- [17] J.C. Slater, J.C. Phillips, Quantum theory of molecules and solids vol. 4: the self-consistent field for molecules and solids, *Physics Today*, 27 (1974) 49-50.
- [18] C. Herring, A new method for calculating wave functions in crystals, *Physical Review*, 57 (1940) 1169.
- [19] J.C. Slater, Wave functions in a periodic potential, *Physical Review*, 51 (1937) 846.
- [20] J. Koringa, On the calculation of the energy of a Bloch wave in a metal, *Physica*, 13 (1947) 392-400.
- [21] F. Ham, B. Segall, Energy bands in periodic lattices—Green's function method, *Physical Review*, 124 (1961) 1786.
- [22] O.K. Andersen, Linear methods in band theory, *Physical Review B*, 12 (1975) 3060.
- [23] O. Nielsen, R.M. Martin, First-principles calculation of stress, *Physical Review Letters*, 50 (1983) 697.
- [24] J.C. Phillips, Energy-band interpolation scheme based on a pseudopotential, *Physical Review*, 112 (1958) 685.
- [25] M.B. Kanoun, First-Principles study of Structural, Elastic and Electronic Properties of AlN and GaN Semiconductors under Pressure Effect and Magnetism in AlN: Mn and GaN: Mn systems, in, Université de Tlemcen, 2004.
- [26] S. Cottenier, Density Functional Theory and the family of (L) APW-methods: a step-by-step introduction, Instituut voor Kern-en Stralingsfysica, KU Leuven, Belgium, 4 (2002) 41.
- [27] D. Koelling, G. Arbman, Use of energy derivative of the radial solution in an augmented plane wave method: application to copper, *Journal of Physics F: Metal Physics*, 5 (1975) 2041.
- [28] S. Goedecker, Treatment of semicore states in the linearized augmented-plane-wave method and other linearized electronic-structure methods, *Physical Review B*, 47 (1993) 9881.
- [29] D. Hamann, Semiconductor charge densities with hard-core and soft-core pseudopotentials, *Physical Review Letters*, 42 (1979) 662.
- [30] M. Weinert, Solution of Poisson's equation: Beyond Ewald-type methods, *Journal of Mathematical Physics*, 22 (1981) 2433-2439.
- [31] P. Blaha, D. Singh, P. Sorantin, K. Schwarz, Electric-field-gradient calculations for systems with large extended-core-state contributions, *Physical Review B*, 46 (1992) 1321.
- [32] D. Singh, Adequacy of the local-spin-density approximation for Gd, *Physical Review B*, 44 (1991) 7451.
- [33] S. Goedecker, K. Maschke, Alternative approach to separable first-principles pseudopotentials, *Physical Review B*, 42 (1990) 8858.

- [34] D. Singh, Ground-state properties of lanthanum: Treatment of extended-core states, *Physical Review B*, 43 (1991) 6388.
- [35] T. Takeda, J. Kubler, Linear augmented plane wave method for self-consistent calculations, *Journal of Physics F: Metal Physics*, 9 (1979) 661.
- [36] J. Petrů, L. Smrčka, Quadratic augmented plane wave method for self-consistent band structure calculations, *Czechoslovak Journal of Physics B*, 35 (1985) 62-71.
- [37] L. Smrčka, Linearized augmented plane wave method utilizing the quadratic energy expansion of radial wave functions, *Czechoslovak Journal of Physics B*, 34 (1984) 694-704.
- [38] D. Shaughnessy, G. Evans, M. Darby, An improved LAPW method for the calculation of self-consistent electronic band structures, *Journal of Physics F: Metal Physics*, 17 (1987) 1671.
- [39] V. Fock, „Selfconsistent field “mit Austausch für Natrium, *Zeitschrift für Physik*, 62 (1930) 795-805.
- [40] P. Blaha, Improved and updated Unix version of the original copyrighted WIEN-code, which was published by P. Blaha, K. Schwarz, P. Sorantin, and SB Trickey, *Comput. Phys. Commun*, 59 (1990) 399.
- [41] S.J. Clark, M.D. Segall, C.J. Pickard, P.J. Hasnip, M.I. Probert, K. Refson, M.C. Payne, First principles methods using CASTEP, *Zeitschrift für kristallographie-crystalline materials*, 220 (2005) 567-570.
- [42] M.C. Payne, M.P. Teter, D.C. Allan, T. Arias, a.J. Joannopoulos, Iterative minimization techniques for ab initio total-energy calculations: molecular dynamics and conjugate gradients, *Reviews of modern physics*, 64 (1992) 1045.

Chapter IV

Results and discussions

IV.1. Introduction

This chapter presents the findings concerning the structural, elastic, electronic, and magnetic properties of CrCoSi and MnCoSi half-Heusler alloys, focusing on their half-metallicity. Additionally, the discussions extend to their derivative double half-Heusler alloy, CrMnCo₂Si₂. Through first-principles calculations utilizing density functional theory (DFT), the full-potential linearly augmented plane-wave (FP-LAPW) method is employed, with the exchange and correlation potential being described by the generalized gradient approximation (GGA).

Heusler alloys hold a significant role in the realm of spintronics physics due to their magnetic nature and diverse electronic structures influenced by spin orientation. Moreover, these alloys present an appealing potential for technological applications, owing to their Curie temperature surpassing room temperature and a structure consistent with the zinc blende arrangement found in industrially employed binary semiconductors.

IV.2. Computational method

In this investigation, the full potential linearized augmented plane waves (FP-LAPW) method[1]combined with density functional theory using the Wien2k code[2] was employed to scrutinize the structural, mechanical, and magneto-electronic characteristics of Heusler alloys CrCoSi, MnCoSi, and CrMnCo₂Si₂. The evaluation of the exchange-correlation energy functional for each material was carried out using the Perdew-Burke-Ernzerhof (PBE) generalized gradient approximation (GGA)[3, 4]. Notably, the GGA for the CrMnCo₂Si₂ derivative double half-Heusler (DHH) alloy underwent a Hubbard adjustment, with effective values (U_{eff}) of 1.59 eV for Cr, 1.92 eV for Co, and 1.69 eV for Mn[5]. These U_{eff} values have been shown to accurately depict the magnetic moment and electronic structure of the Heusler alloys.

The methodology involves dividing space into non-overlapping muffin-tin (MT) spheres separated by an interstitial zone. Specific MT values are assigned for different atoms: Cr (1.46 Bohr), Mn (1.71 Bohr), Co (1.83 Bohr), Si (1.5 Bohr), and 1.71 Bohr (Bohr) for different atoms. The study also specifies criteria such as RMT cutoff, K_{max} , l_{max} , G_{max} , and N_k -points are 8.0, 10, 12, and 3000, respectively, where R_{MT} represent the smallest muffin-tin sphere radius, K_{max} is the maximum modulus for the reciprocal vectors, l_{max} is the maximum angular quantum number for the expansion of wave functions inside the spheres, G_{max} is the plane-wave cutoff (magnitude of largest vector in charge density Fourier

expansion), and $N_{k\text{-points}}$ is the number of k-points in the whole Brillouin zone. The convergence criterion of 10^{-6} Ry and 10^{-5} e for the energy and charge, respectively, are used.

IV.3. Structural properties

IV.3.1 Crystalline structure of Heusler alloys and preferred sites

The pivotal phase of ab-initio calculations is the determination of a system's structural characteristics in its ground state. This understanding lays the foundation for grasping other crucial physical attributes. In this regard, the fusion of two half-Heusler compounds, CrCoSi and MnCoSi, culminates in the crystalline structure denoted as CrMnCo₂Si₂. This crystal structure is classified under space group N^o115, resulting from the amalgamation of CrCoSi and MnCoSi.

The distinctive hallmark of the half-Heusler structure is the intertwining of three face-centered cubic sub-lattices[6]. Within this framework, three non-equivalent atomic arrangements emerge, specifically type I, type II, and type III. These possibilities are elucidated in Table IV.1.

Table IV.1: Different possibilities for occupying non-equivalent sites in the Half-Heusler C1b structure, for the compounds studied CrCoSi, MnCoSi.

Structure	CrCoSi			MnCoSi		
	Cr	Co	Si	Mn	Co	Si
Type I	$(\frac{1}{4}, \frac{1}{4}, \frac{1}{4})$	$(\frac{1}{2}, \frac{1}{2}, \frac{1}{2})$	(0,0,0)	$(\frac{1}{2}, \frac{1}{2}, \frac{1}{2})$	$(\frac{1}{4}, \frac{1}{4}, \frac{1}{4})$	(0,0,0)
Type II	(0,0,0)	$(\frac{1}{2}, \frac{1}{2}, \frac{1}{2})$	$(\frac{1}{4}, \frac{1}{4}, \frac{1}{4})$	$(\frac{1}{4}, \frac{1}{4}, \frac{1}{4})$	$(\frac{1}{2}, \frac{1}{2}, \frac{1}{2})$	(0,0,0)
Type III	(0,0,0)	$(\frac{1}{4}, \frac{1}{4}, \frac{1}{4})$	$(\frac{1}{2}, \frac{1}{2}, \frac{1}{2})$	(0,0,0)	$(\frac{1}{4}, \frac{1}{4}, \frac{1}{4})$	$(\frac{1}{2}, \frac{1}{2}, \frac{1}{2})$

IV.3.2 Structural optimization and magnetic order

Establishing the structural properties serves as a foundational initial stride in any computational endeavor, serving as a basis for deducing other material attributes under investigation. This is particularly pertinent in our case as we aim to discern both the fundamental state structure of the alloy and its optimal magnetic configuration.

In the preliminary phase, the energy-volume relationship is calculated for the subsequent compounds, namely the half-Heusler (HH) compounds, in their ferromagnetic (FM), non-magnetic (NM), and antiferromagnetic (AFM) phases. These calculations are

depicted graphically in Figure IV.1. The presented graphs vividly illustrate that our HH compounds manifest greater stability when adopting the FM phase with a type I structure, characterized by the specific atomic arrangement: Cr/Mn(0,0,0), Co(1/4,1/4,1/4), and Si(1/2, 1/2,1/2).

The double half-Heusler (DHH) configuration is achieved by substituting two Cr atoms within the cubic conventional unit cell of the CrCoSi half-Heusler compound, which possesses a lattice parameter denoted as a_{HH} . This substitution involves the introduction of Mn atoms, leading to a resulting tetragonal structure (with lattice parameters ($a_{DHH} = \frac{a_{HH}}{\sqrt{2}}$, $c_{DHH} = a_{HH}$)). The optimization of this newly obtained DHH structure is executed across its ferromagnetic (FM), non-magnetic (NM), and antiferromagnetic (AFM) phases, visually represented in Figure IV.2. It is discernible from this depiction that the FM phase stands as the most energetically stable magnetic configuration.

Furthermore, in the quest for the ground state properties, the calculated total energies in relation to volume are subjected to fitting using the Birch-Murnaghan equation[7], as outlined below:

$$E(V) = E_0 + \frac{9V_0B_0}{16} \left\{ \left[\left(\frac{V_0}{V} \right)^{2/3} - 1 \right]^3 \dot{B}_0 + \left[\left(\frac{V_0}{V} \right)^{2/3} - 1 \right]^2 \left[6 - 4 \left(\frac{V_0}{V} \right)^{2/3} \right] \right\} \quad \text{IV.1}$$

Where $E(V)$ represents the energy of the ground state with cell volume V and V_0 the volume of the unit cell at zero pressure, B_0 and \dot{B}_0 are the modulus of compressibility and its derivative, respectively.

The equilibrium network constant is given by the minimum of the curve (V), and the modulus of compressibility B_0 and its derivative are determined by:

$$B_0 = V \left(\frac{d^2E}{dV^2} \right)_V = V_0 \quad \text{IV.2}$$

$$\dot{B}_0 = \left(\frac{\partial B}{\partial p} \right)_p = 0 \quad \text{IV.3}$$

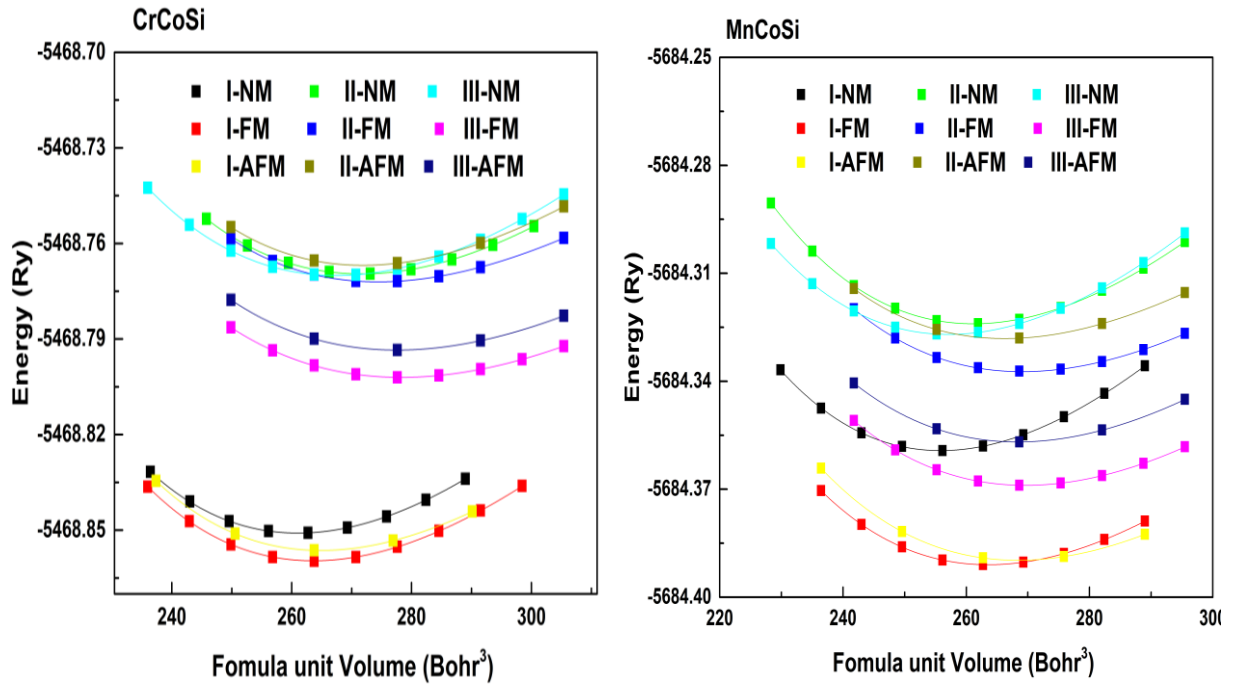


Figure IV.1. Total energy per formula unit of ferromagnetic (FM), non-magnetic (NM) and antiferromagnetic (AFM) phases as functions of the volume for CrCoSi and MnCoSi HH alloys.

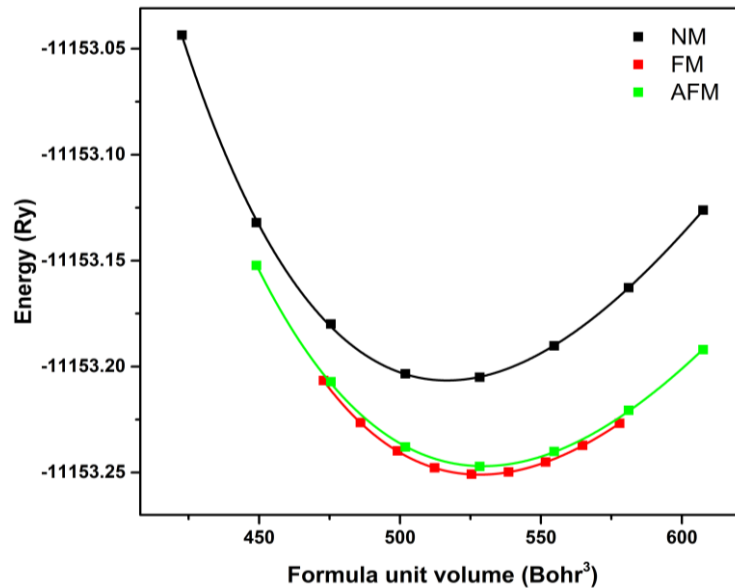


Figure IV.2. Total energy per formula unit as functions of the volume for the ferromagnetic (FM), non-magnetic (NM), and antiferromagnetic (AFM) phases of CrMnCo₂Si₂ DHH alloy.

In **Table IV.2**, we have grouped together the results of the values obtained for the structural properties: the equilibrium lattice parameter $a_0(\text{\AA})$, the compressibility modulus $B(\text{GPa})$ and the derivative of the compressibility modulus B' . CrCoSi, MnCoSi, and CrMnCo₂Si₂ compounds, for FM phase. The bulk modulus is a measure of how resistant these compounds are to compression and is determined by the equation: $B = V \frac{\partial^2 E}{\partial V^2}$. The obtained results, as

can be seen in **Table IV.2**, show that the resistance to compression (Bulk modulus) decreases with the increase of X atomic number ($B(\text{CrCoSi}) > B(\text{CrMnCo}_2\text{Si}_2) > B(\text{MnCoSi})$).

Table IV.2 Calculated lattice parameters (in Å) for the structural ground state of the CrCoSi, MnCoSi HH alloys and parent structure of CrMnCo₂Si₂ DHH, bulk moduli (in GPa), their derivative pressures, and magnetic ground phase (FM) for CrCoSi, MnCoSi and CrMnCo₂Si₂ compounds.

X		a_{HH}	B	B'
CrCoSi	GGA	5.3864	190.87	4.86
		5.4100[8]		
		5.3900[9]		
MnCoSi	GGA	5.3857	174.72	5.02
		5.4100[9]		
CrMnCo ₂ Si ₂	GGA	5.3899	181.00	4.72

IV-3.2 Formation Energy (or enthalpy of formation)

The enthalpy of formation of a crystal is defined as the difference between the crystal's energy and the sum of the energies of the elements that comprise the crystal in their standard states (a body is said to be in the standard state when it is pure, unmixed, and in its most stable physical state).

In order to verify the validity of synthesizing these alloys, we calculated the energy of formation using the following expressions:

$$E_{form}(XCoSi) = E_{XCoSi}^{tot} - (E_X^{bulk} - E_{Ca}^{bulk} - E_{Si}) \quad \text{IV.4}$$

$$E_{form}(CrMnCo_2Si_2) = E_{CrMnCo_2Si_2}^{tot} - (E_{Cr}^{bulk} + E_{Mn}^{bulk} + 2E_{Ca}^{bulk} + 2E_{Si}) \quad \text{IV.5}$$

where E_{XCoSi}^{tot} and $E_{CrMnCo_2Si_2}^{tot}$ are the total energies per unit cell for XCoSi (X=Cr, and Mn), CrMnCo₂Si₂, respectively, at the equilibrium state and E_{Cr}^{bulk} , E_{Mn}^{bulk} , E_{Co}^{bulk} and E_{Si}^{bulk} match to the total energy for Cr, Mn, Co, and Si, per atom, respectively, at ground state. The resulted negative values of the formation energy point out that our studied compounds are thermodynamically stable and it is possible to synthesize them experimentally.

The values of the energies of formation for the compounds studied are shown in **Table IV.3**. We can see that the negative values of the energies of formation for all the compounds studied indicate the existence and stability of these alloys and that it is possible to synthesize them experimentally.

Table IV.3. Calculated formation (E_{form}) energies (in eV/Atom) of the structural and magnetic ground phase (FM) for CrCoSi, MnCoSi and CrMnCo₂Si₂ compounds.

X		E_{tot}	E_{form}
CrCoSi	GGA	-5468.85962	-0.45
MnCoSi	GGA	-5684.39097	-0.44
CrMnCo ₂ Si ₂	GGA	-11153.250925	-0.45

IV-4. Dynamical proprieties

An additional crucial aspect within the investigation of crystalline materials is the realm of "phonons," which divulge the material's response to atomic vibrations. Phonon dispersion spectra and phonon density of states (DOS) provide both direct and indirect insights into an array of material-related physical properties[10]. Phonon dispersion spectra (PDS) are particularly informative, offering insights into structure stability, phase transitions, and the interplay between vibrations and the thermal and charge transport characteristics of a material[11].

In order to assess the dynamical stability of the CrMnCo₂Si₂ compound, we embarked on calculating its phonon dispersion diagram. This was achieved through the employment of the linear response method within the framework of density functional perturbation theory (DFPT), a technique implemented in the CASTEP code[12]. The resultant phonon dispersion, traced along lines of high symmetry within the Brillouin zone for CrMnCo₂Si₂, is depicted in Figure IV.3. It is established that a material's dynamical stability can be inferred from the presence or absence of soft modes (imaginary modes; negative frequencies) in its phonon dispersion curve[13]. In the case of the phonon dispersion diagram for CrMnCo₂Si₂, as portrayed in Figure IV.3, the absence of negative frequencies serves to underscore the compound's dynamical stability.

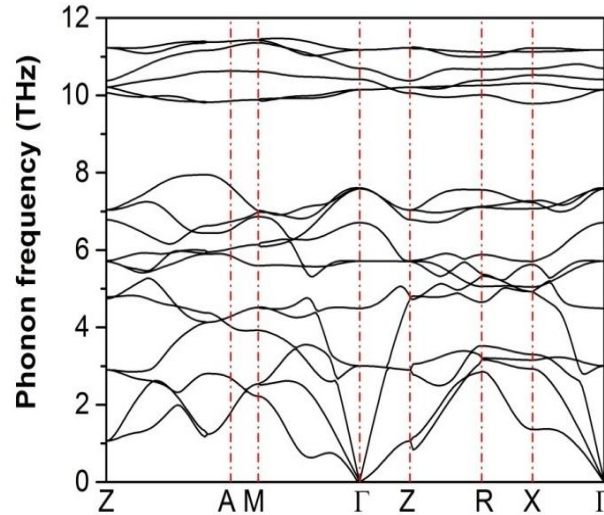


Figure IV.3. Phonon dispersion diagram along lines of high symmetry in the Brillouin zone for the $\text{CrMnCo}_2\text{Si}_2$ compound.

IV.5. Mechanical properties

Elastic properties hold significant significance in furnishing valuable insights into the interatomic stresses among neighboring planes. The anisotropic character of these stresses, coupled with structural stability, is often characterized by the elastic constants denoted as C_{ij} . These constants embody macroscopic parameters that establish a link between stress and strain within homogeneous solids.

The framework of Hook's law establishes the correlation between stress and strain through the utilization of elastic constants. Within a cubic structure, there exist solely three distinct elastic moduli: C_{11} , C_{12} , and C_{44} . Their determination involves solving three equations derived from the application of three distinct deformation scenarios. The foremost equation corresponds to the expression governing the compressibility modulus within the cubic system.

$$B = \frac{C_{11} + 2C_{12}}{3} \quad \text{IV.6}$$

The second equation is formed by the application of a volume conserved orthorhombic deformation tensor which is given by the following expression:

$$\bar{\epsilon} = \begin{bmatrix} \delta & 0 & 0 \\ 0 & -\delta & 0 \\ 0 & 0 & \frac{1}{1-\delta^2} \end{bmatrix} \quad \text{IV.7}$$

Where the total energy expression has the following form:

$$E(\delta) = E(-\delta) = E(0) + (C_{11} - C_{12})V_0\delta^2 + O(\delta^4) \quad \text{IV.8}$$

V_0 is the volume of the elementary mesh and $E(0)$ is the energy of the unconstrained system in this volume. Finally, to determine the C_{44} , we apply a volume-conserved monoclinic deformation of the following form:

$$\bar{\epsilon} = \begin{bmatrix} \frac{\delta}{2} & 0 & 0 \\ 0 & -\frac{\delta}{2} & 0 \\ 0 & 0 & \frac{\delta^2}{4-\delta^2} \end{bmatrix} \quad \text{IV.9}$$

The total energy of the system has become:

$$E(\delta) = E(-\delta) = E(0) + \frac{1}{2}C_{44}V_0\delta^2 + O(\delta^4) \quad \text{IV.10}$$

Other mechanical quantities as Bulk $B_{C/T}$ (C for cubic structure and T for tetragonal structure), shear G, Young's E moduli, anisotropic factor, as well as Poisson's ratio can be obtained from the evaluated elastic constants by using the following formula:

$$B_C = \frac{C_{11}+2C_{12}}{3}, \quad B_T = \frac{1}{9}(2C_{11} + 2C_{12} + 4C_{13} + C_{33}) \quad \text{IV.11}$$

$$G_C = \frac{1}{5}(3C_{44} + C_{11} - C_{12}), \quad \text{IV.12}$$

$$G_T = \frac{1}{2} \left[\frac{2C_{11} + C_{33} - C_{12} - 2C_{13}}{15 + (2C_{44} + C_{66})/5} + \frac{15}{4(S_{11} + S_{22} + S_{33}) + 3(S_{44} + S_{55} + S_{66}) - 4(S_{12} + S_{13} + S_{23})} \right]$$

$$E_{C/T} = \frac{9BG}{3B+G}, \quad \text{IV.13}$$

$$\nu_{C/T} = \frac{1}{2} \left(1 - \frac{E}{3B} \right), \quad \text{IV.14}$$

$$A_C = \frac{2C_{44}}{C_{11}-C_{12}}, A_{C/T} = 5 \frac{G_V}{G_R} + \frac{B_V}{B_R} - 6 \quad \text{IV.15}$$

Driven by their interest in elucidating the mechanical attributes and structural robustness of solid materials, the researchers embarked on determining the elastic constants C_{11} , C_{12} , and C_{44} . This was achieved by manipulating the total energy of the deformed crystal. The acquired values are conveniently presented in Table IV.4. Additionally, a spectrum of other elasticity parameters including the compressibility modulus B , shear modulus G , Young's modulus E , Poisson's ratio ν , anisotropy parameter A , and the B/G ratio were evaluated.

The outcomes, as detailed in Table IV.4., exhibit positive values and align with Born's stability criteria for cubic structures[14]: $C_{11} > 0$, $C_{11} - C_{12} > 0$, $C_{11} + 2C_{12} > 0$, and $C_{44} > 0$. Similarly, for the tetragonal (I) structure [26]: $C_{11} > 0$, $C_{33} > 0$, $C_{44} > 0$, $C_{66} > 0$, $C_{11} - C_{12} >$

0, $C_{11} + C_{33} - 2C_{13} > 0$, and $2C_{11} + C_{33} + 2C_{12} + 4C_{13} > 0$. Consequently, the mechanical stability of CrCoSi, MnCoSi, and CrMnCo₂Si₂ is firmly established.

Table IV.4 Elastic constants C_{11} , C_{12} , C_{13} , C_{33} , C_{44} , C_{66} (in GPa), bulk B , Young E (GPa), Shear G moduli (in GPa), B/G , Anisotropic parameter A , and Poisson's coefficients ν of CrCoSi, MnCoSi and CrMnCo₂Si₂ Heusler alloys.

X	C_{11}	C_{12}	C_{13}	C_{33}	C_{44}	C_{66}	B	E	G	B/G	A	ν
CrCoSi	285.5 274.6[8]	145.8 115.2[8]	/	/	132.3 94.9[8]	/	192.4	125.8	49.3	1.9	0.62	0.28
MnCoSi	253.60	137.97	/	/	127.5	/	176.5	131.9	52.1	1.7	0.75	0.26
CrMnCo₂Si₂	330.96	74.15	137.7	268.2	127.5	65.2	181.0	248.0	97.5	1.9	0.57	0.27

Where B_V , G_V , B_R and G_R represent the estimated bulk and shear moduli using Voigt and Reuss methods, respectively. The calculated elastic constants, along with mechanical parameters for all the considered materials, are presented in Table IV.4. Notably, the bulk modulus values derived from elastic constants for the three compounds closely align with those obtained from total energy optimization. Based on the calculated data, it is evident that CrCoSi exhibits enhanced resistance to deformation compared to the other compounds. On a different note, the shear modulus demonstrates a robust capacity to counter reversible deformation caused by shear strain in the CrMnCo₂Si₂ derivative double half-Heusler (DHH) alloy. Furthermore, its Young's modulus value indicates superior hardness when juxtaposed with its parent compounds, CrCoSi and MnCoSi.

To gauge the ductility and brittleness of our studied compound, the B/G ratio, also known as Pugh's ratio, is commonly employed. According to Pugh's index[15], if $B/G < 1.75$ ($B/G > 1.75$), the material is classified as brittle (ductile), respectively. The calculated B/G values for CrCoSi, MnCoSi, and CrMnCo₂Si₂ are 1.9, 1.7, and 1.9, respectively. This indicates that MnCoSi is categorized as brittle, while both CrCoSi and CrMnCo₂Si₂ compounds exhibit ductile behavior.

For assessing the degree of anisotropy, the anisotropic parameter A is employed. Isotropic materials have $A = 1$, whereas anisotropic materials have $A \neq 1$ [16]. In the case of the compounds CrCoSi, MnCoSi, and CrMnCo₂Si₂, A deviates from unity, signaling their anisotropic behavior. Poisson's ratio ν is a commonly utilized metric to comprehend the nature of bonding forces within a compound [17]. The calculated values of Poisson's ratio are 0.28, 0.26, and 0.27 for CrCoSi, MnCoSi, and CrMnCo₂Si₂, respectively, which are in the vicinity of 0.25. This value suggests a higher ionic nature of inter-atomic bonding.

The resulting computed elastic parameters, as presented in Table IV.4, are in commendable concurrence with those reported by Hussain et al[8]. for the investigated half-Heusler (HH) alloys.

IV.6. Electronic and magnetic properties

Within this section, we shall delve into the electronic and magnetic structural properties of the materials under scrutiny. Specifically, we will unveil the band structure, along with the total and partial densities of states, at their fundamental structural states for both majority and minority spins. These evaluations will be conducted along the high symmetry directions within the first Brillouin zone. Notably, these electronic properties will be elucidated for both spin channels and will be based on the utilization of the generalized gradient approximation (GGA-PBE).

Our focus in this exploration of electronic structures is twofold: first, to unravel insights into the nature and origins of the half-metallic behavior; and second, to discern the impact of potent correlations on the gap energy within the half-Heusler compounds CrCoSi, MnCoSi, and the derivative double half-Heusler CrMnCo₂Si₂. This comprehensive analysis is aimed at deepening our understanding of the intricate interplay between electronic structure, magnetic properties, and strong correlations present within these compounds.

IV-6.1. Electronic properties

IV-6.1.1. Electronic band structure

The computational exploration of electronic structures holds paramount significance in the anticipation of half-metallic ferromagnetism and the identification of magnetic traits within both half-Heusler and derivative double half-Heusler compounds. Through electronic structure simulations, materials can be tailored to cater to specific spintronic applications.

Electronic structure investigations provide us with the means to classify compounds as insulating, conducting, semiconducting, or semimetallic, contingent on the band width and the position of the Fermi level[18]. Illustratively, Figure IV.4, delineates energy levels and bands in a vertical arrangement, progressing with increasing energies. Among these, the valence bands and conduction bands constitute the highest energy bands, separated by a region of forbidden energy known as the energy gap. The energy gap is defined as the discrepancy between the highest point of the valence band and the lowest point of the conduction band.

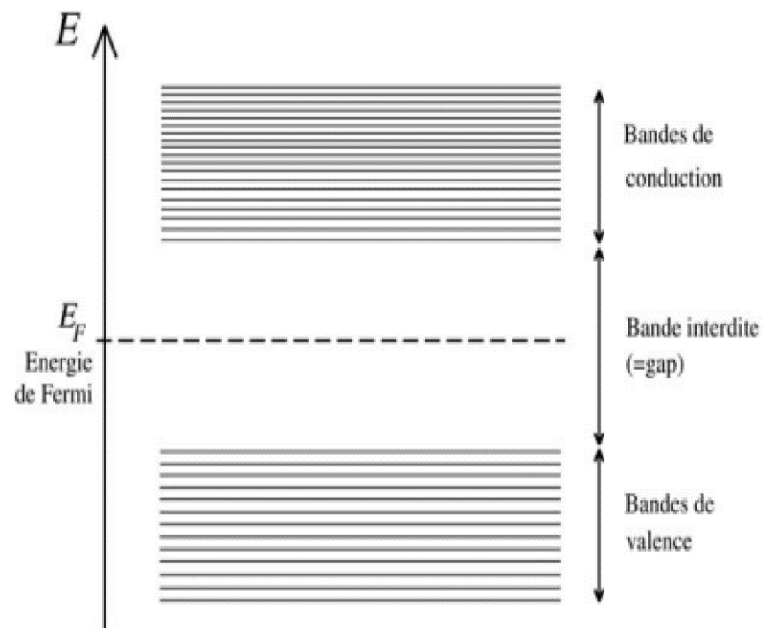


Figure IV.4: Valence bands, conduction bands, band gap and the Fermi level.

To do this, we study the band structures of the compounds CrCoSi, MnCoSi, and CrMnCo₂Si₂. The electronic band structures are calculated along the directions of high symmetry in the first Brillouin zone, for the majority and minority bands of the three compounds, calculated at their equilibrium lattice parameters in their structural and magnetic ground states, shown in Figure IV.5.

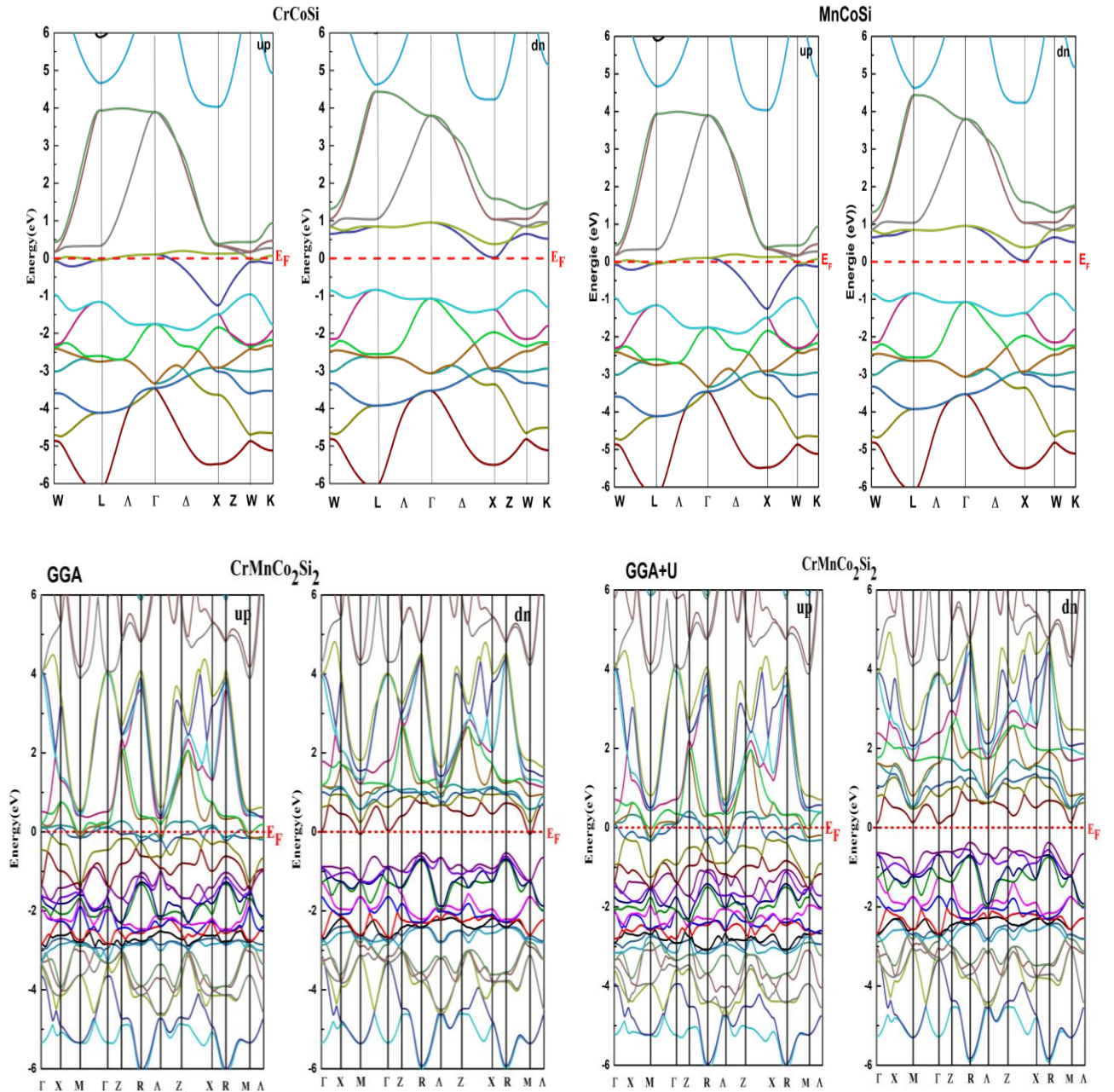


Figure IV.5: Spin-polarized band structures for CrCoSi, MnCoSi, and CrMnCo₂Si₂ Heusler alloys.

In Figure IV.5, the spin-polarized band structures (both spin-up and spin-down) of the three compounds are depicted. The Fermi level (E_F) is demarcated by a horizontal red line. Evidently, the overall band profiles exhibit striking similarity across the studied half-Heusler (HH) compounds, with minor variations in the finer details. Notably, band crossings with the Fermi level are apparent in the majority-spin channel. Conversely, in the minority-spin bands, the Fermi level resides within the energy band gap. This distinct electronic behavior categorizes the considered HHs as exhibiting half-metallic properties, denoted by energy gaps (half-metallic gaps) of approximately 0.85 eV and 0.02 eV for both compounds.

This coherence in their electronic characteristics can be attributed to the closely aligned atomic numbers of Cr ($Z=24$) and Mn ($Z=25$) atoms within their structures.

Furthermore, as Table IV.5 illustrates, these findings diverge from those reported by Feng et al.[9] and Hussain et al.[8], primarily due to the utilization of distinct methods. The dissimilarity in methodology is rooted in the description of ion-electron interaction through ultrasoft pseudo potentials[19, 20]. Additionally, our exploration of the derivative double half-Heusler (DHH) compound $\text{CrMnCo}_2\text{Si}_2$ uncovers narrower energy gaps (HMGap) of 0.53(0.002) and 0.382(0.106) eV (via GGA and GGA+U approximations, respectively). This underlines the substantial impact of the chosen computational approach on the calculated energy gaps. In summary, the amassed data robustly substantiate the half-metallic nature of CrCoSi , MnCoSi , and $\text{CrMnCo}_2\text{Si}_2$ Heusler alloys, a classification concisely summarized in Table IV.5.

Table IV.5: Gap, and Half-metallic gap (in eV) of CrCoSi , MnCoSi , and $\text{CrMnCo}_2\text{Si}_2$ Heusler alloys.

<i>X</i>		<i>Gap</i>	<i>HM Gap</i>
CrCoSi	GGA	0.851	0.020
		1.160[8]	0.650[8]
		0.670[9]	0.660[9]
MnCoSi	GGA	0.852	0.021
		0.640[9]	0.190[9]
CrMnCo ₂ Si ₂	GGA	0.53	0.002
	GGA+U	0.382	0.106

IV-6.1.2. Densities of states

In determining the energy distribution of electrons within the valence and conduction bands, a fundamental parameter called the density of electronic states (DOS) comes into play. This parameter is of utmost importance. For instance, when investigating a material's electrical conduction characteristics, the total density of states (TDOS) is often employed. Moreover, a distinct sphere is defined around each atom, within which the electron density is projected onto spherically shaped harmonics (s, p, d, or f orbitals). This process yields partial densities of states (PDOS), which can be instrumental in unraveling the nature of chemical bonds between atoms within a crystal or molecule. It's worth noting that projections of the total density of states are dependent on the radii of the spheres onto which the partial densities of states are projected, and therefore they offer qualitative insights[21].

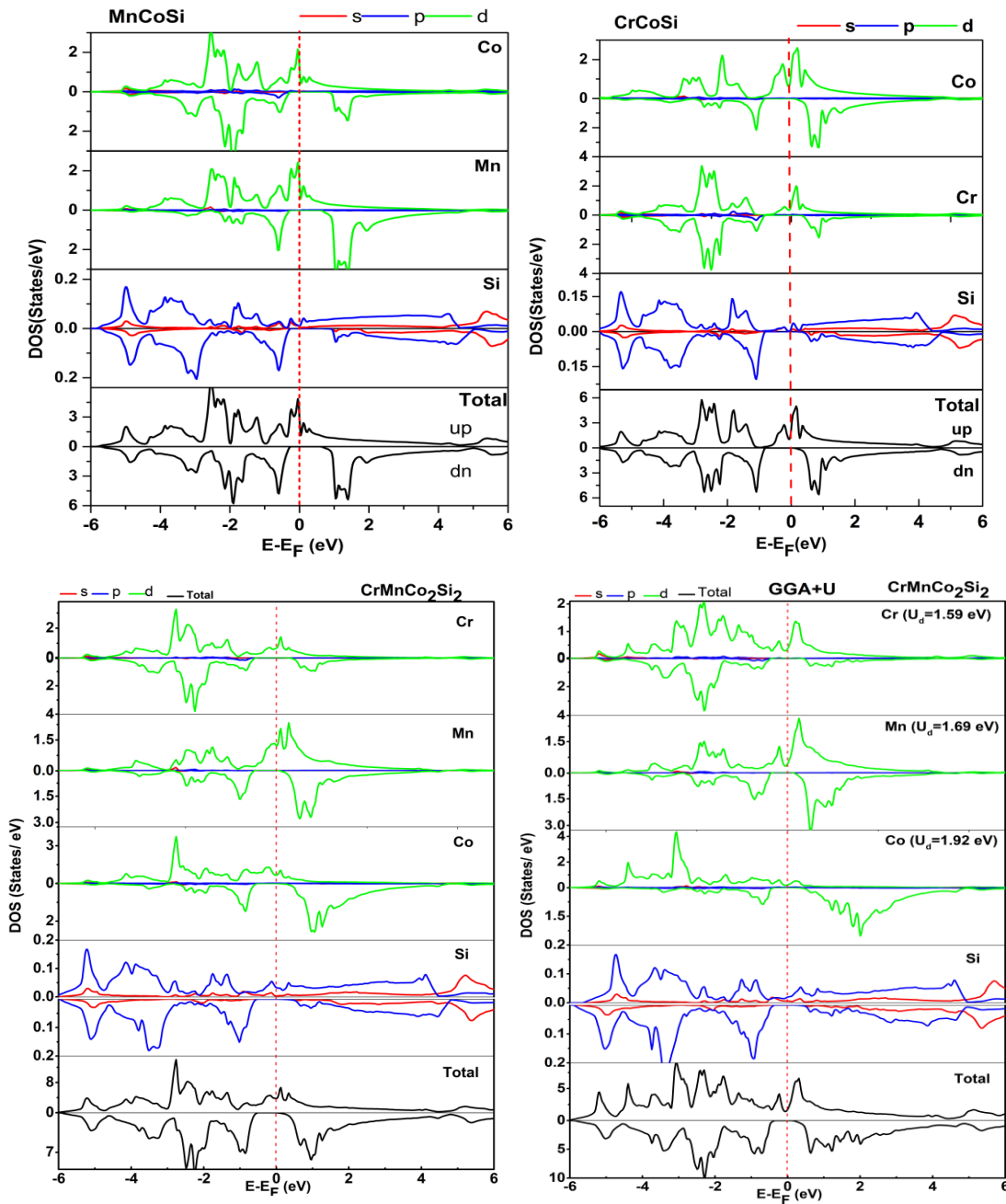


Figure IV.6: Spin-polarized density of states (DOS) for CrCoSi, MnCoSi, and CrMnCo₂Si₂ Heusler alloys.

For a comprehensive understanding of electronic properties, both total (TDOS) and partial (PDOS) densities of states have been visually represented in Figure IV.6. This depiction unveils the electronic state densities of the half-Heusler compounds CrCoSi, MnCoSi, and CrMnCo₂Si₂. These calculations were performed using the generalized gradient approximation (GGA). The vertical red line is indicative of the Fermi level (E_F) within the system.

For the Half-Heusler compounds CrCoSi, MnCoSi, and CrMnCo₂Si₂, we notice the following: The magnetic moment is essentially originated from Cr, and Mn atoms in which

the Cr-d, Mn-d states have large exchange divisions between the states of the spin up and - down channels around the Fermi level, for CrCoSi, and MnCoSi, respectively. Furthermore, little contributions to the total magnetic moment are from Co and Si atoms.

IV-7. Magnetic properties

This section is dedicated to exploring the magnetic attributes of the elements under scrutiny. The total and partial magnetic moments of the compounds have been ascertained through the utilization of the GGA approximation, while accounting for the influence of spin-orbit coupling correction.

The work of Galanakis et al. illuminated a coherent pattern within the total spin magnetic moment of half-metallic half-Heusler compounds, succinctly referred to as the Slater-Pauling rule[22]. This empirical relationship connects the total magnetic moment M_{tot} , per unit formula, with the overall count of valence electrons within the elemental lattice. The relationship is articulated as follows:

$$M_{tot} = (N_V - 18)\mu_B \quad \text{IV.16}$$

This is because the total number of valence electrons, N_V , is given by the sum of the number of spin up and spin down electrons, while the total magnetic moment, M_{tot} , is given by their difference, i.e. M_{tot} is the number of uncompensated spins. It follows that:

$$M_{tot} = (N_{maj} - N_{min})\mu_B = (N_V - 2N_{maj})\mu_B \quad \text{IV.17}$$

Where N_{maj} and N_{min} are the number of occupied states of majority and minority spins, respectively.

Given that the energy gap at the Fermi level (E_F) resides within the majority-spin bands, the total magnetic moment (M_{tot}) is furnished by subtracting twice the number of occupied majority states from the total count of valence electrons (N_V). Consequently, within the context of the three investigated half-metallic half-Heusler compounds, these bands are fully populated, accommodating a total of nine bands. Each of these bands has the potential to host nine spin-up electrons per unit cell. This relationship is expressed by Equation IV.17.

Table IV.6: Atomic (M_{Cr} , M_{Co} , M_{Mn} , M_{Si}), interstitial ($M_{Intersti}$) and total magnetic (M_{tot}) moments (in μ_B) for CrCoSi, MnCoSi, and CrMnCo₂Si₂ Heusler alloys.

X	Method	M_{Cr}	M_{Mn}	M_{Co}	M_{Si}	$M_{Intersti}$	M_{tot}
CrCoSi	GGA	1.166		-0.178	-0.031	0.043	1.000
		1.550[8]		-0.410[8]	-0.09[8]		1.000[8]
		1.560[9]		-0.42[9]			1.000[9]
MnCoSi	GGA		2.114	0.027	-0.061	0.080	1.999
			2.120[9]	-0.040[9]			2.000[9]
CrMnCo ₂ Si ₂	GGA	0.612	2.560	-0.042	-0.034	-0.018	3.000
	GGA+U	0.438	3.352	-0.329	-0.058	-0.047	3.000

For the half-Heusler compounds CrCoSi, MnCoSi, and the derivative CrMnCo₂Si₂, the following observations can be made:

1. Co atom has a negative magnetic moment for both HH alloys, demonstrating an antiferromagnetic interaction between Co and Cr/Mn atoms.
2. There is no contribution of Si atom for all studied Heusler compounds.
3. Total Magnetic Moments:
 - For CrCoSi: The total magnetic moment amounts to 1 μ_B (Bohr magneton).
 - For MnCoSi: The total magnetic moment is 2 μ_B .
 - For CrMnCo₂Si₂: In this derivative double half-Heusler alloy, the results from both approximations (GGA and GGA+U) highlight that the predominant contribution to its total magnetic moment arises from the Cr and Mn atoms. This is substantiated by a notable splitting of their d-orbitals around the Fermi level, resulting in a remarkable 100% spin-polarization. The spin-magnetization, quantified as 3 μ_B , solidifies the classification of CrMnCo₂Si₂ as a half-metallic material.

These magnetic insights underscore the intricate interplay of various atoms within the compounds, influencing their magnetic behaviors and classifications.

References

- [1] P. Blaha, K. Schwarz, P. Sorantin, S. Trickey, Full-potential, linearized augmented plane wave programs for crystalline systems, *Computer physics communications*, 59 (1990) 399-415.
- [2] P. Blaha, K. Schwarz, G.K. Madsen, D. Kvasnicka, J. Luitz, wien2k, An augmented plane wave+ local orbitals program for calculating crystal properties, 60 (2001).
- [3] J.P. Perdew, K. Burke, Y. Wang, Generalized gradient approximation for the exchange-correlation hole of a many-electron system, *Physical review B*, 54 (1996) 16533.
- [4] J.P. Perdew, K. Burke, M. Ernzerhof, Generalized gradient approximation made simple, *Physical review letters*, 77 (1996) 3865.
- [5] H.C. Kandpal, G.H. Fecher, C. Felser, Calculated electronic and magnetic properties of the half-metallic, transition metal based Heusler compounds, *Journal of Physics D: Applied Physics*, 40 (2007) 1507.
- [6] R.A. De Groot, F.M. Mueller, P.v. van Engen, K. Buschow, New class of materials: half-metallic ferromagnets, *Physical review letters*, 50 (1983) 2024.
- [7] F. Murnaghan, *Proceedings of the National Academy of Sciences of the United States of America*, 30 (1944) 244-247.
- [8] M.K. Hussain, Effects of strain on the half-metallic and elastic properties of FeCrTe and CoCrSi with Clb structure, in: *Spin*, World Scientific, 2019, pp. 1950018.
- [9] L. Feng, E. Liu, W. Zhang, W. Wang, G. Wu, First-principles investigation of half-metallic ferromagnetism of half-Heusler compounds XYZ, *Journal of magnetism and magnetic materials*, 351 (2014) 92-97.
- [10] E.N. Koukaras, G. Kalosakas, C. Galiotis, K. Papagelis, Phonon properties of graphene derived from molecular dynamics simulations, *Scientific reports*, 5 (2015) 12923.
- [11] Y. Yun, D. Legut, P.M. Oppeneer, Phonon spectrum, thermal expansion and heat capacity of UO₂ from first-principles, *Journal of nuclear materials*, 426 (2012) 109-114.
- [12] S.J. Clark, M.D. Segall, C.J. Pickard, P.J. Hasnip, M.I. Probert, K. Refson, M.C. Payne, First principles methods using CASTEP, *Zeitschrift für kristallographie-crystalline materials*, 220 (2005) 567-570.
- [13] A. Gherriche, A. Bouhemadou, Y. Al-Douri, S. Bin-Omran, R. Khenata, M. Hadi, Ab initio exploration of the structural, elastic, electronic and optical properties of a new layered perovskite-type oxyfluoride: CsSrNb₂O₆F, *Materials Science in Semiconductor Processing*, 131 (2021) 105890.

- [14] R. Fürth, On the stability of crystal lattices: VI. The properties of matter under high pressure and the lattice theory of crystals, in: *Mathematical Proceedings of the Cambridge Philosophical Society*, Cambridge University Press, 1941, pp. 177-185.
- [15] S. Pugh, XCII. Relations between the elastic moduli and the plastic properties of polycrystalline pure metals, *The London, Edinburgh, and Dublin Philosophical Magazine and Journal of Science*, 45 (1954) 823-843.
- [16] P. Ravindran, L. Fast, P.A. Korzhavyi, B. Johansson, J. Wills, O. Eriksson, Density functional theory for calculation of elastic properties of orthorhombic crystals: Application to TiSi₂, *Journal of Applied Physics*, 84 (1998) 4891-4904.
- [17] Y. Cao, J. Zhu, Y. Liu, Z. Nong, Z. Lai, First-principles studies of the structural, elastic, electronic and thermal properties of Ni₃Si, *Computational materials science*, 69 (2013) 40-45.
- [18] J. Fais, *Introduction à la physique des semi-conducteurs*, University de neuchatel, (2001).
- [19] D. Vanderbilt, Soft self-consistent pseudopotentials in a generalized eigenvalue formalism, *Physical review B*, 41 (1990) 7892.
- [20] G. Kresse, J. Hafner, Ab initio molecular-dynamics simulation of the liquid-metal–amorphous-semiconductor transition in germanium, *Physical Review B*, 49 (1994) 14251.
- [21] T. OUAHRANI, CALCUL DES PROPRIÉTÉS STRUCTURALES, THERMIQUES ET OPTIQUES DES COMPOSÉS CHALCOPYRITES PAR LA MÉTHODE FP-(L) APW, in, Université de Tlemcen-Abou Bekr Belkaid, 2011.
- [22] I. Galanakis, P. Dederichs, N. Papanikolaou, Slater-Pauling behavior and origin of the half-metallicity of the full-Heusler alloys, *Physical Review B*, 66 (2002) 174429.

General Conclusion

General conclusion

This study aims to identify new physical properties that combine ferromagnetic and half-metallic characteristics, which are promising for spintronic technology. Our research contributes to the theoretical understanding of the structural, electronic, magnetic, and elastic properties of half-metals and double half-Heusler alloys, using first-principles calculations. The FP-LAPW method, based on density functional theory (DFT), was employed and implemented using the WIEN2k code. The exchange-correlation functional was treated with the generalized gradient approximation (GGA-PBE96).

We focused on the study of half-Heusler and double half-Heusler compounds, specifically CrCoSi, MnCoSi, and CrMnCo₂Si₂, in the C1b structure with three possible atomic arrangements: type I, type II, and type III. Structural properties were investigated across different magnetic configurations, including non-magnetic (NM), ferromagnetic (FM), and antiferromagnetic (AFM) phases. Our results show that all the materials studied are stable in the ferromagnetic phase. A systematic calculation was performed to determine the lattice parameters, bulk modulus (B), and its derivative (B').

The main findings of this study are summarized as follows:

Structural properties:

We first calculated the energy versus volume curves for CrCoSi and MnCoSi compounds in their ferromagnetic (FM), non-magnetic (NM), and antiferromagnetic (AFM) phases. Our results show that the half-Heusler (HH) compounds are most stable in the FM phase within the Type I structure, as this phase has the lowest energy. For the double half-Heusler (DHH) CrMnCo₂Si₂, optimization across FM, NM, and AFM phases revealed the FM phase as the most stable.

Mechanical properties:

We investigated the elastic properties of each compound by calculating the elastic constants C_{ij} (C_{11} , C_{12} , and C_{44}) for the most stable phase. Using these constants, we derived additional mechanical parameters such as the shear modulus GGG, Young's modulus E , Poisson's ratio ν , and the anisotropy factor A . The bulk modulus values calculated from the elastic constants closely match those obtained from total energy optimization. Among the compounds, CrCoSi exhibits the highest resistance to deformation. In the CrMnCo₂Si₂ DHH

alloy, the shear modulus indicates strong resistance to reversible deformation caused by shear strain, and its Young's modulus suggests it has greater hardness than its parent compounds, CrCoSi and MnCoSi.

Dynamical stability:

The dynamical stability of CrMnCo₂Si₂ was confirmed by calculating its phonon dispersion diagram using density functional perturbation theory (DFPT). The phonon dispersion, plotted along high-symmetry lines in the Brillouin zone, shows no soft modes (negative frequencies), confirming the compound's dynamical stability.

Electronic and magnetic properties:

The band structures of the studied HH compounds are similar, with minor differences. In the majority-spin channel, the bands cross the Fermi level, while in the minority-spin channel, the Fermi level is located within a band gap. This behavior classifies the HH compounds as half-metals. The half-metallic gaps are approximately 0.85 eV for CrCoSi and 0.02 eV for MnCoSi. In contrast, the DHH compound CrMnCo₂Si₂ has reduced half-metallic gaps of 0.53 eV and 0.002 eV. The magnetic moments in CrCoSi and MnCoSi originate primarily from the Cr and Mn atoms. The large exchange splitting between the spin-up and spin-down states around the Fermi level in the d-orbitals of Cr and Mn results in 100% spin polarization.

This study opens new avenues in materials science, highlighting double half-Heusler compounds as a promising class of materials with exceptional properties such as phase transitions, magnetoresistance, half-metallicity, spintronic applications, and shape memory effects.

Half-metallicity from CrCoSi and MnCoSi half-Heusler alloys to their derivative double half-Heusler CrMnCo₂Si₂

Hiba Elarabi^a, Friha Khelifaoui^a, Keltouma Boudia^b, Fatima Labani^a, Mama Hamlat^a, Ouafaa Sadouki^b, Fadila Belkharroubi^c, Fares Faïd^d, Abdelmadjid Bouhemadou^e, and Bahri Deghfel^f

^aLaboratory of Physicochemical Studies, University of Saida-Dr. Moulay Tahar, Saida 20000, Algeria; ^bUniversity of Tissemsilt, Ahmed Ben Yahia El-Wanchrissi, Algeria; ^cLaboratory of Physical Chemistry of Advanced Materials (LPCMA), University of Djillali Liabes, BP 89, 22000, Sidi-Bel-Abbes, Algeria; ^dCommon Trunk Sciences and Technology Department, Faculty of Technology, University of Laghouat, Algeria; ^eLaboratory for Developing New Materials and their Characterizations, University of Ferhat Abbas Setif 1, Faculty of Sciences, Department of Physics, Setif 19000, Algeria; ^fDepartment of Physics, Faculty of Sciences, University of M'sila, Algeria

Corresponding author: **Friha Khelifaoui** (email: friha.khelifaoui@univ-saida.dz)

Abstract

The structural, elastic, electronic, and magnetic properties of the CrCoSi, MnCoSi parent half-Heusler (HH) alloys, and their CrMnCo₂Si₂ derivative double half-Heusler (DHH) compound are studied, utilizing the augmented plane wave method, which is based on density functional theory and implemented in the WIEN2k code. The stability of HH structure of the CrCoSi and MnCoSi alloys has been checked for their non-magnetic and ferromagnetic phases, leading to that the latter phase of the type I arrangement is the most stable. The CrMnCo₂Si₂ DHH alloy, derivative from the found structural and magnetic ground states of CrCoSi and MnCoSi HH alloys, is constructed and investigated. This DDH as well as its CrCoSi parent HH are found to be resistant to deformation and can be classified as ductile materials, whereas the MnCoSi compound is brittle. By the gradient generalized approximation (GGA), the electronic structures of CrCoSi, MnCoSi, and CrMnCo₂Si₂ compounds exhibit a metallic behavior in the spin-up channel and a semiconducting behavior in the spin-down channel, with band gaps (half-metallic gaps) of 0.851(0.020), 0.852(0.021), and 0.531(0.002) eV, respectively. The half-metallicity of CrMnCo₂Si₂ DHH is retained with smaller (larger) band gap (half-metallic gap) of 0.38(0.106) eV than that of GGA, using GGA + U approximation. In addition, the total magnetic moments are found to be 1, 2, and 3 μ_B for CrCoSi, MnCoSi, and CrMnCo₂Si₂, respectively. Therefore, these alloys can be good candidates for spintronic applications due to their half-metallicity.

Key words: half-metal, heusler alloys, spin polarization, mechanical stability, FP-LAPW

1. Introduction

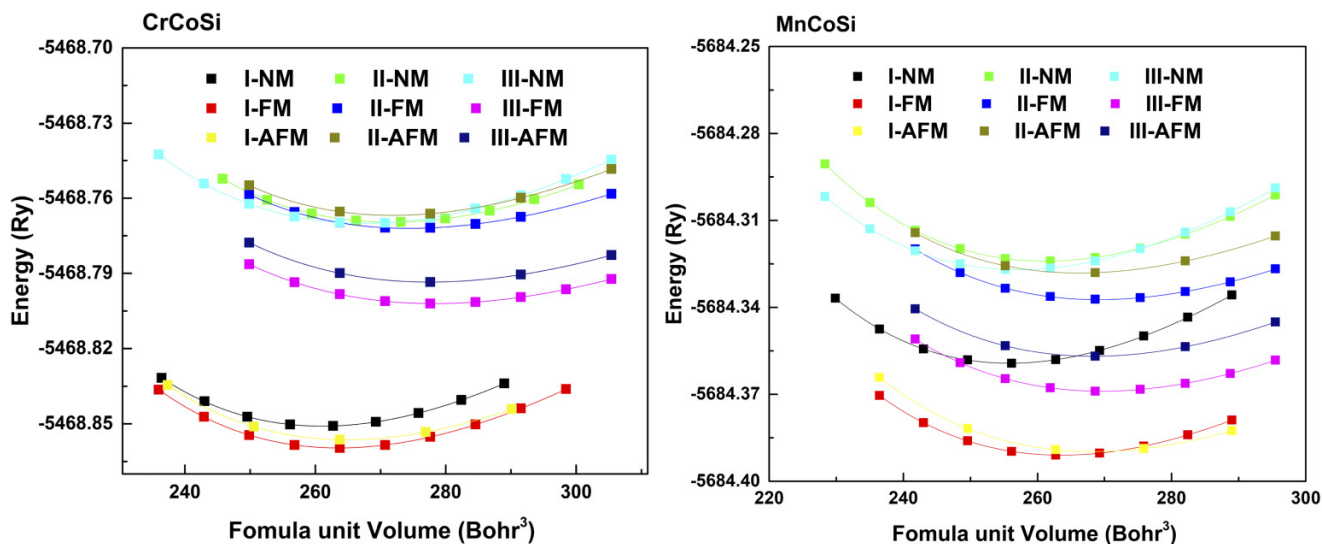
Spin-based electronics has grown into a significant field of study that spans a wide range of high spin-polarized materials, used in spintronic devices. It overcomes the limitations of electronics by using the spin-to-store information instead of charge of electrons. The half-metallic ferromagnets (HMFs) are an important class of spintronic materials with a very unique electronic structure. In these materials, electrons with one spin orientation pass through the Fermi surface to participate in conduction, showing a metallic character; while the electrons with the other spin orientation exhibit insulator or semiconductor characteristics [1, 2].

Therefore, the half-metals have theoretically a spin polarization of 100% and can provide fully spin-polarized carriers. They are regarded as ideal materials for the construction of spintronic devices and have attracted much attention. Heusler alloys [3] are one of the most motivating category of materials with half-metallic behavior, which structurally have many possible types: full-Heusler alloys with general formula X₂YZ, half-Heusler (HH) with formula XYZ, and quater-

nary compound with the composition XX'YZ. Several Heusler alloys have been investigated and found to be HMFs, such as that of de Groot et al. 1983 [4], where they have shown that the most famous HH, NiMnSb compound, is a half-metallic ferromagnetic (FM) material, using the magnetic measurements [5]. The first prediction of this phenomenon, in the case of quaternary and full Heusler compounds, has been found by the Japanese research groups; Ishida et al. studied the Co₂MnZ compounds, where Z matches to Si and Ge [6] and Alijani et al. have demonstrated that the quaternary intermetallic Heusler compounds CoFeMnZ (Z = Al, Ga, Si, or Ge) are potential HMFs with high Curie temperatures, using ab initio electronic structure calculations [7]. Another renowned class of HMFs is found in the rutile structure like the magnetic oxide Fe₃O₄ [8] and CrO₂ [9]. Galanakis et al. showed that zinc-blende compounds have a FM half-metallic behavior for a wide range of lattice constants [10]. The same behavior appears in double perovskite Sr₂CrReO₆ [11].

One of the Heusler family's well-known HMFs or near-HMFs is the HH alloys. Recently, the investigation of Uto et al. [12],

Fig. 1. Total energy per formula unit of ferromagnetic (FM), non-magnetic (NM), and antiferromagnetic (AFM) phases as functions of the volume for CrCoSi and MnCoSi HH alloys.



using density functional theory (DFT) calculations, indicate that CoCrSb is mechanically stable and has a half-metallic behavior, with a minority-spin band gap of 0.81 eV. Furthermore, Javed et al. [13] have calculated the spin-polarized band structures, cohesive formation energy, elastic constants, and have also analyzed the phonon dispersion curve of CrMnS HH to prove its half-metallic FM behavior, thermodynamically, mechanically, and dynamical stabilities. Latest DFT simulations by Ozdemir et al. [14] indicated a half-metallic behavior in MnZrX HH compounds ($X = \text{In, Tl, C, Si, Ge, Sn, Pb, N, P, As, Sb, O, S, Se, Te}$) [21].

In all above mentioned materials, the half-metallic character is caused by the d-spin polarization of the transition elements. Inspired by HH alloys, particularly those based on transition metals, and with the aim of enhancing literature with novel (HMFs) materials that have high spin polarization, we have studied novel double half-Heusler (DHH) CrMnCo₂Si₂, derivative from the HH alloys CrCoSi and MnCoSi, which have also been examined and compared with the results of Hussain [15], and Feng et al. [16]. In this paper, the outcomes of these latter are also compared with those of the considered novel DHH compound CrMnCo₂Si₂.

2. Computational method

In this paper, the full potential linearized augmented plane wave (FP-LAPW) method [17], within the framework of the DFT, as implemented in WIEN2k code [18], was used to examine the structural, mechanical, and magneto-electronic properties of CrCoSi, MnCoSi, and CrMnCo₂Si₂ Heusler alloys. The generalized gradient approximation (GGA) of Perdew–Burke–Ernzerhof [19, 20] was used to evaluate the exchange–correlation energy functional, for all considered materials, but for only CrMnCo₂Si₂ DHH compound, the Hubbard correction is added to the GGA (i.e., GGA + U), with the effec-

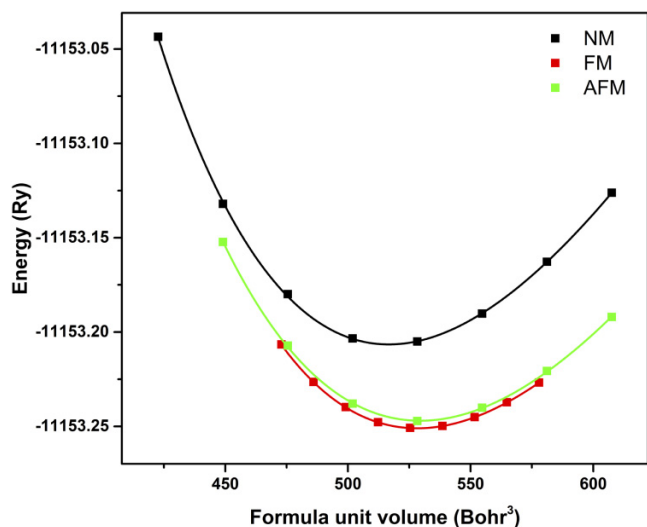
tive values (U_{eff}) of 1.59, 1.92, and 1.69 eV for Cr, Co, and Mn atoms, respectively. It has been demonstrated that these U_{eff} values are accurate for describing the magnetic moment and electronic structure in the Heusler alloys [21]. In this method, the space is divided into non-overlapping muffin-tin (MT) spheres separated by an interstitial region, and the used MT radii for Cr, Mn, Co, and Si atoms are 1.46, 1.71, 1.83, 1.5, and 1.71 (Bohr), respectively. In addition, the set cut-off parameters $R_{\text{MT}} \cdot K_{\text{max}}$, l_{max} , G_{max} , and $N_{\text{k-points}}$ are 8.0, 10, 12, and 3000, respectively, where R_{MT} represent the smallest MT sphere radius, K_{max} is the maximum modulus for the reciprocal vectors, l_{max} is the maximum angular quantum number for the expansion of wave functions inside the spheres, G_{max} is the plane-wave cutoff (magnitude of largest vector in charge density Fourier expansion), and $N_{\text{k-points}}$ is the number of k-points in the whole Brillouin zone. The convergence criterion of 10^{-6} Ry and 10^{-5} e for the energy and charge, respectively, is used.

3. Results and discussion

3.1. Structural properties

The most important step in ab initio calculations is the determining of the structural properties for a given system on its ground state, which will enable us to understand other important physical properties. CrMnCo₂Si₂ crystallizes in a tetragonal structure with a space group $N^{\circ}115$, generated from the two HH compounds CrCoSi and MnCoSi. The energy versus volume, for latter compounds (i.e., HH) in their FM, non-magnetic (NM), and antiferromagnetic (AFM) phases, is calculated in the first step and shown in Fig. 1. These graphs show that our HH compounds are more stable in FM phase of type I (i.e., specified atomic arrangement: Cr/Mn(0,0,0), Co(1/4,1/4,1/4), Si(1/2, 1/2,1/2)) structure than the other phases because the corresponding energy is the

Fig. 2. Total energy per formula unit as functions of the volume for the ferromagnetic (FM), non-magnetic (NM), and antiferromagnetic (AFM) phases of CrMnCo₂Si₂ DHH alloy.



lowest. From this type structure, the DHH structure is obtained by substitution of two Cr atoms, in the cubic conventional cell of CrCoSi HH (lattice parameter a_{HH}), with Mn atoms. Therefore, the obtained structure has a tetragonal structure ($a_{DHH} = \frac{a_{HH}}{\sqrt{2}}$, $c_{DHH} = a_{HH}$). The optimization of this obtained DHH structure is performed for its FM, NM, and AFM phases, as shown in Fig. 2. As can be seen from this figure, the FM phase is the most stable magnetic phase. In addition, to obtain the ground state properties, the calculated total energies as functions of volume are fitted with the Birch-Murnaghan equation [22], as follows:

$$E(V) = E_0 + \frac{9V_0B_0}{16} \left\{ \left[\left(\frac{V_0}{V} \right)^{2/3} - 1 \right]^3 \hat{B}_0 + \left[\left(\frac{V_0}{V} \right)^{2/3} - 1 \right]^2 \left[6 - 4 \left(\frac{V_0}{V} \right)^{2/3} \right] \right\} \quad (1)$$

Our calculated equilibrium lattice constants, bulk moduli B , pressure derivatives B' , and formation energies E_{form} are presented in Table 1. The bulk modulus is a measure of how resistant these compounds are to compression and is determined by the equation, $B = V \frac{\partial^2 E}{\partial V^2}$. The obtained results, as can be seen in Table 1, show that the resistance to compression (Bulk modulus) decreases with the increase of X atomic number ($B(\text{CrCoSi}) > B(\text{CrMnCo}_2\text{Si}_2) > B(\text{MnCoSi})$).

To verify the validity of synthesizing these alloys, we calculated the energy of formation using the following expressions:

$$E_{form}(\text{XCoSi}) = E_{\text{XCoSi}}^{\text{tot}} - (E_{\text{X}}^{\text{bulk}} - E_{\text{Ca}}^{\text{bulk}} - E_{\text{Si}}) \quad (2)$$

$$E_{form}(\text{CrMnCo}_2\text{Si}_2) = E_{\text{CrMnCo}_2\text{Si}_2}^{\text{tot}} - (E_{\text{Cr}}^{\text{bulk}} + E_{\text{Mn}}^{\text{bulk}} + 2E_{\text{Ca}}^{\text{bulk}} + 2E_{\text{Si}}) \quad (3)$$

where $E_{\text{XCoSi}}^{\text{tot}}$ and $E_{\text{CrMnCo}_2\text{Si}_2}^{\text{tot}}$ are the total energies per unit cell for XCoSi ($X = \text{Cr}$ and Mn) and CrMnCo₂Si₂, respectively, at the equilibrium state and $E_{\text{Cr}}^{\text{bulk}}$, $E_{\text{Mn}}^{\text{bulk}}$, $E_{\text{Co}}^{\text{bulk}}$, and $E_{\text{Si}}^{\text{bulk}}$ match to the total energy for Cr, Mn, Co, and Si per atom, respectively, at ground state. The resulted negative values of the formation energy point out that our studied compounds are thermodynamically stable and it is possible to synthesize them experimentally.

To check the dynamical stability of the CrMnCo₂Si₂ compound, we calculated its phonon dispersion diagram using the linear response method within the density functional perturbation theory, as implemented in the CASTEP code [23]. The calculated phonon dispersion along lines of high symmetry in the Brillouin zone, for CrMnCo₂Si₂, is presented in Fig. 3. It is known that the absence of soft modes (imaginary modes, negative frequencies) in the phonon dispersion curve of a material implies its dynamical stability [24]. There are no negative frequencies in the phonon dispersion diagram, shown in Fig. 3, which highlights the dynamical stability of the CrMnCo₂Si₂ compound.

3.2. Mechanical properties

With a view to affirm the stabilization of our studied compounds, the elastic properties are performed using IRelast package, incorporated in WIEN2k code. The gained results reported in Table 2 are positive and obey Born's stability criteria for cubic structures [25]: $C_{11} > 0$, $C_{11} - C_{12} > 0$, $C_{11} + 2C_{12} > 0$, and $C_{44} > 0$, and for tetragonal (I) structures [26]: $C_{11} > 0$, $C_{33} > 0$, $C_{44} > 0$, $C_{66} > 0$, $C_{11} - C_{12} > 0$, $C_{11} + C_{33} - 2C_{13} > 0$, $2C_{11} + C_{33} + 2C_{12} + 4C_{13} > 0$, subsequently, CrCoSi, MnCoSi, and CrMnCo₂Si₂ are mechanically stable.

Other mechanical quantities, such as bulk $B_{C/T}$ (C for cubic structure and T for tetragonal structure), shear G, Young's moduli E , anisotropic factor, as well as Poisson's ratio, can be obtained from the evaluated elastic constants by using the following formula:

$$B_C = \frac{C_{11} + 2C_{12}}{3}, \quad B_T = \frac{1}{9}(2C_{11} + 2C_{12} + 4C_{13} + C_{33}) \quad (4)$$

$$G_C = \frac{1}{5}(3C_{44} + C_{11} - C_{12}) \quad (5)$$

$$G_T = \frac{1}{2} \left[\frac{2C_{11} + C_{33} - C_{12} - 2C_{13}}{15 + (2C_{44} + C_{66})/5} + \frac{4(S_{11} + S_{22} + S_{33}) + 3(S_{44} + S_{55} + S_{66}) - 4(S_{12} + S_{13} + S_{23})}{15} \right] \quad (6)$$

$$E_{C/T} = \frac{9BG}{3B + G} \quad (7)$$

$$\nu_{C/T} = \frac{1}{2} \left(1 - \frac{E}{3B} \right) \quad (8)$$

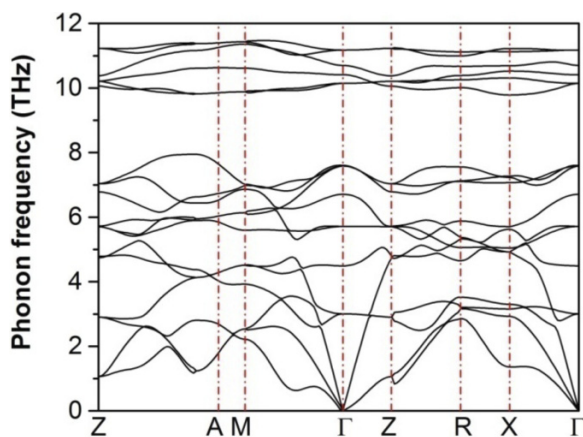
$$A_C = \frac{2C_{44}}{C_{11} - C_{12}} A_{C/T} = 5 \frac{G_V}{G_R} + \frac{B_V}{B_R} - 6 \quad (9)$$

where B_V , G_V , B_R , and G_R are the estimated bulk and shear moduli by Voigt and Reuss methods, respectively. The calculated elastic constants as well as mechanical parameters, for all considered materials, are illustrated in Table 2. It can be seen that the bulk modulus values resulting through the elastic constants for the three compounds accord well with that gained from the total energy optimization. According

Table 1. Calculated lattice parameters (in Å) for the structural ground state of the CrCoSi, MnCoSi HH alloys and parent structure of CrMnCo₂Si₂ DHH, bulk moduli (in GPa), their derivative pressures, and formation (E_{form}) energies (in eV/atom) of the structural and magnetic ground phase (FM) for CrCoSi, MnCoSi, and CrMnCo₂Si₂ compounds.

X		a_{HH}	B	B'	E_{tot}	E_{form}
CrCoSi	GGA	5.3864	190.87	4.86	−5468.85962	−0.45
		5.4100 [15]				
		5.3900 [16]				
MnCoSi	GGA	5.3857	174.72	5.02	−5684.39097	−0.44
		5.4100 [16]				
CrMnCo ₂ Si ₂	GGA	5.3899	181.00	4.72	−11153.250925	−0.45

Fig. 3. Phonon dispersion diagram along lines of high symmetry in the Brillouin zone for the CrMnCo₂Si₂ compound.



to the calculated datum, CrCoSi has a stronger capability to resist deformation compared with other compounds. Otherwise, the shear modulus presents a strong ability to defend versus reversible deformation by shear strain for CrMnCo₂Si₂ DHH alloy, while its young modulus value shows a greater hardness than their parent HH CrCoSi and MnCoSi.

To categorize ductility and brittleness of our studied compound, the B/G ratio, called Pugh's ratio, too is usually used. Depending on Pugh's [27] index, if $B/G < 1.75$ ($B/G > 1.75$), the material is characterized by brittle nature, otherwise, the ductile nature is expected. The calculated value of B/G was found to be 1.9, 1.7, and 1.9 for CrCoSi, MnCoSi, and CrMnCo₂Si₂, respectively. One can look out that MnCoSi is categorized as brittle, while CrCoSi and CrMnCo₂Si₂ compounds are showing their ductility.

The analysis of the degree of anisotropy requires the use of anisotropic parameter A . For isotropic materials $A = 1$; however for anisotropic materials $A \neq 1$ [28]. With regard to compounds CrCoSi, MnCoSi, and CrMnCo₂Si₂, it is found to be different to unity, so, these Heusler alloys have an anisotropic behavior. Poisson's ratio ν is ordinarily utilized to comprehend the kind of the bonding force in a compound [29]. The value of Poisson's ratio was evaluated to be 0.28, 0.26, and 0.27 for CrCoSi, MnCoSi, and CrMnCo₂Si₂, respectively, is around 0.25, indicating a higher ionic behavior as interatomic bonding. The resulted computed elastic parameters

are, as shown in Table 2, in good agreement with those of Feng et al. [16] and Hussain et al. [15], for both investigated HH alloys.

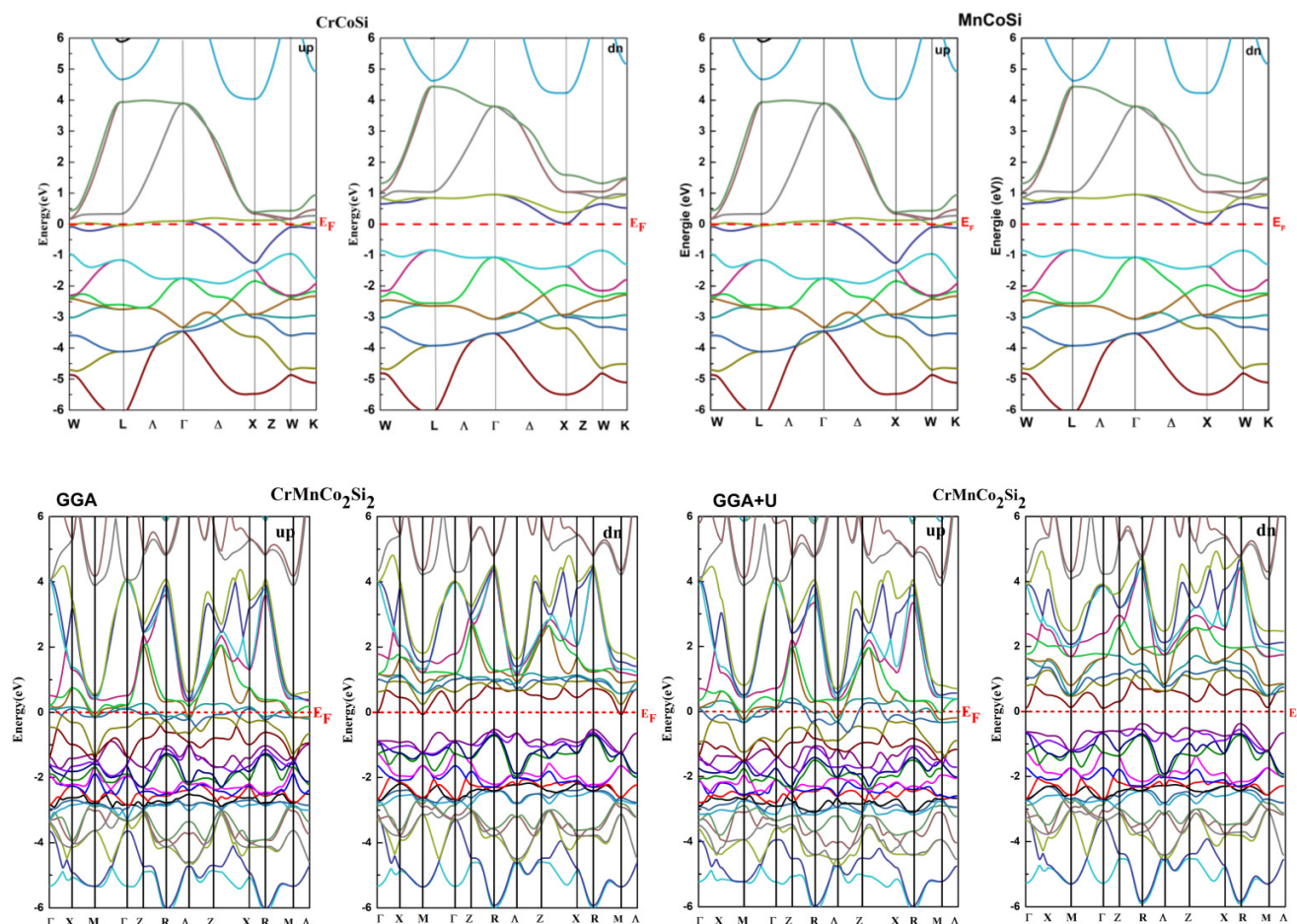
3.3. Electronic and magnetic properties:

This section was used to comprehend the behavior of the electronic states of the CrCoSi and MnCoSi HH alloys and their derivative DHH CrMnCo₂Si₂ from their calculated band structures and density of state (DOS) maps, using GGA approximation, which are plotted for both spin channels. As shown in Fig. 4, it is clear that the general band profiles are almost analogous for both studied HH with a little diversity in the details. It can be seen band crossings with the Fermi level in the majority-spin channel, whereas in the minority-spin bands, the Fermi level just situated in the energy band gap, describing the considered HHs as half-metals with energy gaps (half-metallic gaps) of about 0.85(0.02) eV for both of them. This similarity is due to their very close atomic numbers of Cr ($Z = 24$) and Mn ($Z = 25$) atoms. In addition, as can be seen from Table 3, these findings are smaller than those of Feng et al. [16] and Hussain et al. [15] due to different used methods, based on the description of the interaction between ions and electrons by ultrasoft pseudo potentials [30, 31]. Furthermore, our investigated derivative DHH CrMnCo₂Si₂ has much smaller gaps (HM gap) of 0.53(0.002) and 0.382(0.106) eV, obtained by GGA and GGA + U approximations, respectively. Thus, the obtained data demonstrate the half-metallic character of CrCoSi, MnCoSi, and CrMnCo₂Si₂ Heusler alloys, as indicated in Table 3.

To comprehend the electronic properties, total (TDOS) and partial (PDOS) densities of states have been plotted and given in Fig. 5. The magnetic moment is essentially originated from Cr and Mn atoms in which the Cr-d and Mn-d states have large exchange divisions between the states of the spin-up and -down channels around the Fermi level for CrCoSi and MnCoSi, respectively, as shown in Table 4. In addition, Co atom has a negative magnetic moment for both HH alloys, demonstrating an antiferromagnetic interaction between Co and Cr/Mn atoms. There is no contribution of Si atom for all studied Heusler compounds. The total magnetic moments are found to be 1 and 2 μ_B for CrCoSi and MnCoSi, respectively, but, for their derivative CrMnCo₂Si₂ DHH alloy, the results of both approximations (i.e., GGA and GGA + U) show that the main contribution to its total magnetic moment is from

Table 2. Elastic constants C_{11} , C_{12} , C_{13} , C_{33} , C_{44} , C_{66} (in GPa), bulk B , Young E (GPa), shear G moduli (in GPa), B/G , anisotropic parameter A , and Poisson's coefficients ν of CrCoSi, MnCoSi, and CrMnCo₂Si₂ Heusler alloys.

X	C_{11}	C_{12}	C_{13}	C_{33}	C_{44}	C_{66}	B	E	G	B/G	A	ν
CrCoSi	285.5	145.8	–	–	132.3	–	192.4	125.8	49.3	1.9	0.62	0.28
	274.6 [15]	115.2 [15]			94.9 [15]							
MnCoSi	253.60	137.97	–	–	127.5	–	176.5	131.9	52.1	1.7	0.75	0.26
CrMnCo ₂ Si ₂	330.96	74.15	137.7	268.2	127.5	65.2	181.0	248.0	97.5	1.9	0.57	0.27

Fig. 4. Spin-polarized band structures for CrCoSi, MnCoSi, and CrMnCo₂Si₂ Heusler alloys.**Table 3.** Gap and half-metallic gap (in eV) of CrCoSi, MnCoSi, and CrMnCo₂Si₂ Heusler alloys.

X		Gap	HM gap
CrCoSi	GGA	0.851	0.020
		1.160 [15]	0.650 [15]
		0.670 [16]	0.660 [16]
MnCoSi	GGA	0.852	0.021
		0.640 [16]	0.190 [16]
CrMnCo ₂ Si ₂	GGA	0.53	0.002
	GGA + U	0.382	0.106

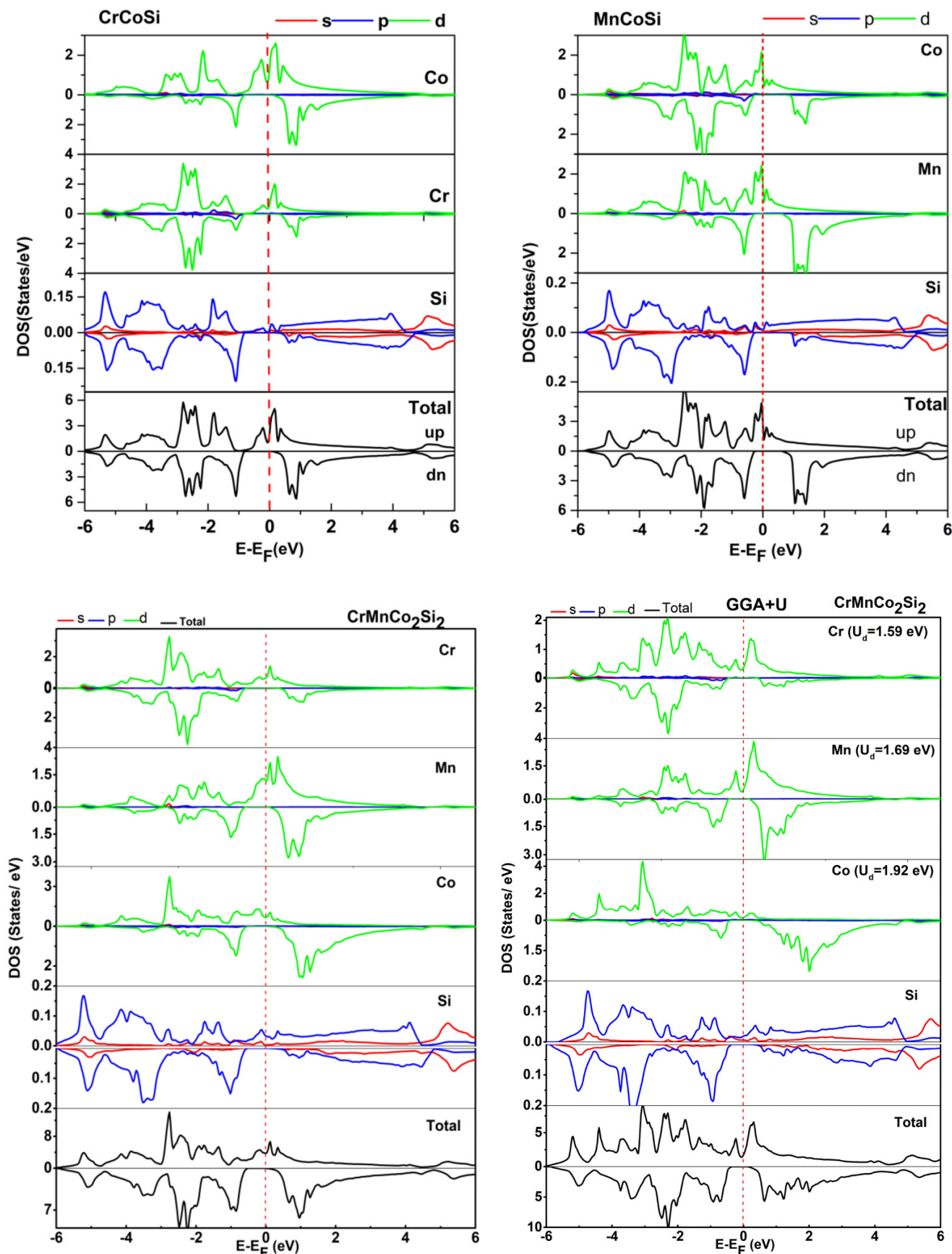
Cr and Mn atoms, as demonstrated by large splitting of their d-orbitals around Fermi level, leading to 100% spin polarization. Furthermore, little contributions to the total magnetic moment are from Co and Si atoms. The spin magnetization

has an integer of $3 \mu_B$ for CrMnCo₂Si₂, confirming its classification as half-metallic material.

4. Conclusion

Using FP-LAPW method, the structural, elastic, electronic, and magnetic properties of CrCoSi, MnCoSi, and CrMnCo₂Si₂ have been investigated. According to our calculations, they are stable in their FM phase. When compared with other compounds, CrCoSi's bulk modulus shows a higher resistance to the deformation. Otherwise, a large shear modulus value indicates a strong ability to defend against reversible deformation by shear strain for The DHH CrMnCo₂Si₂. The B/G values indicate the brittleness of MnCoSi, whereas CrCoSi, and CrMnCo₂Si₂ compounds are showing their ductility. The anisotropic coefficient A is different from the

Fig. 5. Spin-polarized density of states (DOS) for CrCoSi, MnCoSi, and CrMnCo₂Si₂ Heusler alloys.



Can. J. Phys. Downloaded from cdservicepub.com by F. Khelifaoui on 11/17/23
For personal use only.

Table 4. Atomic (M_{Cr} , M_{Co} , M_{Mn} , M_{Si}), interstitial ($M_{Intersti}$), and total magnetic (M_{Tot}) moments (in μ_B) for CrCoSi, MnCoSi, and CrMnCo₂Si₂ Heusler alloys.

X	Method	M_{Cr}	M_{Mn}	M_{Co}	M_{Si}	$M_{Intersti}$	M_{Tot}
CrCoSi	GGA	1.166	–	–0.178	–0.031	0.043	1.000
		1.550 [15]		–0.410 [15]	–0.09 [15]		1.000 [15]
		1.560 [16]		–0.42 [16]			1.000 [16]
MnCoSi	GGA	–	2.114	0.027	–0.061	0.080	1.999
			2.120 [16]	–0.040 [16]			2.000 [16]
CrMnCo ₂ Si ₂	GGA	0.612	2.560	–0.042	–0.034	–0.018	3.000
	GGA + U	0.438	3.352	–0.329	–0.058	–0.047	3.000

unit for all compounds, so, CrCoSi, MnCoSi, and CrMnCo₂Si₂ compounds have an anisotropic behavior. Poisson's ratio values of 0.28, 0.26, and 0.27 for CrCoSi, MnCoSi, and CrMnCo₂Si₂, indicate a higher ionic behavior as inter-atomic bonding. The electronic structures of CrCoSi, MnCoSi, and CrMnCo₂Si₂ exhibit a metallic behavior for the spin-up channel and a semiconducting behavior in the spin-down channel. The integer values of 1 μ_B (CrCoSi), 2 μ_B (MnCoSi), and 3 μ_B (CrMnCo₂Si₂) confirm their half-metallic nature with a major contribution of Cr and Mn atoms. The 100% spin polarization of CrCoSi, MnCoSi, and CrMnCo₂Si₂ systems make all of them good candidates for spintronic applications.

Article information

History dates

Received: 30 August 2022

Accepted: 2 January 2023

Accepted manuscript online: 18 May 2023

Version of record online: 18 May 2023

Copyright

© 2023 The Author(s). Permission for reuse (free in most cases) can be obtained from copyright.com.

Data availability

Data generated or analyzed during this study are provided in full within the published article.

Author information

Author contributions

Conceptualization: FK

Data curation: FK

Formal analysis: HE, FF, AB, BD

Investigation: HE, FB

Methodology: KB, OS

Project administration: KB, FL

Resources: KB

Software: FL

Supervision: FK, FL

Validation: OS

Visualization: HE

Writing – original draft: HE

Writing – review & editing: FK, KB, MH, FB, AB, BD

Competing interests

The authors declare there are no competing interests.

References

1. A. Aguayo and G. Murrieta. *J. Magn. Magn. Mater.* **323**, 3013 (2011). doi:[10.1016/j.jmmm.2011.06.038](https://doi.org/10.1016/j.jmmm.2011.06.038).
2. M. Katsnelson, V.Y. Irkhin, L. Chioncel, A. Lichtenstein, and R.A. de Groot. *Rev. Mod. Phys.* **80**, 315 (2008). doi:[10.1103/RevModPhys.80.315](https://doi.org/10.1103/RevModPhys.80.315).
3. A. Birsan and V. Kuncser. *J. Magn. Magn. Mater.* **388**, 1 (2015). doi:[10.1016/j.jmmm.2015.04.007](https://doi.org/10.1016/j.jmmm.2015.04.007).
4. R. de Groot, F. Mueller, P. van Engen, and K. Buschow. *Phys. Rev. Lett.* **50**, 2024 (1983). doi:[10.1103/PhysRevLett.50.2024](https://doi.org/10.1103/PhysRevLett.50.2024).
5. R. Helmholdt, R. de Groot, F. Mueller, P. van Engen, and K. Buschow. *J. Magn. Magn. Mater.* **43**, 249 (1984). doi:[10.1016/0304-8853\(84\)90075-1](https://doi.org/10.1016/0304-8853(84)90075-1).
6. S. Ishida, S. Fujii, S. Kashiwagi, and S. Asano. *J. Phys. Soc. Jpn.* **64**, 2152 (1995). doi:[10.1143/JPSJ.64.2152](https://doi.org/10.1143/JPSJ.64.2152).
7. V. Alijani, S. Ouardi, G.H. Fecher, et al. *Phys. Rev. B*, **84**, 224416 (2011). doi:[10.1103/PhysRevB.84.224416](https://doi.org/10.1103/PhysRevB.84.224416).
8. I. Galanakis and P. Mavropoulos. *Phys. Rev. B*, **67**, 104417 (2003). doi:[10.1103/PhysRevB.67.104417](https://doi.org/10.1103/PhysRevB.67.104417).
9. K. Yao, G. Gao, Z. Liu, and L. Zhu. *Solid State Commun.* **133**, 301 (2005). doi:[10.1016/j.ssc.2004.11.016](https://doi.org/10.1016/j.ssc.2004.11.016).
10. W.-H. Xie, Y.-Q. Xu, B.-G. Liu, and D. Pettifor. *Phys. Rev. Lett.* **91**, 037204 (2003). doi:[10.1103/PhysRevLett.91.037204](https://doi.org/10.1103/PhysRevLett.91.037204).
11. R. Soulen, Jr., M.S. Osofsky, B. Nadgorny, et al. *Science*, **282**, 85 (1998). doi:[10.1126/science.282.5386.85](https://doi.org/10.1126/science.282.5386.85).
12. O.T. Uto, P.O. Adebambo, J.O. Akinlami, S. Kenmoe, and A.G. Adebayo. *Solids*, **3**, 22 (2022). doi:[10.3390/solids3010002](https://doi.org/10.3390/solids3010002).
13. M. Javed, M.A. Sattar, M. Benkraouda, and N. Amrane. *Opt. Quant. Electron.* **54**, 1 (2022). doi:[10.1007/s11082-021-03373-1](https://doi.org/10.1007/s11082-021-03373-1).
14. E. G. Özdemir and Z. Merdan. *J. Magn. Magn. Mater.* **491**, 165567 (2019). doi:[10.1016/j.jmmm.2019.165567](https://doi.org/10.1016/j.jmmm.2019.165567).
15. M. K. Hussain. *In Spin world scientific*. 2019. p. 1950018.
16. L. Feng, E. Liu, W. Zhang, W. Wang, and G. Wu. *J. Magn. Magn. Mater.* **351**, 92 (2014). doi:[10.1016/j.jmmm.2013.09.054](https://doi.org/10.1016/j.jmmm.2013.09.054).
17. P. Blaha, K. Schwarz, P. Sorantin, and S. Trickey. *Comput. Phys. Commun.* **59**, 399 (1990). doi:[10.1016/0010-4655\(90\)90187-6](https://doi.org/10.1016/0010-4655(90)90187-6).
18. P. Blaha, K. Schwarz, G. K. Madsen, D. Kvasnicka, and J. Luitz. *An augmented plane wave+ local orbitals program for calculating crystal properties*. Northwestern University, Evanston, IL. 2001. p. 60.
19. J.P. Perdew, K. Burke, and Y. Wang. *Phys. Rev. B*, **54**, 16533 (1996). doi:[10.1103/PhysRevB.54.16533](https://doi.org/10.1103/PhysRevB.54.16533).
20. J.P. Perdew, K. Burke, and M. Ernzerhof. *Phys. Rev. Lett.* **77**, 3865 (1996). doi:[10.1103/PhysRevLett.77.3865](https://doi.org/10.1103/PhysRevLett.77.3865).
21. H.C. Kandpal, G.H. Fecher, and C. Felser. *J. Phys. D Appl. Phys.* **40**, 1507 (2007). doi:[10.1088/0022-3727/40/6/S01](https://doi.org/10.1088/0022-3727/40/6/S01).
22. F. Murnaghan. *America*, **30**, 244 (1944). doi:[10.1073/pnas.30.9.244](https://doi.org/10.1073/pnas.30.9.244).
23. S.J. Clark, M.D. Segall, C.J. Pickard, P.J. Hasnip, M.I. Probert, K. Refson, and M.C. Payne. *Z. Kristallogr. Cryst. Mater.* **220**, 567 (2005). doi:[10.1524/zkri.220.5.567.65075](https://doi.org/10.1524/zkri.220.5.567.65075).

24. A. Gherriche, A. Bouhemadou, Y. Al-Douri, S. Bin-Omran, R. Khenata, and M. Hadi. *Mater. Sci. Semicond. Process.* **131**, 105890 (2021). doi:[10.1016/j.mssp.2021.105890](https://doi.org/10.1016/j.mssp.2021.105890).
25. R. Fürth. *In Mathematical Proceedings of the Cambridge Philosophical Society*. Cambridge University Press, 1941. pp. 34.
26. F. Mouhat and F.-X. Coudert. *Phys. Rev. B*, **90**, 224104 (2014). doi:[10.1103/PhysRevB.90.224104](https://doi.org/10.1103/PhysRevB.90.224104).
27. S. Pugh. *Lond. Edinb. Dublin Philos. Mag. J. Sci.* **45**, 823 (1954). doi:[10.1080/14786440808520496](https://doi.org/10.1080/14786440808520496).
28. P. Ravindran, L. Fast, P.A. Korzhavyi, B. Johansson, J. Wills, and O. Eriksson. *J. Appl. Phys.* **84**, 4891 (1998). doi:[10.1063/1.368733](https://doi.org/10.1063/1.368733).
29. Y. Cao, J. Zhu, Y. Liu, Z. Nong, and Z. Lai. *Comput. Mater. Sci.* **69**, 40 (2013). doi:[10.1016/j.commatsci.2012.11.037](https://doi.org/10.1016/j.commatsci.2012.11.037).
30. D. Vanderbilt. *Phys. Rev. B*, **41**, 7892 (1990). doi:[10.1103/PhysRevB.41.7892](https://doi.org/10.1103/PhysRevB.41.7892).
31. G. Kresse and J. Hafner. *Phys. Rev. B*, **49**, 14251 (1994). doi:[10.1103/PhysRevB.49.14251](https://doi.org/10.1103/PhysRevB.49.14251).